UNIVERSIDAD DE MÁLAGA

Tesis doctoral:

MÉTODO PARA ESTUDIAR LA VIABILIDAD DE LAS CORRIENTES MARINAS COMO FUENTE DE ENERGÍA RENOVABLE EN SISTEMAS HIDRODINÁMICOS SUSCEPTIBLES DE APROVECHAMIENTO. CASOS PARTICULARES EN EL SUR DE LA PENÍNSULA IBÉRICA.

Autora:

María Concepción Calero Quesada

Directores:

Jesús García Lafuente

Javier Delgado Cabello

Dinámica de los Flujos Biogeoquímicos y sus Aplicaciones (EDUMA)

2021

UNIVERSIDAD DE MÁLAGA

AUTOR: María Concepción Calero Quesada

https://orcid.org/0000-0002-9667-0417

EDITA: Publicaciones y Divulgación Científica. Universidad de Málaga

Grupo de Oceanografía Física de la Universidad de Málaga

TESIS DOCTORAL:

MÉTODO PARA ESTUDIAR LA VIABILIDAD DE LAS CORRIENTES MARINAS COMO FUENTE DE ENERGÍA RENOVABLE EN SISEMAS HIDRODINÁMICOS SUSCEPTIBLES DE APROVECHAMIENTO. CASOS PARTICULARES DEL SUR DE LA PENÍNSULA IBÉRICA.

María Concepción Calero Quesada

2021

DECLARACIÓN DE AUTORÍA Y ORIGINALIDAD DE LA TESIS PRESENTADA PARA OBTENER EL TÍTULO DE DOCTOR

D./Dña MARÍA CONCEPCIÓN CALERO QUESADA estudiante del programa de doctorado DINÁMICA DE LOS FLUJOS BIOGEOQUÍMICOS Y SUS APLICACIONES de la Universidad de Málaga, autor/a de la tesis, presentada para la obtención del título de doctor por la Universidad de Málaga, titulada: "MÉTODO PARA ESTUDIAR LA VIABILIDAD DE LAS CORRIENTES MARINAS COMO FUENTE DE ENERGÍA RENOVABLE EN SISTEMAS HIDRODINÁMICOS SUSCEPTIBLES DE APROVECHAMIENTO. CASOS PARTICULARES EN EL SUR DE LA PENÍSNULA IBÉRICA"

Realizada bajo la tutorización de JESÚS GARCÍA LAFUENTE y dirección de JESÚS GARCÍA LAFUENTE Y JAVIER DELGADO CABELLO

DECLARO QUE:

La tesis presentada es una obra original que no infringe los derechos de propiedad intelectual ni los derechos de propiedad industrial u otros, conforme al ordenamiento jurídico vigente (Real Decreto Legislativo 1/1996, de 12 de abril, por el que se aprueba el texto refundido de la Ley de Propiedad Intelectual, regularizando, aclarando y armonizando las disposiciones legales vigentes sobre la materia), modificado por la Ley 2/2019, de 1 de marzo.

Igualmente asumo, ante a la Universidad de Málaga y ante cualquier otra instancia, la responsabilidad que pudiera derivarse en caso de plagio de contenidos en la tesis presentada, conforme al ordenamiento jurídico vigente.

En Málaga, a 11 de MARZO de 2022

Fdo.: MARÍA CONCEPCIÓN CALERO QUESADA
Doctorando/a

Fdo.:JESÚS GARCÍA LAFUENTE
Tutor

Fdo.: JESÚS GARCÍA LAFUENTE
Director de tesis

Fdo.: JAVIER DELGADO CABELLO
Director de tesis

Edificio Pabellón de Gobierno. Campus El Ejido. 29071
Tel.: 952 13 10 28 / 952 13 14 61 / 952 13 71 10
E-mail: doctorado@uma.es

A Abraham, a mis hijos y a toda mi familia.

ÍNDICE

ÍNDICE DE FIGURAS

ÍNDICE DE TABLAS

1.- PUBLICACIONES

La presente tesis está avalada por los artículos que abajo se detallan y un tercero pendiente de ser enviado a una revista que conforman los capítulos 5, 6 y 7. Todos ellos han sido presentados en revistas científicas que pertenecen al primer cuartil dentro de la rama de ingeniería y del área de oceanografía. El primero indica las zonas más viables para extraer energía de las corrientes marinas en el Estrecho de Gibraltar y presenta un método para localizarlas. El segundo describe la hidrodinámica del Estuario del Guadiana mediante un enfoque en 2D y explora la progresión de la onda de marea bajo diferentes forzamientos de marea y descargas de río. Finalmente, el tercero de ellos estudia la viabilidad del Estuario del Guadiana para aprovechar las corrientes marinas como fuente de energía renovable siguiendo el método expuesto en el capítulo 4. En este artículo también se hace una valoración del impacto de una granja de turbinas atendiendo a la progresión de la onda de marea a lo largo del estuario. Los artículos son:

a) *María Concepción Calero Quesada*, Jesús García Lafuente, José Carlos Sánchez Garrido, Simone Sammartino, Javier Delgado, *Energy of marine currents in the Strait of Gibraltar and its potential as a renewable energy resource,* Renewable and Sustainable Energy Reviews, 2014, 34, 98-109, http://dx.doi.org/10.1016/j.rser.2014.02.038. Impact factor: 7.89. Quartile in category: Q1

b) *María Concepción Calero Quesada,* Jesús García-Lafuente, Erwan Garel, Javier Delgado, Flavio Martins, Juan Moreno-Navas, *Effects of tidal and river discharge forcings on tidal propagation along the Guadiana Estuary,* Journal of Sea Research, 2019, 146, 1-13, http://dx.doi.org/10.1016/j.seares.2019.01.006. Impact factor: 1.7. Quartile in category: Q1

c) *María Concepción Calero Quesada,* Jesús García-Lafuente, Javier Delgado Cabello, Francisco Campuzano, *Harnessing the energy of marine currents in meso-tidal estuaries. Viability in the Guadiana Estuary (SW Iberian Peninsula).*

2.- RESUMEN Y OBJETIVOS

Dada la necesidad global de reducir la dependencia de los combustibles fósiles, los organismos públicos se esfuerzan en promover otros modelos de obtención de energía a partir de fuentes de energía renovables. Las de origen marino se encuentran entre las más prometedoras para contribuir a esta transición. Las energías marinas presentan ventajas sobre otras energías renovables por ser más predecibles y pueden funcionar a cualquier hora del día.

De las distintas formas de obtención de energía a partir de los océanos, este trabajo se ha centrado en la obtenida a partir de la energía cinética de las corrientes marinas, incluidas las de marea. Dos sistemas hídricos del sur de la Península Ibérica han sido analizados para aprovechar la intensidad de las corrientes: el Estrecho de Gibraltar y el Estuario del Guadiana. Mediante un método basado en indicadores se han identificado las zonas más propicias de estos sistemas hidrodinámicos para la instalación de una granja de turbinas. Estos indicadores consideran también información sobre la rentabilidad y vida media de los dispositivos, información que queda reflejada en una función de calidad, definida *ad hoc*.

En cada caso se usó un modelo hidrodinámico que se adaptara mejor a las características de cada sistema hídrico, el Massachusetts Institute of Technology general circulation model (MITgcm), para el Estrecho de Gibraltar y el sistema basado en el MOdelo HIDrodinámico (Mohid) en el Estuario del Guadiana. Ambos modelos fueron implementados con batimetrías de alta resolución.

En el Estrecho de Gibraltar se ha encontrado que las mejores zonas para aprovechar las corrientes están en superficie sobre el umbral de Camarinal hacia el Este, a profundidades intermedias sobre el umbral de Camarinal, en ambos casos con intensidades de flujo en torno a 900 Wm^{-2} y en profundidad sobre el umbral de Camarinal y el umbral de Espartel donde la intensidad llega a 1800 Wm^{-2} (figura 2.1). En el Estuario del Guadiana la mejor área se localiza en la parte baja del Estuario con intensidades en torno a los 1200 Wm^{-2} (figura 2.2).

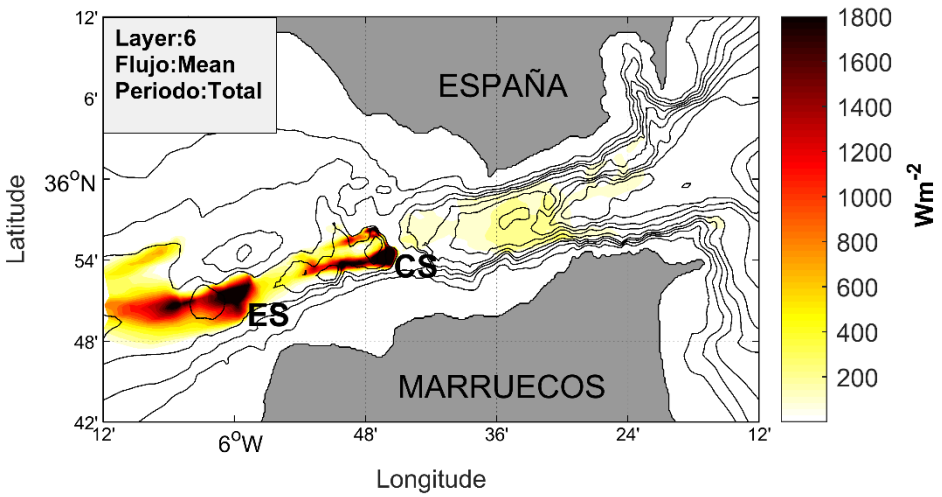

Figura 2. 1.- Flujos de energía en el Estrecho de Gibraltar. Los tonos claros en la barra de color se corresponden con valores bajos de flujo mientras que los tonos más oscuros corresponden a valores altos pero no está referenciado a los mismos valores de energía. Los topónimos señalados en la figura son ES el umbral de Espartel, CS el umbral de Camarinal (Figura tomada del capítulo 5, ver dicho capítulo para más información).

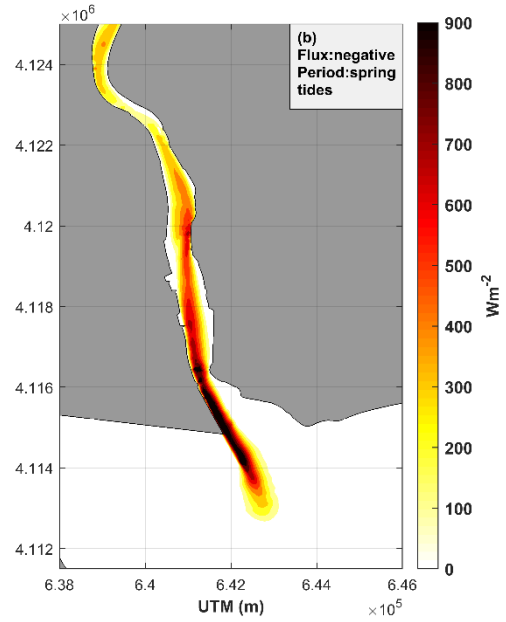

Figura 2. 2.- Flujo de energía en la parte baja del Estuario del Guadiana. La leyenda es análoga a la de la figura 1 al igual que la barra de color. Figura tomada del capítulo 7.

Se realizaron diferentes simulaciones en el Estuario del Guadiana dada la importancia de conocer la hidrodinámica del emplazamiento donde situar una granja de turbinas y detectar el impacto de la misma. Las variables tenidas en cuenta en la hidrodinámica han sido la propagación de la onda de marea, la duración de los semiciclos de marea ascendente y descendente y la diferencia de duración entre la marea llenante y vaciante.

El sistema Mohid fue implementado con un módulo que permitió simular una granja de 105 turbinas situada sobre la zona del Estuario del Guadiana más viable para la extracción de energía y se obtuvo un valor de $7.5 \cdot 10^4$ MJ por mes. Se analizó la progresión de la onda de marea en presencia y ausencia de la granja de turbinas lo que permitió evaluar el impacto de la granja de turbinas. Se concluyó que la granja no tiene un efecto significativo en la progresión de la onda de marea y los cambios observados tienen lugar tanto a continuación de la granja como aguas arriba de la granja, a gran distancia.

Estos trabajos permiten concluir que tanto el Estrecho de Gibraltar como el Estuario del Guadiana son viables para la instalación de una granja de turbinas con una evidente diferencia en cuanto a las posibles dimensiones de las mismas.

Objetivos de la tesis

Los objetivos de esta tesis consisten, en primer lugar, en el empleo de un método basado en indicadores que permite localizar las zonas más viables de un sistema hidrodinámico para la extracción de energía a partir de las corrientes marinas. En concreto se ha practicado en dos sistemas hidrodinámicos diferentes situados al sur de la Península Ibérica, que son el Estrecho de Gibraltar y el Estuario del Guadiana. De este modo, el método queda validado y puede ser generalizado a más sistemas hídrodinámicos. Se entiende una zona viable como aquella que además de presentar corrientes intensas considera otras características del flujo que pueden ser decisivas en la elección de los dispositivos y permitan una mayor vida media de los mismos. Otro de los objetivos ha sido conocer la energía que se puede obtener a partir de una granja de turbinas localizada sobre la zona más viable en el Estuario del Guadiana.

Como se ha indicado anteriormente, los estuarios son sistemas hidrodinámicos muy sensibles a cualquier tipo de cambio por lo tanto, conocer con precisión las características hidrodinámicas en un estuario bajo diferentes condiciones es esencial para una gestión sostenible (Nash et al., 2014). Por tanto, otro objetivo de la tesis ha sido el estudio de la hidrodinámica del Estuario del Guadiana. Ello va a permitir hacer una valoración del impacto ambiental que tendría la granja de turbinas situada en el estuario.

3.- INTRODUCCIÓN

3.1.- Estado del arte

La evolución tecnológica, económica y social de la humanidad durante las últimas décadas se debe principalmente al uso de combustibles fósiles. Esto provoca una fuerte dependencia a nivel mundial de esta fuente de energía limitada que sólo unos pocos países en el mundo la encuentra dentro sus fronteras. Por tanto, los países que no disponen de suficientes combustibles fósiles dependen de los países productores. Este es el caso de la Unión Europea (UE) y más concretamente de España, que importa casi en su totalidad el petróleo y el gas que consume, sus dos principales fuentes de energía. En efecto, más de la mitad (el 58.2 %) de la energía bruta disponible de la UE en 2018 corresponde a fuentes de energía importadas y desde 2013 los veintisiete Estados miembros de la UE son importadores netos de energía. En 2018, los mayores importadores netos de energía en cifras absolutas fueron Alemania, Italia, Francia y España (Eurostat, 2020).

Un aspecto negativo del uso de combustibles fósiles es el aumento de las emisiones de gases de efecto invernadero como resultado de su combustión y su contribución al aumento de temperatura global. Todo esto ha llevado a los responsables de la formulación de políticas a adoptar objetivos que limiten las emisiones de dióxido de carbono y utilizar fuentes de energía renovables, con el fin de hacer la transición a una economía sostenible (Frost et al., 2018). En diciembre de 2019, la UE se comprometió a activar un paquete de medidas para afrontar la emergencia climática a través de su "Nuevo Pacto Verde" para la consecución de la neutralidad climática en 2050, esto es, que sólo se pueda emitir lo que la Tierra es capaz de absorber. A su vez, también apuesta por extraer cualquier tipo de energía renovable local que permita el abastecimiento de las zonas circundantes.

Actualmente, las energías renovables representan el 7% de la demanda eléctrica mundial (Resch et al., 2008). La energía oceánica es abundante, geográficamente diversa y renovable. Por ejemplo, el Instituto de Investigación de Energía Eléctrica de EE. UU. (EPRI) y el Laboratorio Nacional de Energía Renovable (NREL) estiman que el potencial total de todas las energías renovables oceánicas combinadas en los Estados Unidos supera actualmente las necesidades nacionales de energía eléctrica. En Europa se calcula que podría satisfacer el 10% de la demanda de energía de la UE para 2050, lo que podría evitar el equivalente a 276 millones de toneladas de emisiones de CO2 al año (Ocean

Energy Forum, 2016). De entre ellas, la energía de las corrientes de marea representa el 0.75% de la demanda global, el resto del porcentaje proviene de la eólica marina y las olas generadas por el viento (Woolf et al., 2014).

La energía del océano puede ser captada de diferentes maneras: a través de la energía de las olas, de la energía de la corriente de las mareas (generada a partir del flujo de agua en canales estrechos) y mediante barreras de marea, que explotan la diferencia en altura a ambos lados de una presa de un estuario o una bahía (UE, 2014). Los intentos más recientes para obtener la energía procedente de las mareas se han focalizado en la velocidad de las corrientes que se encuentran en muchas regiones costeras del mundo (Bryden and Couch, 2005). En Reino Unido, los canales entre las islas de Orkney y Shetland experimentan con frecuencia corrientes durante el periodo de mareas vivas de más de 3 ms^{-1}, siendo una opción interesante para desarrollar este tipo de energía (Bryden et al., 1995). Otros lugares indicados para extraer este tipo de energía son Irlanda (O'Rourke et al., 2009), el río Amazonas, el Canal de la Mancha, el Estrecho de Gibraltar (O'Rourke et al., 2010a, Calero Quesada et al., 2014), la Isla Fiji (Goundar and Raffiudein, 2013), el Estrecho de Messina (Amelio et al., 2012), la costa sur de Irán (Rashid, 2012) o Corea del Sur (Jo Chul Hee et al., 2012). En algunos lugares, la extracción de energía marina puede combinarse con dos tipos de tecnologías, como es el caso de los sistemas mixtos de olas y mareas en Reino Unido (Muller and Wallace, 2008). Cabe mencionar que las corrientes en algunos estuarios llegan a alcanzar velocidades de 2 ms^{-1} en mareas vivas por lo que puede ser otra fuente de energía renovable. Tal es el caso del estuario del Severn (Liang et al., 2014), el estuario del Tajo (Lopes de Almeida, 2008; Ceregeiro, 2019), el estuario del Duero (Abreu, 2010) o el Estuario del Guadiana (Calero Quesada et al., 2019). El éxito de las instalaciones que aprovechan la energía de las corrientes depende del acceso a una red asequible y suficiente. Por tanto, construir líneas de transmisión resulta más atractivo en zonas costeras que en lugares dispersos debido al menor coste económico y de mantenimiento de la red (Pearce, 2005).

Existen diferentes sistemas de conversión de energía: dispositivos rotativos y dispositivos alternativos. Los últimos son aquellos dispositivos formados por alerones que basculan alternativamente debido al paso del flujo pero en este trabajo no se profundiza en ellos. Los dispositivos rotativos, denominadas turbinas de corriente marina (MCT de aquí en adelante), tiene la misma base física y tecnológica que las usadas para extracción de energía del viento. La potencia generada es directamente proporcional a la densidad del

fluido y al cubo de la velocidad. Las corrientes oceánicas suelen tener un orden de magnitud menor que la velocidad del viento, pero la densidad del agua del mar es aproximadamente tres órdenes de magnitud mayor que la densidad del aire y, por lo tanto, la energía generada es del mismo orden de magnitud en ambos ambientes. Las MCT pueden tener dos configuraciones diferentes. La primera de ellas es la turbina axial (Figura 3.1a), la más empleada, donde el eje gira horizontalmente paralelo al flujo de corriente y con una configuración especial de las palas que puede operar en flujos opuestos. La segunda de ellas es la turbina de eje cruzado (Figura 3.1b) donde el eje principal es vertical y las palas son perpendiculares a la corriente principal, pudiendo operar con un flujo en cualquier dirección (CSIRO, 2012; O'Rourke, 2010a).

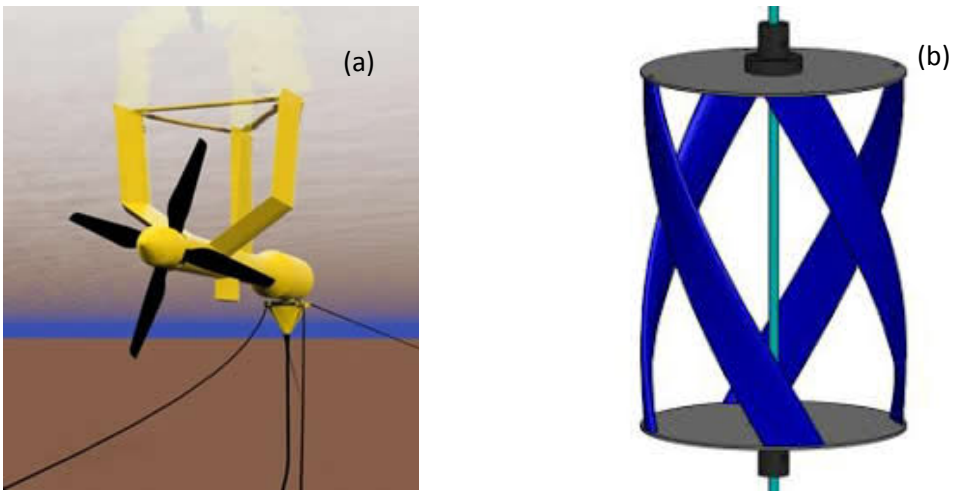

Figura 3.1.- Panel a) Turbina Evopod como ejemplo de turbina axial o de eje horizontal (http://www.oceanflowenergy.com/Evopod-Technology.html). Panel b) Turbina Gorlov como ejemplo de turbina de eje vertical (Niblick, 2012).

El modelo Mohid ha sido implementado con un módulo que simula una granja de turbinas de tipo axial (Balsells Badia, 2019). Dicho módulo proporciona un enfoque sobre la energía que se puede extraer de las corrientes marinas y el impacto de las MCTs en el flujo. Las principales consideraciones en el diseño de estas MCTs es que pueden operar en ambas direcciones y tienen rotación libre del eje vertical haciendo que la velocidad de la corriente sea siempre perpendicular a las palas. Existen varios enfoques para modelar los efectos de las turbinas en modelos hidrodinámicos, la mayoría de ellos se basan en la misma premisa, representan las turbinas como un sumidero de impulso añadiendo una fuerza de reacción en la hidrodinámica del modelo.

La extracción de energía de las corrientes marinas depende del emplazamiento (O'Rourke et al., 2014). Es importante conocer la hidrodinámica del área donde se va a extraer energía para la elección del prototipo más adecuado que puede ser adaptado *ad hoc* para

un uso óptimo. Igualmente permite conocer y evaluar de antemano los efectos en la hidrodinámica de los diferentes tipos de dispositivos (García Oliva et al., 2017; Ramos e Iglesias, 2013). Los estuarios son sistemas hidrodinámicos muy sensibles a cualquier tipo de cambio luego la correcta elección del dispositivo así como el emplazamiento son aspectos esenciales a tener en cuenta previos al diseño de una granja de turbinas (Bryden y Couch, 2005).

La energía de las mareas tiene la ventaja de ser más predecible que la del viento, apenas se ve influenciada por condiciones meteorológicas y está disponible a cualquier hora del día, a diferencia de la energía solar. A pesar de esto, la tecnología que desarrolla la energía mareomotriz se encuentra actualmente en fase piloto o son proyectos de investigación (O'Rourke et al., 2010a) que aún tienen que irrumpir en el mercado comercial, hecho que se retrasa debido principalmente a sus costos actuales.

3.2.- Corrientes marinas en el Estrecho de Gibraltar

El Estrecho de Gibraltar (SG de aquí en adelante) contiene áreas donde las corrientes oceánicas son fuertes, con velocidad de hasta 2 ms^{-1} (Candela et al., 1990; Sánchez Román et al., 2009) al igual que en Irlanda (O'Rourke et al., 2010b), algo menos que los 3 ms^{-1} que se alcanzan en el Estrecho de Messina (Amelio et al., 2012). En cualquier caso esas corrientes lo hacen apto para instalar granjas marinas. El SG es el escenario de un intercambio bidireccional de marcada variabilidad espacial inducida por la interacción del flujo con las diversas limitaciones topográficas como el Estrechamiento de Tarifa (TN, de aquí en adelante), el umbral de Camarinal (CS) y el umbral de Espartel (ES) (García Lafuente et al., 2000; Bruno et al., 2002; Bryden y Kinder, 1991; Delgado et al., 2001) mostradas en la figura 3.2. El agua del Atlántico, menos salina y más cálida, fluye en superficie hacia el Mediterráneo, mientras que una corriente profunda del Mediterráneo, más salada y más fría, desemboca en el Atlántico. Por lo tanto, los flujos en el Estrecho ocurren principalmente a lo largo de su eje en dos orientaciones principales: 10 - 15º desde el este en sentido antihorario y 190 - 195º, la orientación opuesta.

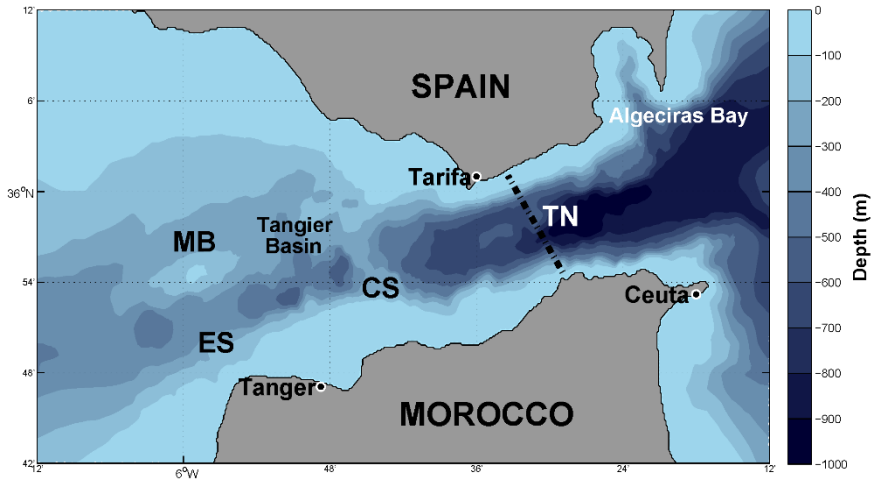

Figura 3. 2.- Batimetría del SG mostrando los topónimos mencionados en este estudio: ES es el umbral de Espartel, CS el umbral de Camarinal y TN para el Estrechamiento de Tarifa, el tramo más estrecho del Estrecho de Gibraltar, MB es el Banco Majuan. Figura tomada del Capítulo 5.

Los modelos numéricos (Sánchez Román et al., 2009; Sannino et al., 2002, 2004; Sánchez Garrido et al., 2011), teóricos (Bryden, 1991; Armi y Farmer, 1988; García Lafuente y Criado Aldeanueva, 2001) y experimentales (Sánchez Román et al., 2011; García Lafuente et al., 2000; Armi y Farmer 1988) sugieren que TN ejerce control hidráulico en el flujo de entrada mientras que CS y ES lo hacen en el flujo de salida, ofreciendo un escenario de intercambio controlado hidráulicamente.

Este intercambio bidireccional está fuertemente modulado por mareas que son lo suficientemente intensas como para revertir el flujo instantáneo en la mayoría de las áreas y profundidades del Estrecho dos veces al día y desbordar el control hidráulico en el CS (Sánchez Román et al., 2011; García Lafuente et al., 2000; Sannino et al., 2004; Armi y Farmer, 1988). Los controles hidráulicos en TN y ES están mucho menos influenciados por los flujos de las mareas y sus características son casi permanentes (Sannino et al., 2004; Armi y Farmer, 1985,1988). Por lo tanto, la corriente atlántica superficial al este de TN sigue fluyendo hacia el este de forma cuasi permanente mientras que el agua profunda del Mediterráneo hace lo mismo en la dirección opuesta cerca y al oeste de ES, presentando dos zonas de flujo predominantemente unidireccional independientemente del forzamiento de la marea (Sánchez Román et al., 2011; García Lafuente et al., 2009; Delgado et al., 2001; Armi y Farmer, 1988).

3.3.- Corrientes en el Estuario del Guadiana

El Estuario del Guadiana (EG) discurre por el suroeste de la Península Ibérica formando la frontera entre España y Portugal. Se trata de un estuario largo y estrecho. Su anchura disminuye exponencialmente de 800 m en la desembocadura a 70 m en su cabecera (Mértola, ver figura 3.3) ubicada a 80 km río arriba (Fortunato et al., 2002; Garel et al., 2009a) donde la marea está completamente amortiguada por una barrera natural (Garel, 2017a; Ruíz Muñoz et al., 1996). La profundidad media del canal es de unos 5 m, pero alcanza los 18 m localmente (Garel et al., 2009a; Garel, 2017a).

La amplitud de las mareas en el GE varía de 1,5 m en mareas muertas a 3,5 m en mareas vivas (Garel y Ferreira, 2013). Las principales constituyentes de marea son M2, S2 entre las semidiurnas y K1 y O1 entre las diurnas (Silva et al., 2000). Esas constituyentes semidiurnas representan ~ 80% de la señal en la desembocadura y que está dominada en gran medida por la constituyente M2 (Garel y Ferreira, 2013). La onda de marea en el GE es una mezcla de onda estacionaria y progresiva (Silva et al., 2003; Garel y Ferreira, 2013). El desfase entre la pleamar y el pico de corriente es de aproximadamente 2 h en la boca y aumenta hacia la cabecera (Garel y Cai, 2018).

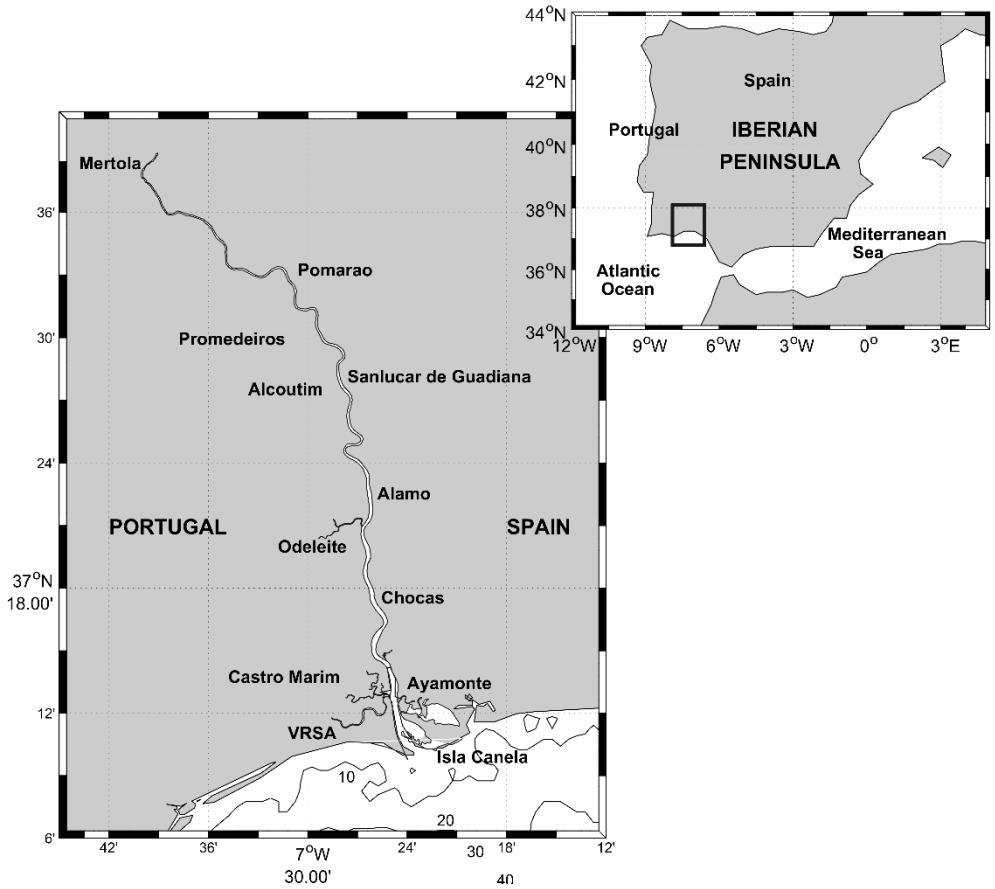

Figura 3. 3. - Mapa del Estuario del Guadiana y su ubicación dentro de la Península Ibérica (ver recuadro). Algunas localidades de España y Portugal se indican en negrita (VRSA significa Vila Real de Santo Antonio). Figura tomada del Capítulo 6.

Históricamente, el régimen de descargas del río Guadiana (Qr, de aquí en adelante) está estrechamente relacionado con los patrones de precipitación regionales. Los períodos prolongados de sequía en verano – otoño se alternan con inundaciones episódicas de corta duración (pocos días) en invierno – primavera. Estos eventos de inundación también se caracterizan por una fuerte variabilidad interanual (Fortunato et al., 2002). Desde la construcción de la presa de Alqueva (2002) ubicada a 60 km aguas arriba de la cabecera, el régimen de Qr ha sido fuertemente regulado, reduciendo su variabilidad interanual y estacional (Dias et al., 2004; Wolanski et al., 2006; Garel y D 'Alimonte, 2017). Para caudales bajos en el estuario, el máximo de velocidad medida como el promedio vertical es de 1 ms^{-1} en mareas vivas y de 0.5 ms^{-1} en mareas muertas en Vila Real de Santo Antonio, situado en la desembocadura (VRSA en la figura 3.3) mientras que la velocidad en las capas superficiales llega a los 2 ms^{-1} como se ha indicado anteriormente (Garel y Ferreira 2013; Calero Quesada et al., 2019).

En los estuarios convergentes, las propiedades que gobiernan la progresión de marea están controladas principalmente por la disminución en la anchura y la profundidad aguas arriba (convergencia morfológica), efectos de fricción y reflexión en el caso de que haya cambios morfológicos abruptos que generalmente ocurren cerca de la cabecera del estuario (Dyer, 1997; McDowell y O'Connor, 1977; Prandle, 2009; Savenije, 2005 y Van Rijn, 2010). Estos factores determinan la evolución espacial de la amplitud y celeridad de la onda de marea, y del desfase entre la marea vertical (nivel del agua) y la horizontal (corrientes) (Jay, 1991; Friedrichs y Aubrey, 1994; Lanzoni y Seminara, 1998; Prandle, 2003, 2004; Savenije y Veling, 2005).

4.- METODOLOGÍA Y OBSERVACIONES

El método utilizado para analizar la viabilidad de una zona está basado en indicadores que cuantifican diferentes características del flujo. El más importante de ellos es la intensidad del flujo, sin el cual no tendría sentido hablar de la instalación de una granja de turbinas. Otros tres indicadores nos proporcionarían información acerca de la rentabilidad de la granja de turbinas, como son el tiempo en que el flujo permanece por encima de un cierto valor umbral, la permanencia del flujo en un sentido y la unidireccionalidad del mismo. Finalmente, otros dos indicadores estarían relacionados con la vida media de los dispositivos al considerar el ruido y la cizalla vertical a la que estarían sometidos los dispositivos. Una función empírica, que se ha denominado función de calidad o viabilidad, reúne toda la información aportada por estos indicadores con diferente peso. Esta función proporciona un valor numérico que permite determinar la viabilidad de una zona según una clasificación (Capítulos 5 y 7).

Se han empleado dos modelos numéricos diferentes: el modelo numérico de circulación general del Instituto Tecnológico de Massachusetts (MITgcm) para el SG y el Modelo Hidrodinámico (MOHID) para el GE, que se detallan a continuación. Ambos modelos fueron validados previamente con medidas *in-situ* tomadas en estaciones de medida instaladas en cada uno de esos entornos. La mayor parte de las medidas provienen de una estación de monitorización desplegada en el umbral de Espartel en el SG y el sistema de monitorización SIMPATICO en el Estuario del Guadiana. Ambas se describen en los apartados 4.4 y 4.5.

4.1.- Modelo MITgcm

Este modelo resuelve completamente las ecuaciones no lineales no hidrostáticas de Navier-Stokes bajo la aproximación de Boussinesq para un fluido incompresible. Se pueden consultar más detalles sobre el modelo en (http://mitgcm.org/sealion/online_documents/node2.html).

La formulación del modelo incluye superficie libre implícita y topografía escalonada parcial (Marshall et al., 1997 a, b). Su dominio (figura 4.1) se extiende desde 6.31W a 4.781W discretizado por una cuadrícula horizontal ortogonal curvilínea no uniforme de 1440 × 210 puntos. La resolución espacial a lo largo del Estrecho, Δx, está entre 46 y 63

m en el área CS y siempre es menor de 70 m entre ES y TN. La resolución espacial a través del Estrecho, Δy, es menos de 340 m en medio del estrecho entre ES y CS, 175–200 m en CS y menos de 200 m entre CS y TN. El modelo cuenta con 53 niveles verticales de 7,5 m de espesor en los 300 m superiores que aumentan gradualmente hasta 105 m de espesor máximo para los 13 niveles restantes más profundos.

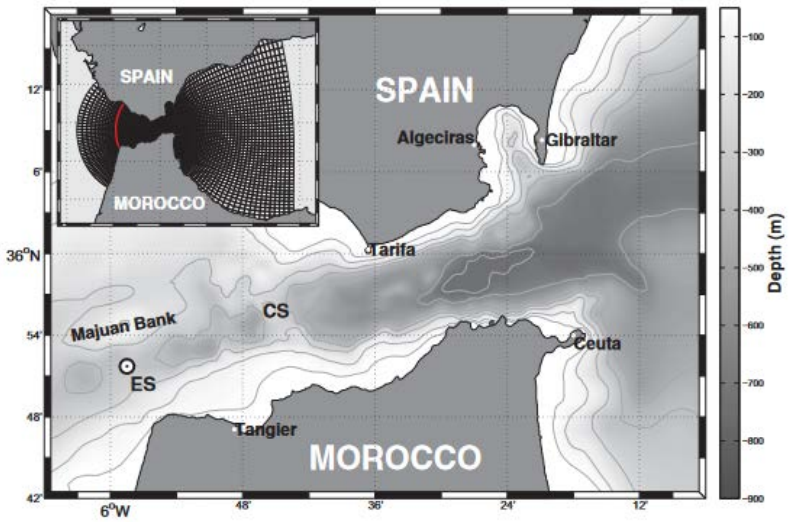

Figura 4. 1.- Batimetría del SG con los principales topónimos y en el recuadro se ha indicado el grid con el que se ha implementado el modelo del MITgcm (Sammartino et al., 2015).

Se usó este modelo en el Estrecho de Gibraltar por haber sido específicamente adaptado para este entorno por Sánchez Garrido ya que para resolver ondas internas de corto periodo (solitones) presentes en el Estrecho de Gibraltar es necesario que el modelo sea no hidrostático (Sánchez Garrido et al., 2011). Las condiciones iniciales de temperatura fueron obtenidas de la base de datos climatológica Medar-MedAtlas (MEDAR Group, 2002) para el mes de Abril. El intercambio bidireccional constante se obtiene forzando lateralmente el modelo con los campos de velocidad temperatura y salinidad medios extraídos de los resultados del modelo desarrollado por Sannino (Sannino et al., 2002) cuyo objetivo era el estudio del intercambio medio de agua a través del Estrecho de Gibraltar y su hidráulica interna. Las reflexiones de ondas en los límites abiertos se minimizaron adoptando el esquema de relajación de flujo propuesto por Carter (Carter and Marrfield, 2007) para el campo de velocidad. El modelo tiene un periodo de 11 días de simulación para lograr el estado estable sin forzamiento de marea. El forzamiento de marea se introdujo imponiendo la corriente de marea barotrópica con las principales constituyentes diurnas (O1, K1) y semidiurnas (M2, S2) en los contornos abiertos, hasta que el modelo alcanza soluciones estacionarias periódicas. Posteriormente, el modelo se

ejecutó durante un mes climatológico para generar salidas de los diferentes campos baroclínicos cada 20 minutos, que es el conjunto de datos analizados en el capítulo 5.

4.2.- Modelo MOHID y batimetría

El sistema hidrodinámico MOHID es un sistema modular de código abierto que comprende modelos numéricos, interfaces gráficas y otras herramientas de pre y post procesamiento (Braunschweig et al., 2004; Miranda et al., 2000; MOHID, 2002). El código está escrito en Fortran usando una estrategia de programación orientada a objetos. El paquete MOHID incluye un módulo GIS que maneja datos de variables espaciales y temporales en formatos específicos requeridos o producidos por MOHID, MOHID GIS (Braunschweig et al., 2005). MOHID Water es un modelo hidrodinámico en 3D desarrollado para simular masas de agua superficiales utilizando el método de volúmenes finitos en el dominio real sin ninguna transformación espacial (Martins et al., 2001).

La batimetría consiste en una malla curvilínea que se extiende 300 m desde la plataforma continental y 80 km tierra adentro hasta la ciudad de Mertola (Capítulo 4). Los bordes de la cuadrícula curvilínea se ajusta con precisión a los márgenes del estuario lo que resulta en menos celdas de cuadrícula no utilizadas y una precisión en las partes más estrechas que más interesan del dominio mayor que lo que harían las mallas rectangulares (Basos, 2013). Este tipo de mallado es particularmente adecuado para canales serpenteantes largos y estrechos como el GE y para todos los sistemas costeros en general (Blumberg et al., 2000). En algunas celdas, el valor de profundidad se manipuló de manera realista utilizando MOHID GIS durante el paso de calibración del modelo para mejorar la concordancia con las observaciones. La batimetría final del dominio se presenta en la figura 4.2.

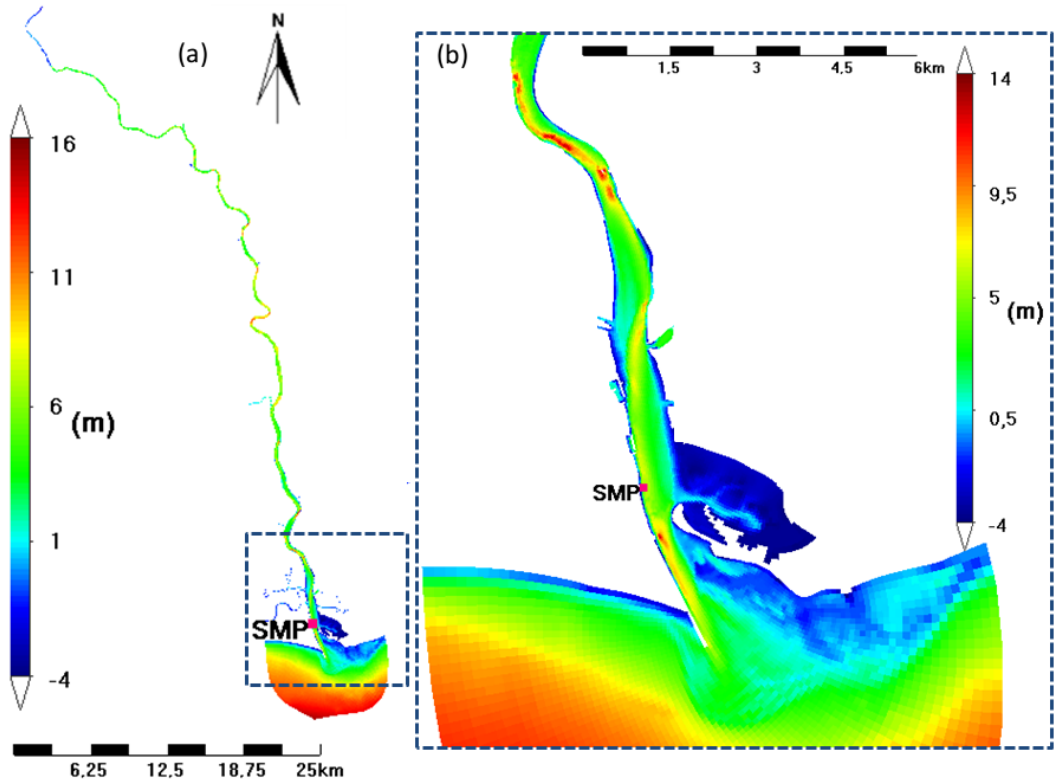

Figura 4. 2.- Panel a) Batimetría introducida en el dominio en el modelo MOHID (la escala de colores aparece en la izquierda). El contorno de 0 m se corresponde con el cero hidrográfico y los valores positivos (colores del cian al rojo) son las profundidades por debajo del cero hidrográfico mientras que los valores negativos (azul intenso) están por encima de dicho cero. Panel b) Zoom de la parte baja del estuario. La escala de colores indica las profundidades del estuario referenciados al cero hidrográfico de forma similar al del panel a). En ambos paneles se ha indicado la localización del sistema de monitorización Simpático, SMP. Figura tomada del Capítulo 6.

Con las observaciones disponibles se realizó la calibración y la validación para distintos subconjuntos de datos (del 1 al 15 de agosto de 2015 y del 16 al 31 de agosto de 2015, respectivamente). El coeficiente de fricción del fondo y los parámetros de viscosidad se ajustaron para coincidir con la propagación y deformación observadas en la onda de marea. El ajuste se llevó a cabo analizando la amplitud de la oscilación del nivel del agua y la fase de diferentes constituyentes de marea, especialmente la constituyente principal semidiurna, M2. Los valores finales adoptados para el coeficiente de fricción, la viscosidad y otros parámetros como el tamaño de la malla y el paso de tiempo se muestran en la Tabla A3 del capítulo 6. La validación se llevó a cabo comparando los datos de salida del modelo con las mediciones *in-situ* disponibles tanto de nivel del mar como de corrientes.

4.3.- Cálculo del flujo de energía

El flujo de energía, E_{flux}, es el primer y más importante indicador de la función de calidad construida. Se ha calculado como:

$$\vec{E}_{flux} = \frac{1}{2}\rho u^2 \vec{u} \qquad (4.1)$$

donde ρ es la densidad del agua del mar, cuyo valor se ha tomado como constante e igual a 1027 kg/m^3 y $\vec{u}$ es la velocidad de la corriente. Tanto en SG y el GE, la corriente discurre en una dirección privilegiada que es la componente longitudinal de la velocidad, siendo la componente transversal muy inferior en tamaño. Por tanto, la expresión (4.1) para calcular el flujo toma la forma:

$$\vec{E}_{flux} = \frac{1}{2}\rho(u_1^2 + u_2^2)\overrightarrow{u_1} \qquad (4.2)$$

donde u_1 es la componente longitudinal y u_2 es la componente transversal de la velocidad de corriente. El flujo por unidad de superficie es una magnitud escalar, sin embargo, se le confiere en las expresiones (4.1) y (4.2) el carácter vectorial para indicar que sigue la misma dirección que la velocidad de corriente y es por ello que en las expresiones anteriores se mantiene como factor $\vec{E}_{flux}$, $\vec{u}$ y $\overrightarrow{u_1}$ en (4.1) y (4.2), respectivamente.

4.4.- Estación de monitorización en el SG

La estación de monitorización se encuentra situada en ES y está instalada para monitorizar el flujo de salida en el SG desde el año 2004 a una profundidad de 360 m. La línea tiene menos de 20 m de altura, está equipada con un Perfilador Acústico de Corriente Doppler (ADCP) integrado en una boya, un sensor de conductividad / temperatura (CT), ambos fijados a lo largo del línea debajo de la boya y un medidor de corriente de un solo punto (Nortek Aquadopp DW). Un ancla de una tonelada aproximadamente mantiene la línea en posición y un disparador acústico y dos balizas ARGOS unidas a la boya completan la línea (García-Lafuente et al., 2020; Sammartino et al., 2015).

La serie temporal de medidas de corriente han sido recogidas durante los Proyectos INGRES, INGRES (REN2003_01608), INGRES2 (CTM2006_02326 / MAR) e INGRES3 (CTM2010_21229 C02-01 / MAR), y Acción Especial CTM2009-05810-E / MAR, financiada por el Gobierno de España. La línea de amarre está incluida en la red

de seguimiento del Mar Mediterráneo del proyecto HYDROCHANGES patrocinado por Mediterranean Science Commission (CIESM). El conjunto de datos CTD / LADCP ha sido proporcionado por el Instituto Oceanográfico Español (IEO) que es socio colaborador del proyecto INGRES3.

4.5.- Estación de monitorización en el GE

El Sistema Integrado de Monitorización de Parámetros TIpo en Áreas COsteras (SIMPATICO) situado en la desembocadura del GE es un ejemplo de tres sistemas de monitorización autónoma situados en diferentes estuarios de Portugal. El sistema permite el acceso remoto a datos medidos *in-situ* con el que se han obtenido series de larga duración de nivel del mar, velocidad de corriente, etc y ha estado funcionando en este lugar desde 2008 hasta 2014.

Este sistema fue adquirido por el Instituto de Investigación Marina (IMAR) a través de un programa nacional portugués para el equipamiento de instituciones científicas (Reeq/484/MAR/2005) a quien agradecemos el acceso a los datos para este trabajo.

5.- ENERGY OF MARINE CURRENTS AND ITS POTENTIAL AS A RENEWABLE ENERGY RESOURCE (Primera publicación)

Artículo publicado en la revista: Renewable & Sustainable Energy Reviews en 2014, 34, 98-109. http://dx.doi.org/10.1016/j.rser.2014.02.038

María Concepción Calero Quesada, Jesús García Lafuente, José Carlos Sánchez Garrido, Simone Sammartino, Javier Delgado.

Physical Oceanography Group, University of Málaga.

Corresponding author: María Concepción Calero Quesada. Campus Teatinos s/n, 29071 Málaga (Spain). Tlf +34952132849.

Keywords: Strait of Gibraltar, Energy Fluxes, Strong, Permanence, Unidirectional.

Abstract

A non-hydrostatic hydrodynamic model of the Strait of Gibraltar with high spatial and temporal resolution has been used to assess suitable areas for energy extraction from marine currents. The model shows great spatial variability of the available energy flux, ranging from 200 Wm^{-2} to more than 1800 Wm^{-2}. In addition to the mean energy flux, other properties and characteristics of the flow such as permanence and direction of the currents, vertical shear or occurrence of unwanted high frequency internal waves have been merged into an index that is used in this work as a proxy for the suitability of a given place to install a power plant. This index highlights two zones gathering the required conditions: the subsurface layer of the eastern half of the strait and the near-bottom layer off Espartel sill at the westernmost gateway of the strait.

5.1. Introduction

Renewable marine energy can be obtained from wind waves and swell, tides, ocean currents and from ocean salinity and temperature gradients. Many different devices are employed at this aim, such as the direct-drive converters that transform the wave mechanical energy in electrical power, the hydrokinetic turbines that convert the kinetic energy of the moving mass of water in electricity in the case of marine currents, or the thermal oceanic plant, producing energy by the thermic differences between deep and surface waters (Bedard et al., 2010). Ocean contains a large amount of unexploited clean renewable energy resources that can play a significant role in the future of worldwide

energy portfolios. This kind of energy will supply future electrical energy needs in the world: the U.S. Electric Power Research Institute (EPRI) and the National Renewable Energy Laboratory (NREL) estimate that the total potential of all the combined ocean renewable energies in United States currently exceeds the national electric energy needs. A total of 13 GW of new hydrokinetic technologies could be deployed by 2025, supplying at least the 10% of the USA electrical needs (Thresher and Musial et al., 2010). Wave and tidal current energy could potentially supply the 15% of the UK's electricity needs (Mueller et al., 2010) and wave energy is likely to have a significant role in Australia electric policy with the highest capacity expected (449 GW from 2023 to 2032) (CSIRO).

Several technologies and devices are currently operating with different efficiency depending on the available energy and the device performance and maintenance (Bedard et al., 2010). The exploitation of renewable energy from ocean waves is widely developed in several countries as Australia, Americas, Portugal, South Africa, parts of Scandinavia, United Kindom (Mueller et al., 2010), Ireland (O'Rourke et al., 2009). Wind waves energy extraction has different technologies (De Falcao, 2010) and modes of operation (Drew et al., 2009) with high energy potential (of the order of TW·yr). Some of the most interesting ongoing projects are the Pelamis Wave Power (PWP) in Portugal (2,25 MW), in Orkney (3 MW) and Cronwall (5 MW) in UK (Burman and Walker, 2010).

Tidal energy resource

Marine currents carry a huge deal of energy, too, but this technology is currently under pilot phase or research projects (O'Rourke et al., 2010a). Some of the most suitable places to extract this type of energy are Ireland, the Amazonas River, the English Channel, the Strait of Gibraltar (O'Rourke et al., 2010b), Fiji Island (Goundar and Raffiuddein, 2013a), the Strait of Messina (Amelio et al., 2012), the southern coast of Iran (Rashid, 2012) or South Korea (Jo Chul hee et al., 2012). Most of the plants are already functioning, as the case of the coast of Welsh (UK) with its 8 MW, while others are currently being completed, as the one in Korea that will supply 300 MW by 2015 (Burman and Walker, 2010). In some places the extraction of marine energy can be combined by two types of energy, as the case of wave and tidal mixed systems in UK Muller and Wallace, 2008).

There are different energy conversion systems in MCTs: rotating devices and reciprocating devices. The extraction of energy from ocean currents by rotating devices

has the same physical basis as the extraction from wind and a similar technology. These are named marine current turbines (MCTs). The generated power is directly proportional to the fluid density and the cube of the speed. In places suitable for the extraction of marine energy, ocean currents are typically one order magnitude less than wind speed, but the sea water density is about three orders of magnitude greater than the air density and, therefore, the power generated is of the same order of magnitude in both environments.

MCTs can have two different configurations: the axial turbines, the most frequently employed, where the axis rotates horizontally parallel to the current stream and, with a special configuration of the blades (variable pitch) can operate in opposite flows, and the cross-flow turbines where the main axis is vertical and the blades are perpendicular to the main stream, being able to operate with flow from any direction (CSIRO, O'Rourke et al., 2010a).

An intense work of design and optimization is currently being developed in this field. While all hydrokinetic devices operate on the same conversions principles regardless of their areas of applications, a set of subtle differences may appear in terms of design and operational features of the farms. These include: design of the turbine (size, directionality and placement), operation (flow characteristics, water density, control resource and prediction) and end-use (grid-connectivity) (Khan et al., 2009). Many studies indicate different types of turbines, for instance, the Evopod tested in Ireland or the Gorlov in USA, or the most promising, Delta Stream Turbine or the Neptune Tidal Stream Device (2.4 MW of capacity) (O'Rourke et al., 2010b).

Several test models claim a superior performance of MCTs located in marine channels than others installed in open flows, the latter being more similar to windmills, resulting in an increase of both average and peak power coefficient (Goude and Agren, 2017). In general MCTs present more technical limitations than wind turbines: the closer proximity of the sea surface and the seafloor (Grogan et al., 2018), the damages on the turbine blades caused by cavitation (Grogan et al., 2018) and other effects related to the higher density of sea water with respect to the air. In many cases it results in the failure of the device, such as the blade fracture on the Open-Hydro 16-m installed in the Bay of Fundy or the Atlantis AR1000 (Liu and Veitch, 2012). Once the rotor is in motion, the blade section starts to experience a relative component of tidal current velocity at various angles of attack depending of the blade parameters (Goundar and Raffiuddein, 2013b). For all these

reasons, the presence of a strong current and the persistence of a flow in a site are not sufficient conditions to ensure its suitability for the installation of a turbine farm (Bahaj, 2011).

Besides the optimal design of the MCTs or their components, the hydrodynamic interactions between turbines may have significant impact in the efficiency of the devices and the electrical power output decays considerably. The two most important control variables for energy cost are the farm size and the turbine distribution in a farm (Li et al., 2011). Different models are used to find the optimal configuration of tidal turbine farms, by the solution of an optimization problem (Funke et al., 2014). On the other hand, there are different types of devices that operate in specific conditions and prototypes still under development, whose technical characteristics can be adapted to ocean currents. In the plant location such as in Northeast Normal University in China who to avoid disadvantages of existing horizontal axis turbine, such as needing pitch adjusting and efficiency dropping in reverse flow, a flex shaft was adopted in the turbine, attached the horizontal axis turbine always facing towards the flow (Wang et al., 2011). In Ria de Arousa, Spain, a parametric approach based on four performance parameters was proposed to compare two types of turbines, the Evopod and the Gorlov. It was found that the Evopod achieves greater site-specific turbine efficiency and energy output whereas the Gorlov turbine presents higher availability and capacity factors or, in other words, more operation hours and equivalent hours per year, essentially due to its lower cut-in velocity and power rating (Ramos e Iglesias, 2013).

Marine Currents in the Strait of Gibraltar

The Strait of Gibraltar holds areas where ocean currents are strong, around a velocity of 2 m/s (Candela et al., 1990; Sánchez Roman et al., 2009) compared with 3 m/s in the Strait of Messina (Amelio et al., 2012) or about 2 m/s in Ireland (O'Rourke et al., 2010c), which makes it suitable to install power marine farms. The strait is the scenario of a two-way exchange of marked spatial variability induced by interaction of the flow with the several topographic constraints as Tarifa Narrows (TN hereinafter), Camarinal Sill (CS) and Espartel Sill (ES) showed in Figure 5.1 (García-Lafuente et al., 2000; Bruno et al., 2002; Bryden and Kinder 1991; Delgado et al., 2001). Atlantic water, less saline and warmer, flows at the surface into the Mediterranean while a Mediterranean undercurrent,

saltier and cooler, flows out into the Atlantic. Numerical (Sánchez Román et al., 2009; (Sannino et al., 2002; Sannino et al., 2004; Sánchez Garrido et al., 2011) theoretical (Bryden and Kinder, 1991; Farmer and Armi, 1986; García Lafuente et al., 2001) and experimental (Sánchez Román et al., 2009; García Lafuente et al., 2000; Armi and Farmer, 1988) models/analysis suggest that TN exerts hydraulic control on the inflow while CS and ES do so on the outflow, offering a scenario of hydraulically controlled exchange. Therefore, the flows in the strait occur mainly along its axis in two principal orientations: 10º-15º from the east counterclockwise and 190º-195º, the opposite orientation.

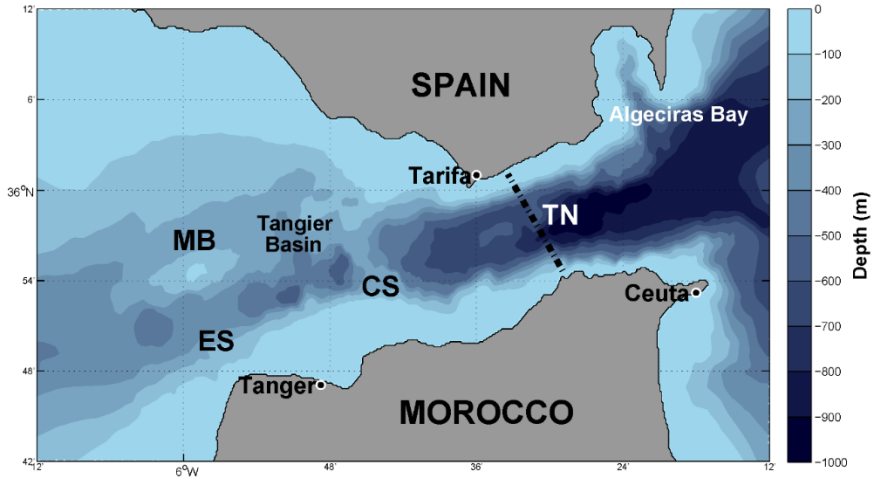

Figure 5. 1.- Bathymetry of the Strait of Gibraltar showing the toponyms mentioned in this study: ES stand for Espartel Sill, CS for Camarinal Sill and TN for Tarifa Narrows, the narrowest section of the strait. The asterisk over Espartel sill indicates the location of a long-term monitoring station mentioned in the text.

This two-way exchange is strongly modulated by tides that are intense enough to reverse the instantaneous flow in most areas and depths of the strait twice a day and flood the hydraulic control at CS (Sánchez Román et al., 2009; García-Lafuente et al., 2000; Sannino et al., 2004; Armi and Farmer, 1988). Hydraulic controls at TN and ES are much less influenced by tidal flows and are quasi-permanent features (Sannino et al., 2004; Armi and Farmer, 1988, 1985). Therefore, the surface Atlantic stream nearby and east of TN keeps flowing eastwards permanently while the deep Mediterranean water does the same to the opposite direction nearby and west of ES, featuring two zones of unidirectional flow regardless of tidal forcing (Sánchez Román et al., 2009; García-Lafuente et al., 2000; Delgado et al., 2001; Armi y Farmer, 1988).

A remarkable feature linked to tides is the formation of a large amplitude internal hydraulic jump over the western edge of CS during the rising tide due to the supercritical-

to-subcritical transition of the Mediterranean undercurrent downstream the sill (Bruno et al., 2002; Sánchez Garrido, 2009; Sánchez Garrido et al., 2008). The jump is released when the Mediterranean current weakens (about 2 hours before high water) and the hydraulic control at CS is lost. It progresses to the Mediterranean as a tidal bore, generating a train of large amplitude, short-period internal waves along its leading edge (Sánchez Garrido et al., 2011; Armi and Farmer, 1988; García-Lafuente et al., 2013) whose associated wave-velocity field induces remarkable fluctuations able to change the total velocity by more than 1 ms^{-1} in few minutes. These fluctuations may be usable or not for extracting energy, depending on the characteristics of the devices (Hanson et al., 2011, 2010) but, in general, of such large amplitude and high frequency oscillations are unwanted for technical reasons and will be considered as noise in the present study (Zhou et al., 2013). Notice, however, that these waves do not fulfill the most important noise characteristic, which is its random nature. Actually they are predictable (Bruno et al., 2002; Sánchez Garrido et al., 2011; Sánchez Garrido et al., 2008; García-Lafuente et al., 2013) because their appearance is strictly linked to tides, an archetypical periodic phenomenon.

Atmospheric forcing also induces moderate fluctuations of the flow speed in the subinertial frequency band (few days to weeks) (Candela et al., 1989; García-Lafuente et al., 2002). The estimation of energy fluxes and their variability in the Strait of Gibraltar should take into account this forcing. However, the subinertial fluctuations occur at relatively low frequency for which the response of the exchange can be considered as a succession of steady-states (quasi-steady fluctuations (Farmer and Armi, 1986). It means that the final solution can be achieved as the linear superposition of the flows exchanged in absence of atmospheric forcing and the barotropic flow induced by that forcing. The situation is completely different in the case of tides because the strength and frequency of tidal flows produce about strong non-linear interactions between mean and tidal flows that invalidate any linear superposition. For this reason, this work focus on the energy fluxes in the strait that is only forced by tides, and addresses the effect of meteorologically induced subinertial fluctuations on these fluxes briefly in section 3.5.

The paper is organised as follows. Section 3.2 describes the high resolution numerical model that has been used, which has been employed in previous studies and has shown to reproduce satisfactorily the hydrodynamics of the exchange at tidal frequencies (Sánchez Garrido et al., 2011). Section 3.3 computes the energy fluxes averaged over

different periods and vertical layers in order to assess the suitability of the different areas of the strait and identify other hydrodynamic parameters of practical relevance for technological issues. In section 3.4 all the previous information is merged into a single quality function that helps identify the most suitable places to install marine-current power plants. The subinertial modulation of the flow is briefly addressed in section 5.5 and conclusions are shown in section 5.6.

5.2. Methodology

In order to obtain a synoptic estimation of the flow in the area of study, aimed at calculating the energy fluxes there, a numerical approach has been applied.

5.2.1. Numerical model

The numerical model is the Massachusetts Institute of Technology general circulation model (MITgcm), which solves the fully non-linear non-hydrostatic Navier-Stokes equations under the Boussinesq approximation for an incompressible fluid. Next we briefly outline the model setup and its initialization for the numerical simulation used in this study. Further details on the model configuration, validation and performance can be consulted in (http://mitgcm.org/sealion/online_documents/node2.html).

The model formulation includes implicit free surface and partial step topography (Marshall et al., 1997a, 1997b; García-Lafuente et al., 2013) and its domain extends from 6.3ºW to 4.78ºW that is discretized by non-uniform curvilinear orthogonal horizontal grid of 1440 x 210 points. The along-strait spatial resolution, Δx, is between 46 and 63 m in CS area and is always less than 70 m between ES and TN. The across-strait spatial resolution, Δy, is less than 340 m in the middle of the strait between ES and CS, 175-200m in CS and less than 200 m between CS and TN. The model has 53 vertical levels 7.5 m thick in the upper 300 m that increases gradually until 105 m maximum thickness for the remaining 13 deeper levels.

The initial conditions of temperature and salinity were derived from the climatologic Medar- MedAtlas Database (MEDAR Group, 2002) for the month of April. The steady two-way exchange is obtained by laterally forcing the model with the mean velocity, temperature, and salinity fields extracted from the outputs of the model developed by

Sannino et.al. (Sannino et al., 2002), which aimed at the study of the mean water exchange through the Strait of Gibraltar and its internal hydraulics. Wave reflections at the open boundaries were minimized adopting the flow relaxation scheme proposed by Carter (Carter and Marriefield, 2007) for the velocity field. A spin-up period of 11 days of simulation was necessary to achieve the steady state without tidal forcing. Subsequently, tidal forcing was introduced by imposing the barotropic tidal current of the main diurnal (O1, K1) and semidiurnal (M2, S2) constituents at the open boundaries and leaving the model to reach a periodic stationary solutions, which was achieved after 8 days approximately. Then the model was run during a climatological month to generate outputs of the different baroclinic fields every 20 min, which is the dataset analyzed in this study.

A similar approach has been employed by the Georgia Tech Research Corporation who utilized a ROM system to obtain the intensity of tidal currents in United States (Kevin et al., 2011; http://www.tidalstreampower.gatech.edu/).

5.2.2. Energy flux computation.

The along-strait component of the energy flux has been computed according to:

$$E = \frac{1}{2}\rho(u^2 + v^2)u \qquad (5.1)$$

where u is the along-strait component of the velocity, v the cross-strait component and ρ the density of sea water that, for the purposes of this study, has been taken as constant (ρ = 1027.5 kg m^{-3}). The across-strait component could be calculated similarly but the prevalence of along-strait over cross-strait velocity makes that component negligible. Only the along-strait energy flux is considered in the subsequent calculations.

The energy flux has been calculated at each point of the 3D grid. These values have been vertically averaged in the layers defined in Table 3.1. The upper part of the water column, (0 - 26.25) m, has been excluded since it is not exploitable for maritime safety reasons. Although the Strait of Gibraltar holds areas deeper than the last layer in the Table 5.1, they are not of practical interest because of the great depth and the weakness of the currents. The contoured energy flux at k-th vertical layer has been then computed as

$$E_k(x,y) = \frac{1}{N_k}\frac{1}{N_t}\sum_{i=1}^{N_t}\sum_{j=1}^{N_k} E(x_j, y_j, z_j, t_i) \qquad (5.2)$$

where N_t is the number data within the selected time intervals and N_k is the number of grid points within vertical layer k. Obviously the estimated energy flux depends on the interval over which the time average is carried out.

Table 5. 1.- Layers and their range depth used for the vertical average of the energy flux. Last column indicates the number of grid points inside each layer.

Layer	*Range depth(m)*	*Grid points*
1	26.25 - 71.25	7
2	71.25 - 116.25	7
3	116.25 - 161.25	7
4	161.25 - 206.25	7
5	206.25 - 273.75	10
6	273.75 - 326.25	6
7	326.25 - 532.50	6

5.3. Flow characteristics

With regards to the suitability of a marine region for renewable energy, the most important variable is the available energy flux in the zone although there are also other characteristics of the flow that are relevant. All they are addressed in the next subsections.

5.3.1. Averaged energy fluxes

Figure 2 shows the temporal mean value of the energy flux in the selected layers (actually, the mean value of the climatic April used in the simulation). The mean has been computed using absolute values (the energy flux in equation (5.1) is positive (negative) if the flow moves to the east (west) in order to determine an upper bound to the available energy flux.

Layer 1 (Figure 5.2a) presents moderate values over the central area of the strait associated with the Atlantic inflow and larger fluxes over CS. Layers 5 and 6 show the highest fluxes in the western part of the strait, in the Mediterranean outflow (Figures 5.2e, f). Values in the intermediate layers 2 to 4 are low except in a narrow band over CS (Figures 5.2b, c, d) because they embrace partially the interfacial layer where the velocity is small. Layer 7 (Figure 5.2g) also shows very reduced values in the eastern half of the strait, where the Mediterranean outflow moves to the west slowly, and high values west of ES where the outflow plunges down in the Atlantic Ocean as a density current. This short overview indicates that layers 1, 5 and 6 deserve further analysis while the

remaining layers are of secondary relevance and are no longer considered. Layer 5 shows spatial patterns very similar to layer 6, a reason for which -and for the sake of conciseness- we hardly present maps for that layer.

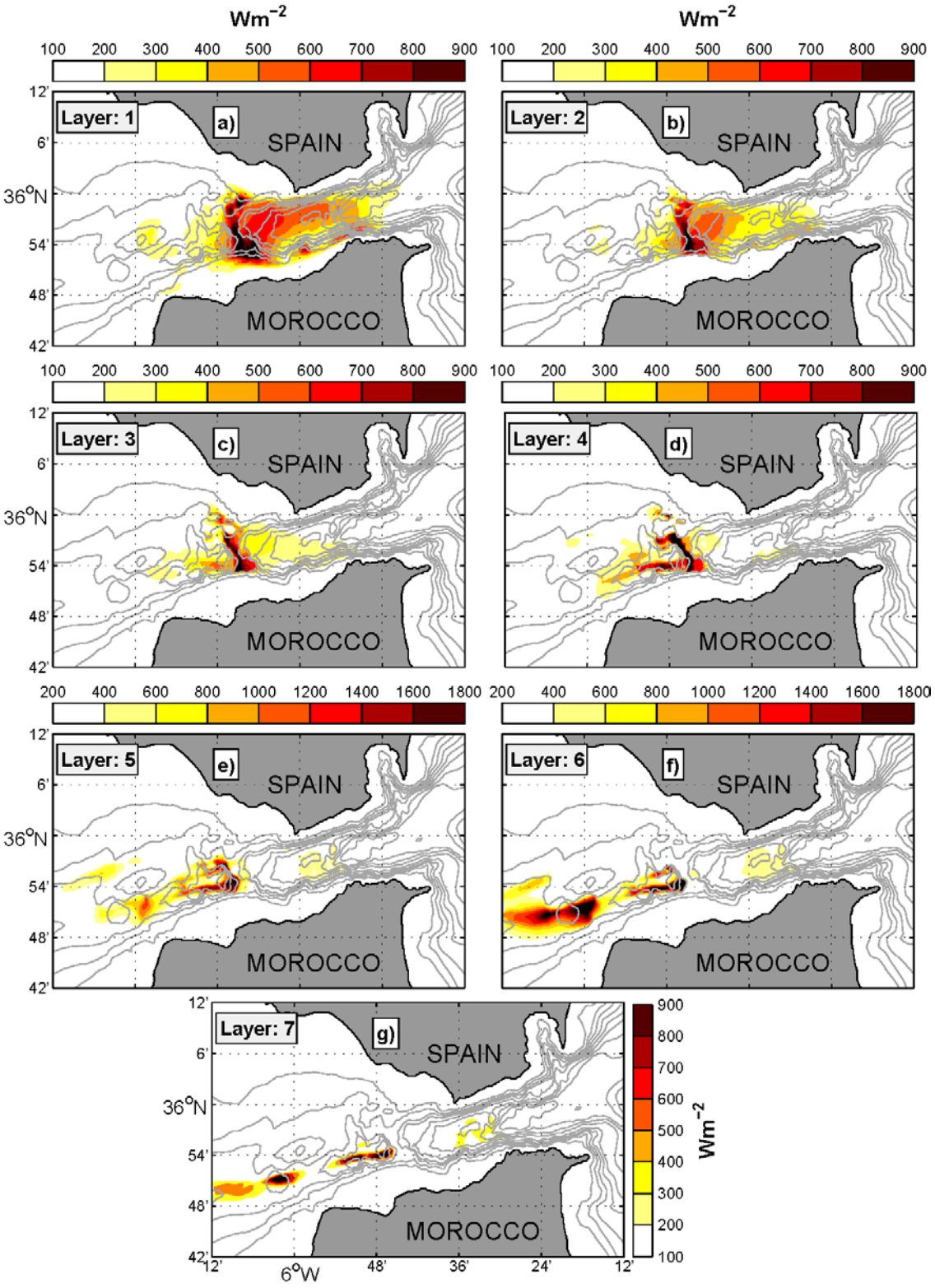

Figure 5. 2.- Mean energy flux in the layers indicated in Table 5.1 and shown in the insets. The colour bar, common for all panels, indicates the energy flux in Wm^{-2}.

5.3.2. Other relevant parameters (indicators)

The preliminary analysis carried out in the previous section hides the high spatial-temporal variability of the flows and, hence, energy fluxes in the strait. See, for instance, the fortnightly variation of the energy flux in layer 1 from spring (Figure 5.3a) to neap (Figure 5.3b) tides. Figures 5.3c and 5.3d show that the energy flux in this layer is mainly achieved by positive (towards the Mediterranean Sea) flows while it diminishes if only periods of negative, westward flow are considered in the time average.

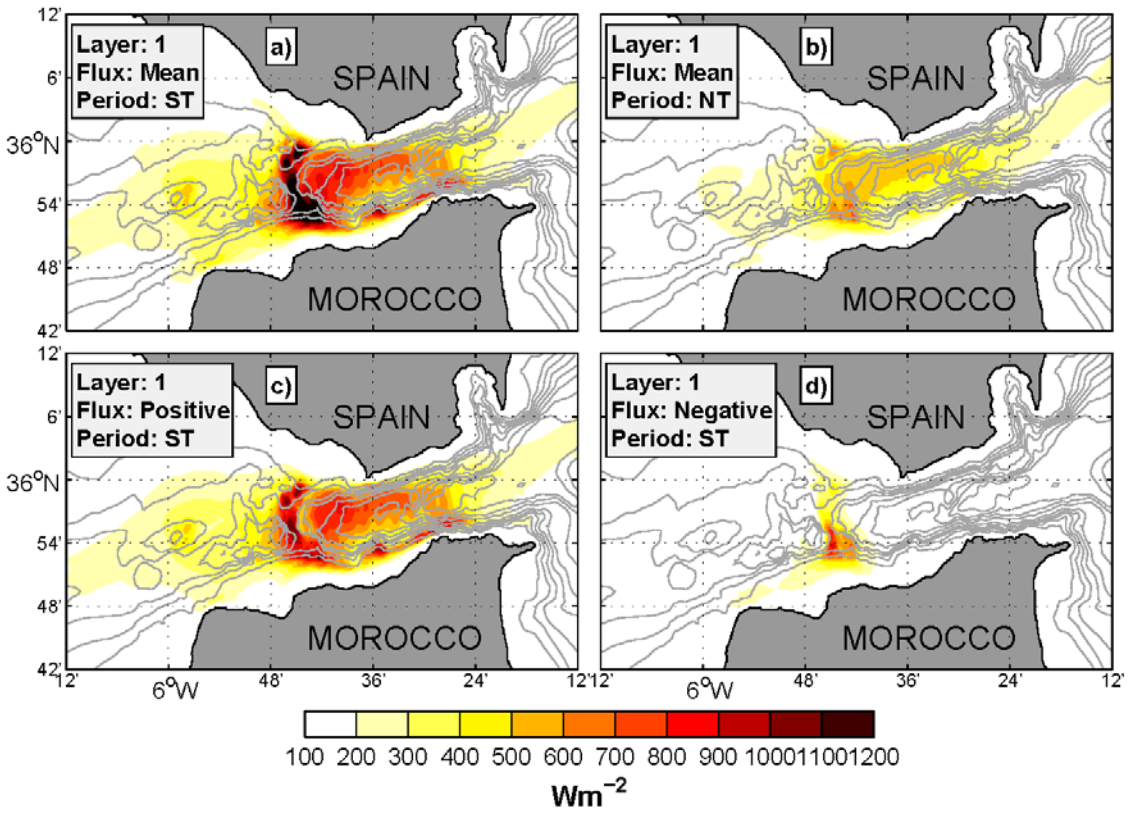

Figure 5. 3.- Panels a) and b): Mean energy flux in layer 1 during spring (ST) and neap tides (NT), respectively. Panel c) and d): Mean energy flux associated with positive (eastward) and negative (westward) flow during ST period.

A fundamental aspect in the installation of turbine farms is the selection of the technology employed, namely, the MCTs. For these reasons and regarding the performance of the devices, it is certainly worth analyzing other time-varying parameters of the flow, rather than only the energy flux as done in (Kevin et al., 2011, http://www.tidalstreampower.gatech.edu/). Five of such time-varying parameters are considered in this study. The time interval over which we have calculated their values is the whole month of the model.

5.3.2.1.- Time interval during which the energy flux is above a threshold value (TAT).

Many kinds of MCTs have a threshold speed below which they are not energetically efficient and it is therefore reasonable to define a parameter that accounts for this limitation. Time interval during which the energy flux is above a threshold value (TAT) is expressed as the percentage of time that the energy flux holds above the selected threshold, which in this study has been set to 200 Wm^{-2} corresponding to a flow speed of 0.73 ms^{-1} according to equation (5.1). Figure 5.4 presents the spatial distribution of TAT in layers 1 and 6, which are the only ones that show values above 50% over an extended area. Layers 2, 3 and 4 (not shown) have patterns similar to layer 1, with smaller percentages over a smaller area (basically CS), while layer 5 (not shown) recalls layer 6 with significantly lower percentages. Regarding this indicator, the zone of ES exhibits the best conditions, with percentages over 90% in area of approximately 60 km^2.

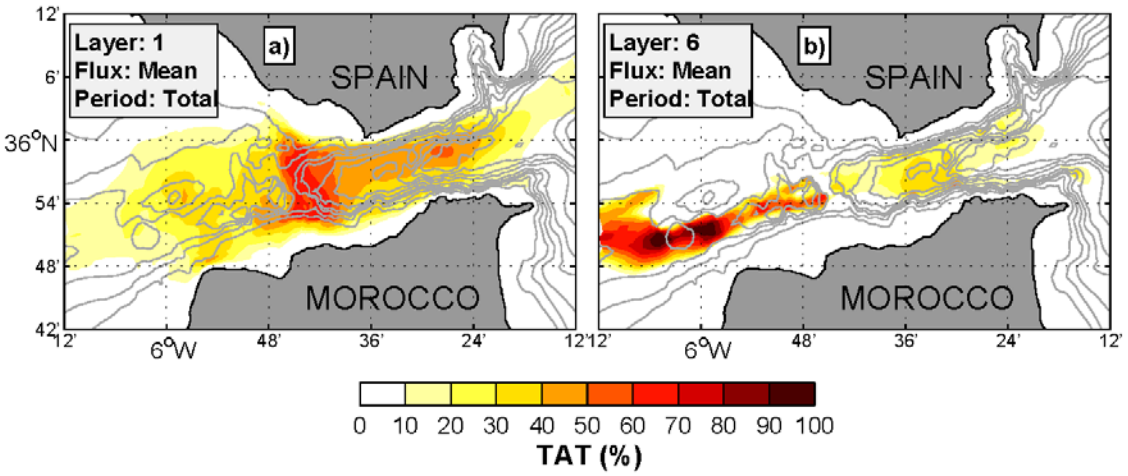

Figure 5. 4.- Percentage of time when the mean energy flux (TAT parameter in the text) is greater than 200 W m^{-2}. Panel a) is for layer 1 and panel b) is for layer 6.

5.3.2.2.- Time interval during which the energy flux does not change sign (TFP).

Some devices only extract energy from marine currents when they are oriented upstream, that is, when they are pointing to the direction the current comes from (O'Rourke et al, 2010a). The time interval during which the energy flux does not change sign (TFP) is of interest for such devices whenever they are mounted on structures that keep them facing at a fixed, pre-selected direction. TFP is also expressed as a percentage.

Figure 5.5a presents the TFP of positive sign in layer 1, that is, the percentage of time the current in this layer flows towards the Mediterranean. As expected here, TFP is higher than 50% everywhere in the strait area (any value below 50% would indicate a prevalence of westward flow) with enhanced values in the eastern half of the strait due to the internal hydraulics of the exchange. The opposite is observed in the deep layer 6 (Figure 5.5b) where TFP is nearly 90% for negative flow (towards the Atlantic) in the west half of the strait and, particularly, over ES area, remaining above 50% elsewhere.

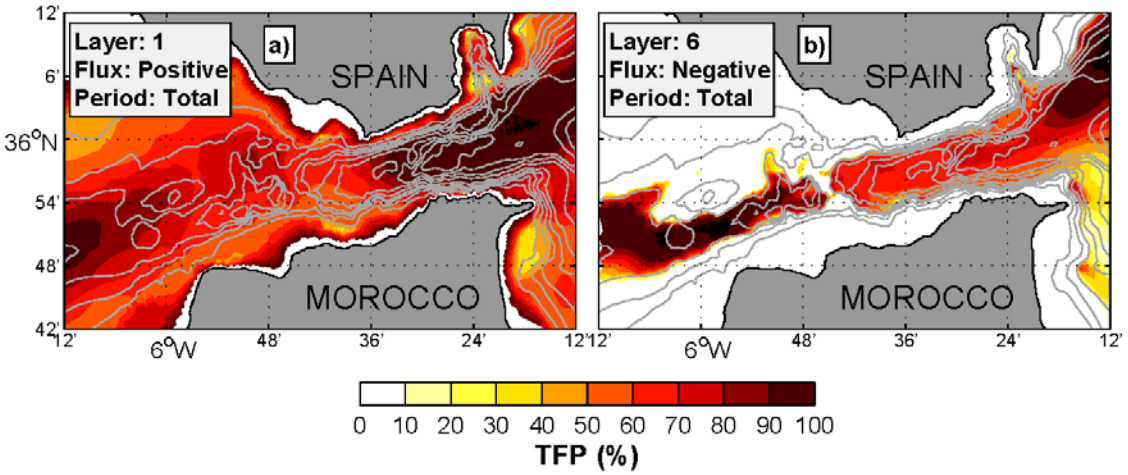

Figure 5. 5.- Percentage of time during which the energy flux does not change sign (TFP parameter in the text). Panel a) corresponds to positive (eastward) energy flux in layer 1. Panel b) is negative (westward) energy flux in layer 6.

5.3.2.3.- Time interval during which the flow lays along a given direction (TFU).

Even when the energy flux does not change sign, the direction of the flow can fluctuate, decreasing the efficiency and performance of the device (Li et al., 2011). A suitable condition is that the flow keeps tight along a favoured direction, which obviously would be the axis of the strait in this case. Again, Time interval during which the flow lays along a given direction (TFU) is expressed as a percentage. Two directions have been considered with an angular tolerance of 25º: the first one towards the Mediterranean along the axis, whose limits have been set to [-25º, 25º] and the second one towards the Atlantic within the interval [160º, 210º]. Although this parameter overlaps with TFP, it is more restrictive and identifies areas of rather unidirectional flows, a very crucial condition for the aforementioned devices (O'Rourke et al., 2010a, Goundar and Raffiuddein, 2013b).

Figure 5.6a, which shows TFU in layer 1, indicates that in the central channel the average energy flux is mainly towards the Mediterranean, the percentage increasing to almost 90% to the East of TN. Recalling the results shown in Figure 5.5a it is clear that the positive energy flux in this area is very directional, with only small fluctuations around the direction of the axis of the strait. Over CS, the TFU percentage is around 50%, significantly less than the ~70% of TFP there visible in Figure 3.5a. Instead, the direction of the flow over CS has greater fluctuations than in the eastern strait, which makes CS a less suitable area regarding this parameter. Figures 5.6b and 5.6c present TFU in layers 5 and 6, respectively. As expected, the general pattern is the opposite to layer 1 with negative flows most of the time, particularly in the central channel. The percentage in layer 6 reaches nearly 100% in ES area and it is slightly less in layer 5. Over CS, TFU is around 50% (Figure 5.6b), which indicates important fluctuations of the flow direction, much like the case of layer 1 already discussed. In summary, the eastern part of the strait in layer 1 and the western part in lower layer 6 are the best areas regarding TFU, a non surprising result that stems from the hydraulic control associated with the internal hydraulics of the strait (Sannino et al., 2004; Armi y Farmer, 1985, 1988).

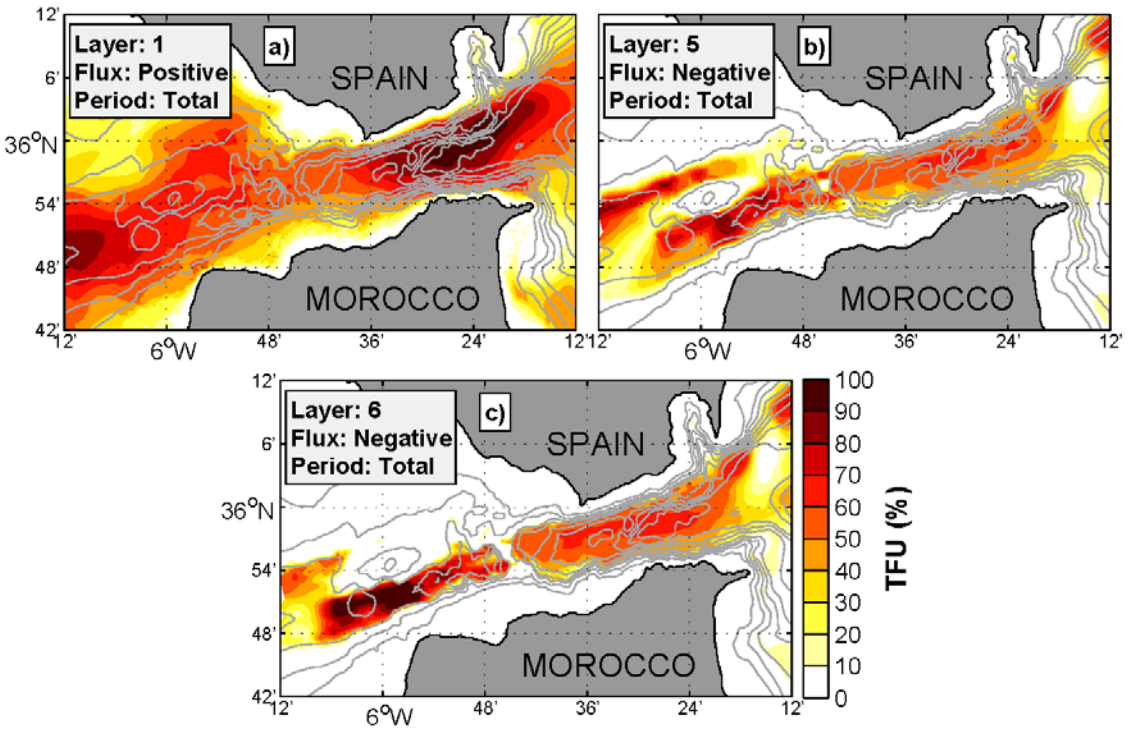

Figure 5. 6.- Percentage of time during which the energy flux keeps the direction within given intervals (TFU parameter in the text). Panel a) is the case of energy flux toward the Mediterranean Sea within [-25º, 25º] in layer 1. Panel b) is the same for layer 6 within the interval [160º, 210º] (towards the Atlantic Ocean).

5.3.2.4.- High frequency phenomena or noise (FN).

As mentioned in Introduction, the high frequency internal waves periodically generated in the strait may contribute negatively to the mean lifetime of some devices due to the rapid fluctuations of the velocity field. For this reason they can be considered as noise, which has been quantified as the root mean square of the high-pass velocity series obtained after filtering the original series with a numerical filter of 2 h^{-1} cut-off frequency. This indicator, high frequency phenomena (FN), has therefore units of m s^{-1}.

Figures 5.7a and 5.7b show FN in layers 1 and 6, respectively. It is well-known that internal waves are mainly found in the eastern half of the strait progressing to the Mediterranean from CS, where they are generated. Figure 5.7a clearly reflects this fact and shows that FN in the upper layer 1 concentrates at east of CS. Similar patterns are found in layers 2 and 3 (not shown) with FN decreasing toward the seafloor in this area. From layers 4 to 6, the spatial pattern changes and FN starts showing significant values west of CS due to supercritical-to-subcritical flow transitions that takes place in the Tangier Basin (Sánchez Garrido et al., 2011; Armi y Farmer, 1988; García-Lafuente et al., 2013). Figure 5.7b illustrates this feature and also (and more importantly) that FN is reduced drastically over ES to increase again westwards of this sill due to new hydraulic transitions (Sánchez Garrido et al., 2011).

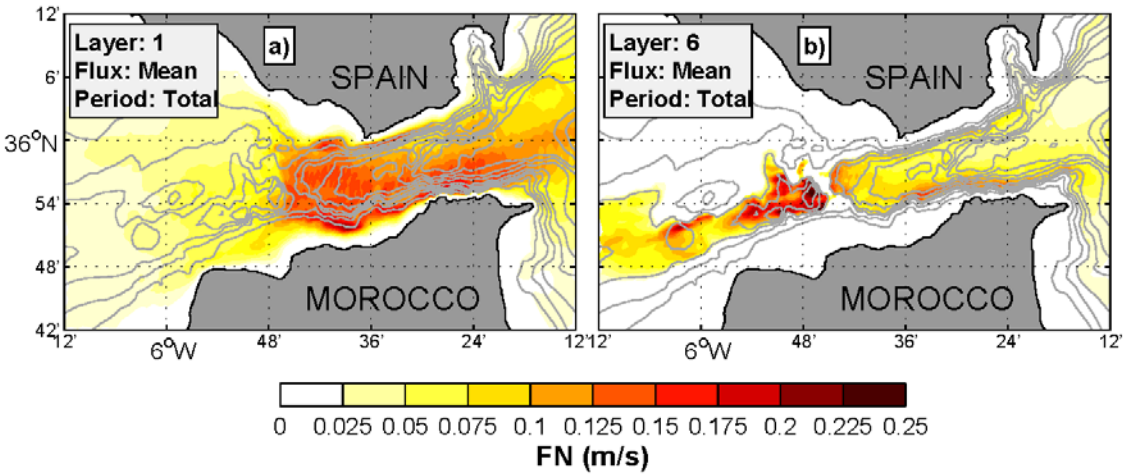

Figure 5. 7.- Noise or RMS high frequency velocity (FN parameter in the text). Panel a) is for layer 1 and panel b) is for layer 6.

5.3.2.5.- Vertical shear of the flow (FS).

Blades of a wind-like turbine, working undersea, are subjected to forces typically 10 times stronger than the ones undergone in air. The mean lifetime of the turbine, especially of those with horizontal axis depends on vibrations supported by the rotor axis, which are enhanced in sheared flow. Vertical shear of the flow (FS) measures the maximum shear within each layer in s^{-1}.

The main source of vertical shear is the bottom friction and only those layers involving the presence of the seafloor show relatively large values of FS. A good example is layer 1 (Figure 5.8a) that shows only two near shore spots in CS area where FS is important, and both sites are located over the shallow seafloor. Another example is layer 6 (Figure 5.8b) where FS is relatively large in ES and to the west (the only places where the flow feels the seafloor) and nearly null elsewhere.

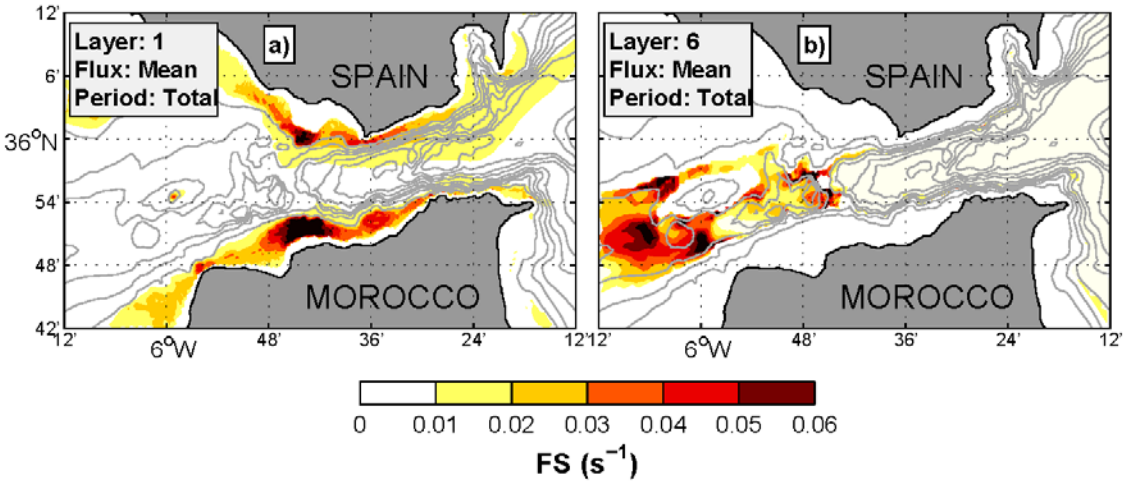

Figure 5. 8.- Velocity shear (FS parameter in the text). Panel a) is for layer 1, panel b) is for layer 6.

5.4. Assessing of suitability of the different areas.

Table 5.2 summarizes the findings discussed in previous section following a subjective qualification. The areas with a priori favorable conditions for installing marine turbine farms have been identified for each of the most suitable layers 1, 5 and 6 (column 2 in Table 5.2). Layer 1 shows good conditions in the eastern part of the strait and also over CS while flow properties in layers 5 and 6 are much better in the western half of the strait, particularly over CS (layer 5) and ES (layer 6). Conditions over ES in layer 5 are also

favourable although to a lesser extent than in the underlying layer 6, a reason for which ES is not included in layer 5 in Table 5.2.

Table 5. 2.- Quality assessment of the variables and indicators in the favourable locations discussed in the text. The first column indicates the layer (See Table 5.1), the second column specifies the most suitable locations in each layer and the remaining columns refer to the different indicators, which have been rated according to A=very good/excellent; B= good; C= medium; D= poor.

Layer	*Selected area*	*I*	*Indicators*				
			TAT	*TFP*	*TFU*	*FN*	*FS*
1	*TN*	B	C	A	A	D	B
	CS	A	B	C	C	D	B
5	*CS*	A	C	B	B	C	B
6	*ES*	A	A	A	A	B	C

The intensity of the energy flux (*I* hereinafter) is the most important variable to select the right place and Table 5.2 indicates that all locations are rather suitable with regards to this variable, with a slightly disadvantage in the eastern strait in layer 1. CS is a good place in layers 1 and 5 due to the strength currents over the whole water column (CS is the bottleneck of the strait) but it shows weaknesses regarding other indicators. Currents there are mainly bidirectional and but they show high fluctuations around the two main directions (poor rating for TFP and TFU). Moreover the periodic reversal makes TAT diminish. Additionally, CS is the place of internal wave generation, which affect the FN indicator negatively too. Except for the shear, all the defined indicators have low rating. On the contrary, ES have a very good rating for all them (except for the shear) because currents do not reverse (they maintain sign and direction) the flow tends to be supercritical there (Sánchez Garrido et al., 2011; Sannino et al., 2009), which inhibits the upstream propagation of internal waves and, hence, propitiates a very low FN.

5.4.1. Quality function

In order to attempt to extract a single index of suitability from the series of the indicators computed, a quality function has been defined according to the table 5.2 as follows

$$V = [2X_I^2 + X_I(X_{TAT} + X_{TFP} + X_{TFU})](1 - X_{FN})(1 - X_{FS}) \qquad (5.3)$$

where parameters X_{YYY} quantify the different indicators according to Table 5.3. The numerical values of the parameters in this table aim at quantifying the qualitative rating in Table 5.2, assigning the value 0 to qualifier "D", 1 to "C" and so on. There are however exceptions in those parameters that appear less relevant, such as the sign of the flux, X_{TFP}, which only can take the values 0 and 1, or the directionality, X_{TFU}. On the other hand, the first three indicators defined in the previous section (*TAT, TFP, TFU*) are directly related with the capability of the device to optimize the extraction of energy and their assigned indices enter equation (5.3) as summands, while the last two ones (*FN, FS*) are rather related to the mean life of the device and enter the equation as factors. We will call "restrictive" parameters to the first group and "non-restrictive" to the second group.

Table 5. 3.- Numerical values assigned to the parameters (X_{YYY} and X_{YY}) in equation (5.3). The first block is for the restrictive indicators and the second block for the non-restrictive ones (see text). Rows X_{YYY} and X_{YY} in either block show the numerical value of the parameter which depends on the actual of the associated indicators (*I, TAT, TFP, TFU, FN* and *FS*) discussed in the text. For instance, in a place where *TAT* is 65%, its associates parameter X_{TAT} would be 1, if it was 80%, X_{TAT} would be 2, and so on.

		V A L U E			
	(X_{YYY})	*0*	*1*	*2*	*3*
Restrictive	*I (W/m^2)*	<200	[200, 500)	[500, 800)	≥ 800
	TAT (%)	< 50	[50, 75)	[75, 90)	≥ 90
	TFP (%)	< 75	≥ 75	---	---
	TFU (%)	< 50	[50, 80)	≥ 80	---
	(X_{YY})	*0*	*0.10*	*0.15*	*0.20*
Non restrictive	*FN (m/s)*	< 0.05	[0.05, 0.15)	[0.15, 0.25)	≥ 0.25
	FS (s^{-1})	< 0.02	[0.02, 0.04)	[0.04, 0.06)	≥ 0.06

In this function, which is always positive, the energy flux weighs much more than any other parameter, since it is the main variable and appears in the equation in a single squared summand. Other parameter like *TAT* is much interest and it is allowed to range from 0 to 3. The *TFU*, parameterized through X_{TFU}, should have more relevance for those devices that requires uni-directionality of the flow, in which case the function *V* may be biased. Being aware of the difficulty of addressing the large variety of items to be considered in practice, we still consider that the quality function (5.3) summarizes the main aspects to be taken into account for decision-makers and contains enough information to help selecting the best location for energy plants based on marine currents.

The maximum values of function *V* found in the area are slightly greater than 30 and are located principally in the deep layer 6 over ES. Going one step ahead in the interpretation of the numerical values of *V* we could classify the candidate places as unfeasible (*V <15*), acceptable (*15<V <20*), advisable (*20<V <25*), very suitable (*V >25*). Figure 5.9 shows the function *V* in layers 1, 5 and 6, where it reaches values greater than 20 somewhere. It is readily seen that the best conditions (*V >25* or even *V>30*) are met in layer 6 over ES, a conclusion that is easily inferred from Table 5.2 as well. Layer 5 shows good conditions over CS and ES, although it compares unfavorably with layer 6 in this place. CS is also the best place in layer 1 due to the strength of currents, although it is an arguable choice for devices that require uni-directionality. For this kind of devices, ES in layer 6 is the best site by far (Figure 5.6b).

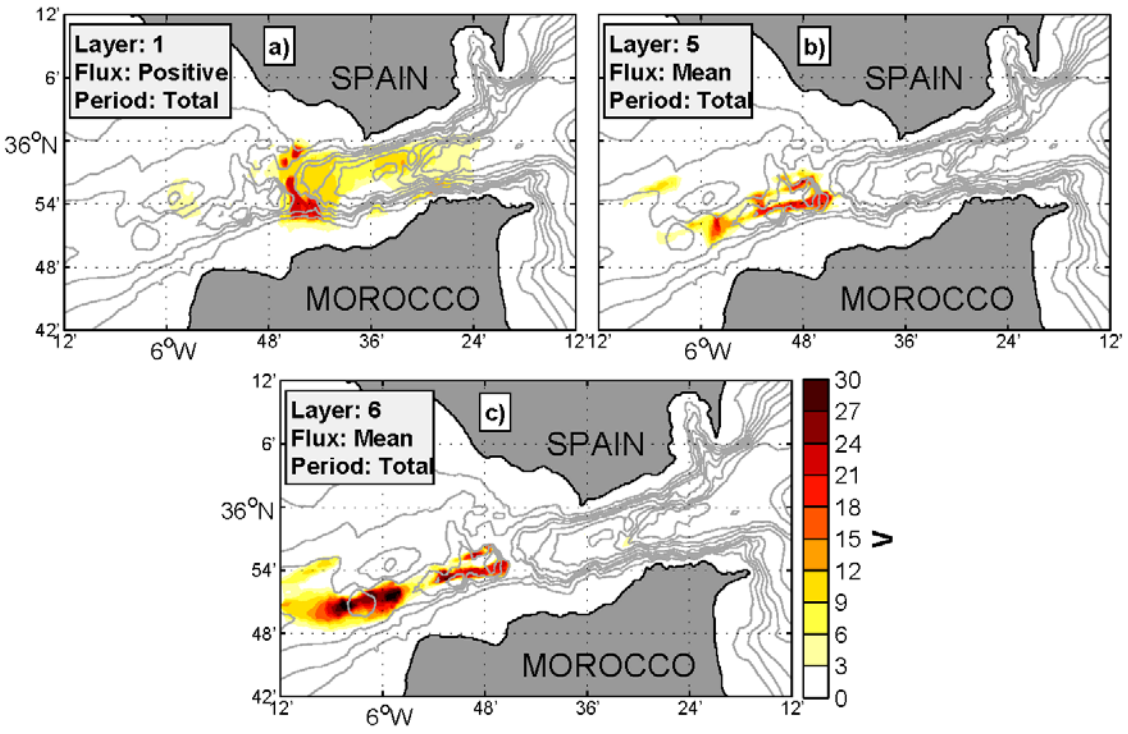

Figure 5. 9.- Quality function (V in the text). Panels a), b) and c) are for layers 1, 5 and 6, respectively.

5.5. Subinertial influence.

As already mentioned, meteorological forcing drives relatively important flow fluctuations at subinertial time-scale, which in turn modifies the averaged energy flux. This section estimates the effect of these fluctuations focusing on layer 6 over ES which,

according to previous section, is the most suitable place from the point of view of the quality function *V* to install a power plant.

At subinertial time-scale, the total flow is well reproduced as the linear superposition of a mean, U_0, and meteorologically induced fluctuations, $\langle U_m(t) \rangle$ (Farmer y Armi, 1986; Candela et al., 1989; García-Lafuente et al., 2002). Under this assumption, $\langle U_m(t) \rangle$ averages to zero in the computation of the long-term averaged flow, and $\langle U_{total} \rangle = \langle U_0 + U_m(t) \rangle = U_0$ ($\langle \quad \rangle$ indicating time average). Obviously, this result is not valid for energy flux that depends on the cube of the water velocity, which indicates that meteorologically driven fluctuations change the average energy flux.

The numerical results analyzed in this work cannot address this influence directly since the model does not include meteorological forcing. A first guess of its size can be done assuming that $U_m(t)$ is sinusoidal of frequency σ and amplitude equal to rU_0, where *r* is the size of the amplitude of the meteorological fluctuation relative to the mean flow, which is usually less than 1 because meteorological forcing reverses the mean flow only exceptionally (García-Lafuente et al., 2002b). Thus, $U_m(t) = rU_0 \sin(\sigma t)$ and $U_{total} = U_0(1 + rsin(\sigma t))$. According to equation (5.1), the average energy flux would be proportional to $\langle U_{total}^3 \rangle = U_0^3 \langle (1 + rsin(\sigma t)^3 \rangle$. For a sinusoidal dependence, the time average between brackets, computed over a period of the fluctuation ($T=2\pi/\sigma$) is straightforwardly computed to give $(1 + 1.5r^2)$ and, therefore $\langle U_{total}^3 \rangle = (1 + 1.5r^2)$. The first term of the parenthesis in the RHS is the energy flux in absence of meteorological forcing and the second one would be the averaged increase due to a meteorological fluctuation of relative amplitude *r*. A meteorological fluctuation of amplitude $r = 0.3$ that changes the mean velocity up to 30% will carry out an increase of the energy flux of 0.135, that is, 13.5%.

The Mediterranean outflow has been monitored in ES since year 2004 (Naranjo et al., 2012), which allow us to make an approximate estimation of *r* directly from the observations there. Figure 3.10 shows that, on average, the amplitude of the subinertial fluctuations are in the range of 0.3 to 0.4 Sv (Sverdrup, 1 Sv =106 m^3s^{-1}) for a mean outflow of 1.3 Sv in absolute value, which gives a value in the range 0.25-0.31 for *r*. Therefore, the meteorologically forced subinertial fluctuations can increase the estimated averaged energy fluxes by a 10 – 15% at ES. In this location very strong currents reaching

1800 Wm^{-2} have been found, hence tidal forcing contributes to overcome the intensity by 200 – 300 Wm^{-2} but V does not change because I takes the maximum value in table 5.3.

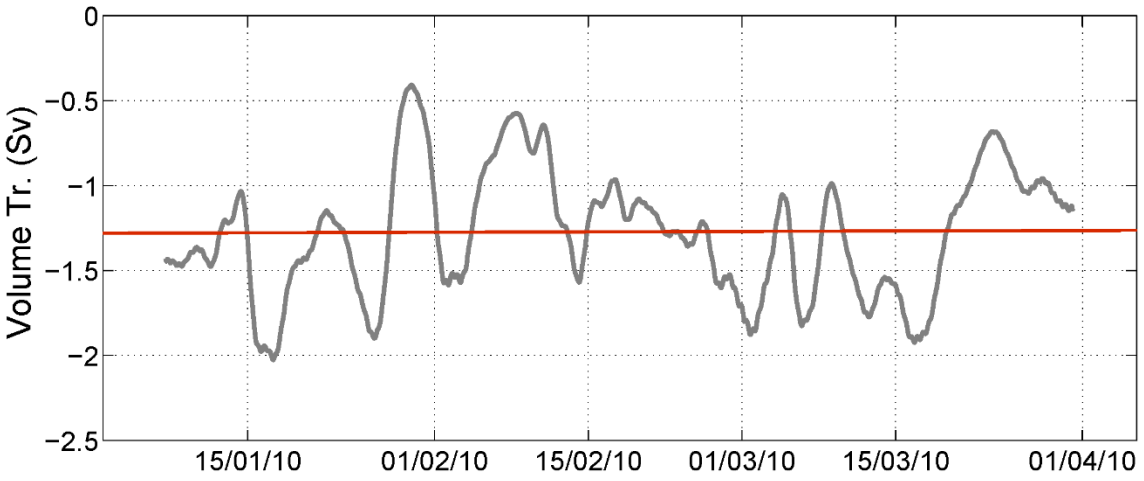

Figure 5. 10.- Mediterranean outflow estimated from observations collected by the monitoring station of ES (see asterisk in figure 5.1). The horizontal line is the mean flow, which is around -1.3 Sv.

5.6. Summary and conclusions

The non-hydrostatic version of MIT-gcm has been implemented in a high resolution grid in the Strait of Gibraltar to estimate the energy fluxes associated with marine currents in the strait of Gibraltar and to identify areas suitable for exploiting this renewable energy resource. The study shows that near-bottom layer over CS and ES areas and the surface layer (a subsurface shallow layer between 26 and 71 m indeed, for maritime safety reasons) over the CS and most of the eastern half of the strait gather good conditions from the point of view of current strength. Computed averaged fluxes in these areas can exceed 1.8 kWm^{-2}.

There are other properties of the flow, however, that must be taken into account. In most areas of the strait, the tide is strong enough to reverse flows (Sánchez Román et al., 2009; García-Lafuente et al., 2000; Sannino et al., 2002), a situation that may be unwanted specially for horizontal axis MCTs (O'Rourke et al., 2010a; Li et al., 2011), but there are other areas where these reversals do not take place or, in the worst scenario, they happen very sporadically (García-Lafuente et al., 2000; Armi y Farmer 1988). Also the strait is a paradigm of sheared flow and a well-known place of generation of high frequency internal waves (Sánchez Garrido et al., 2011), two flow properties that must be harmful for MCTs. For these reasons we have defined a set of 5 indicators that provide additional information about those flow properties that may influence the selection of a place among all places

with good conditions from the point of view of the energy flux. When these indicators are considered, the surface layer shows evident weakness regarding the flow noise (an indicator defined to account for the effect of high frequency internal waves) or the directionality of the flow, since CS area is subjected to periodical flow reversals. Flow shear affects the deeper, near-bottom layers negatively due to bottom friction, tidally driven flow reversals produce undesirable fluctuations of the flow direction, which are considered harmful for the working device, etc.

For these reasons, an attempt to quantify all the influencing factors has been made by defining a quality function that prioritizes the energy flux over the rest of indicators and combines them linearly to return a single index of suitability. This function has been contoured for the layers of interest (Figure 5.9) and allows us to conclude that the near-bottom layer (275 - 325 m depth) over ES area gathers the best conditions for installing a power plant to extract energy from marine currents. With this conclusion in mind, a short study of the meteorological influence (which was not accounted for in the model) on the estimated energy flux has been addressed by using observations collected in the very ES area. The study shows that the meteorologically-driven flow fluctuations may increase the computed energy flux in around 10-15%.

Acknowledgements

This work has been funded by the Regional Government of Junta de Andalucia (Spain) through Proyecto de Excelencia RNM-3738 (FLEGER). Partial support from CTM2010-21229-C02 of the Spanish Ministry of Economy and CTM-2008-04150E of the European MarinERA activities are also acknowledged. We are grateful to Gianmaria Sannino from the Modelling Unit of ENEA (Italy) for his assistance in the development of the numerical model used in this study.

6.- EFFECTS OF TIDAL AND RIVER DISCHARGE FORCINGS ON TIDAL PROPAGATION ALONG THE GUADIANA ESTUARY (Segunda publicación)

(Paper publicado en la revista Journal of Sea Research, en 2019, 146, 1-13. https://doi.org/10.1016/j.seares.2019.01.006.)

María Concepción Calero Quesada[1]*, Jesús García-Lafuente[1], Erwan Garel[2], Javier Delgado Cabello[1], Flávio Martins[2], Juan Moreno Navas[1].

[(1)]Physical Oceanography Group of the University of Malaga, GOFIMA, (Spain).

Campus de Teatinos s/n, C.P.:29071, Málaga, Spain.

Tlf: 952132849

[(2)]Centre for Marine and Environmental Research (CIMA), University of Algarve, Faro (Portugal).

conchi.calero@ctima.uma.es

Abstract

This paper provides information about hydrological changes in a meso-tidal estuary in which seasonal variability has been reduced by the hydraulic control exercised by a dam. The study has been carried out analyzing the outputs of a hydrodynamic model of the Guadiana Estuary, situated in the Southwest region of the Iberian Peninsula. The numerical model, in 2D barotropic mode, has been forced by tides at the ocean side and by freshwater at the upstream boundary of the domain. It has been validated using water level and velocity observations at several locations along the estuary. Different scenarios with variable tidal forcing and freshwater discharge have been analysed in order to assess the influence of each external agent on the along-channel hydrodynamics. In this way, it has been possible to reproduce states previous to the opening of the dam forcing with high freshwater discharges. The model reproduces the expected asymmetries between rising-falling tide and flood-ebb flow durations, with falling tide being longer than rising tide and ebb tide flows lasting longer than flood tide ones. These asymmetries increase with freshwater discharge, showing a trade-off between bottom friction and the freshwater inputs at the estuary's head. The asymmetry related to the tidal wave (ebb-flood) increases faster than the one of sea level (rising-falling), which agrees with the prismatic morphology of the estuary. From a discharge above 200m^3s^{-1}, friction dominates over the tidal amplification caused by the convergence of the estuary, with any tidal forcing. Three

areas have been found in which the tidal propagation has a clearly differentiated behaviour, the first of which is around the mouth of the river with strong dissipation, the second where a balance is observed between friction with the bottom and convergence and finally, the third, at the head of the estuary where the effect of the discharge of water clearly predominates.

Keywords: Guadiana Estuary; MOHID model; tidal propagation; tidal asymmetries.

6.1. Introduction

6.1.1. Theoretical framework

Knowing the hydrodynamics aspects of an estuary has special relevance for the maintenance of navigation channels, the fate of particle bound contaminants, the ecology of benthic and pelagic communities and the morphological evolution of the surrounding coastline (Garel et al., 2009a). Tidal propagation in estuaries is affected by four dominant processes (Dyer, 1997, McDowell and O'Connor, 1977; Prandle, 2009; Savenije 2005 and van Rijn, 2010): inertia related to acceleration and deceleration effects, amplification due to the decrease of width and depth (convergence) in landward direction, damping due to bottom friction and reflection at abrupt changes of the cross-section at the landward end of the estuary. These factors govern the spatial evolution of the tidal amplitude, the wave celerity and the phase lag between vertical and horizontal tides (Jay, 1991; Friedrichs and Aubrey, 1994; Lanzoni and Seminara, 1998; Prandle, 2003, 2004; Savenije and Veling, 2005). Changes in estuarine conditions cause a temporary imbalance in the hydromorphology of the estuary that will eventually converge in a new hydromorphological balance. The time needed to reach equilibrium depends on the magnitude of the actions and how far the estuary is from its equilibrium condition (Medina et al., 1998), although it is typically spoken of decades. Knowing precisely the location and extent of tidal floodplains caused by the above-mentioned hydromorphological changes can be used for planning conservatory actions in adjacent ecosystems, which are very vulnerable (Nash et al., 2014).

Along channelized estuaries, when considering entirely barotropic tides and only external forcing, tidal amplitude and phase tidal wave velocity vary due to imbalance between width convergence and bottom friction (Friedrichs, 2010). The resulting regulation of the freshwater discharge (Qr, hereafter) in estuaries by dams affects the frequency and

characteristics of floods in the river basin and the behaviour of the tidal wave evolution, i.e. changes in morphology. The effect of Qr is much smaller near the estuary mouth, but it can become dominant further upstream in the estuary, particularly during times when the river is in spate (Cai et al., 2012; Cai et al., 2013; Cai et al., 2014). By analysing some aspects of a meso-tidal estuary through the reproduction of states prior to the opening of the dam and comparing it with the current state, it is possible to verify how the estuary has evolved. In particular, it has been possible to observe changes in the distribution of flood zones or the morphology. The Guadiana Estuary (hereafter, GE), located in a semi-arid environment, is an example of rock-bound estuary with significant tidal forcing (Garel et al., 2009a) and Qr strongly regulated by a dam. This study focuses on the response of tidal propagation and asymmetries between rising-falling tide and flood-ebb flow durations along the estuary to different external forcing conditions. A hydrodynamic model in 2D barotropic mode is applied, which reproduces recent known results and provides new important information about meso-tidal estuaries under Qr strongly regulated by a dam.

One-dimensional propagation and deformation of the tidal wave in theoretical shallow estuaries was also studied by Lomonaco (1999). A study based on empirical data has been carried out in the Guadalquivir Estuary (Díez-Minguito et al., 2012). This estuary shares many features of GE; it is located in the South of the Iberian Peninsula, presents a low Qr controlled by a dam and has three distinct areas with different tide propagation processes. Therefore, the results of this study provide a direct insight into GE hydrodynamics and can be used as reference for tidally-dominated meso-tidal estuaries in semi-arid environments.

6.1.2. Study area

The GE runs through the South of the Iberian Peninsula forming the southern border between Spain and Portugal. The estuary width decreases exponentially from 800 at the mouth to 70 m at its head (Mertola, see Figure 6.1) located 80 km upstream (Fortunato et al., 2002, Garel et al., 2009a) where the tide is completely blocked at a weir (Garel 2017a; Ruíz Muñoz et al., 1996). The mean depth of the channel is about 5 m but reaches 18 m locally (Garel et al., 2009a; Garel 2017a). Historically, the wet period extends from November to January, and the dry period from July to August (Morales, 1993). Typical

Qr values are 99 to 268 m^3s^{-1} in wet period (max. 1500 m^3s^{-1}), under 30 m^3s^{-1} in dry period (Fortunato et al., 2002; Garel and D'Alimonte, 2017). The tidal regime of the GE is meso-tidal and the range varies from 1.5 m in neap to 3.5 m in spring tides (Garel and Ferreira, 2013). The main harmonic constituents are M2, S2, K1 and O1 with a higher significance of the semi-diurnal M2 component over the diurnal component K1 (Silva et al., 2000). Since the construction of the Alqueva dam (2002) located around 120 km upstream of the mouth, the Qr is strongly regulated. The result is that yearly and seasonal variability of the Qr have been markedly reduced (Dias et al., 2004; Wolanski et al., 2006). Therefore, GE has underwent important modifications and reached a man-made quasi-steady state characterised by poor productivity and low biomass in all communities (Chícharo et al., 2002; Erzini, 2005, Wolanski et al., 2006), with consequences in the food web on the coastal fishing area.

The analysis of tidal amplitude in GE presented by Morales (1993) and Silva et al., (2003) indicates a variation along the estuary of less than 0.2 m every 10 km. In detail, tidal amplitude tends to be slightly damped due to bottom friction predominance in the lower estuary (up to ~25 km), it is amplified by morphological convergence and probably reflection effects upstream (up to ~50 km), and it is dampened the most in the estuary head. (Garel et al., 2009a). This study shows similar results for the attenuation of the tidal range, especially at the mouth (the amplitude decreases by 0.25 m in live tides in the first 35 km), however, in the intermediate area it depends markedly on the discharge regime and the tidal period considered. For example, the tidal range can be constant (even amplified) in neap tides when Qr are low. Tidal wave in the GE is standing with a significant progressive component and this study it is verified that the progressive nature of the tidal wave has more influence upstream since the opening of the Alqueva dam. Data suggest that the lag between high water amplitude and peak currents is approximately 2 h throughout the entire estuary (Silva et al., 2003). Data measures at Vila Real de Santo Antonio and Odeleite show that currents are faster during low discharge ($Qr < 10$ m^3s^{-1}) compared to high discharge ($Qr > 400$ m^3s^{-1}), and also that the differences in velocities between ebb and flood peak currents are greater during high Qr (from 0.8 to 1 ms^{-1} in low Qr, and 0.2 to 0.6 ms^{-1} in high Qr).

Well-mixed conditions were observed in spring tides, while partial stratification is developed in neap tides with low Qr (<10 m^3s^{-1}) (Oliveira et al., 2006). At neap tides, the estuary is better-mixed during the flood than during the ebb. At Vila Real de Santo

Antonio, highly stratified conditions developed at neap tides for Qr >400 m^3s^{-1} but a relatively weaker stratification was observed around low water (Garel et al., 2009a). At spring tide and for Qr of up to 250 m^3s^{-1}, turbulent diffusion dominated, and the estuary was well-mixed (Ferreira et al., 2003). Despite the effective turbulent mixing throughout the water column, gravitational circulation can affect significantly the barotropic flow. With decreasing tidal range and current velocities, mixing was reduced and stratification was progressively enhanced but the estuary tended to be better-mixed toward the head. Therefore, there is an alternating establishment and breakdown of two-layer residual flow with spring and neap tides (Garel et al., 2009a).

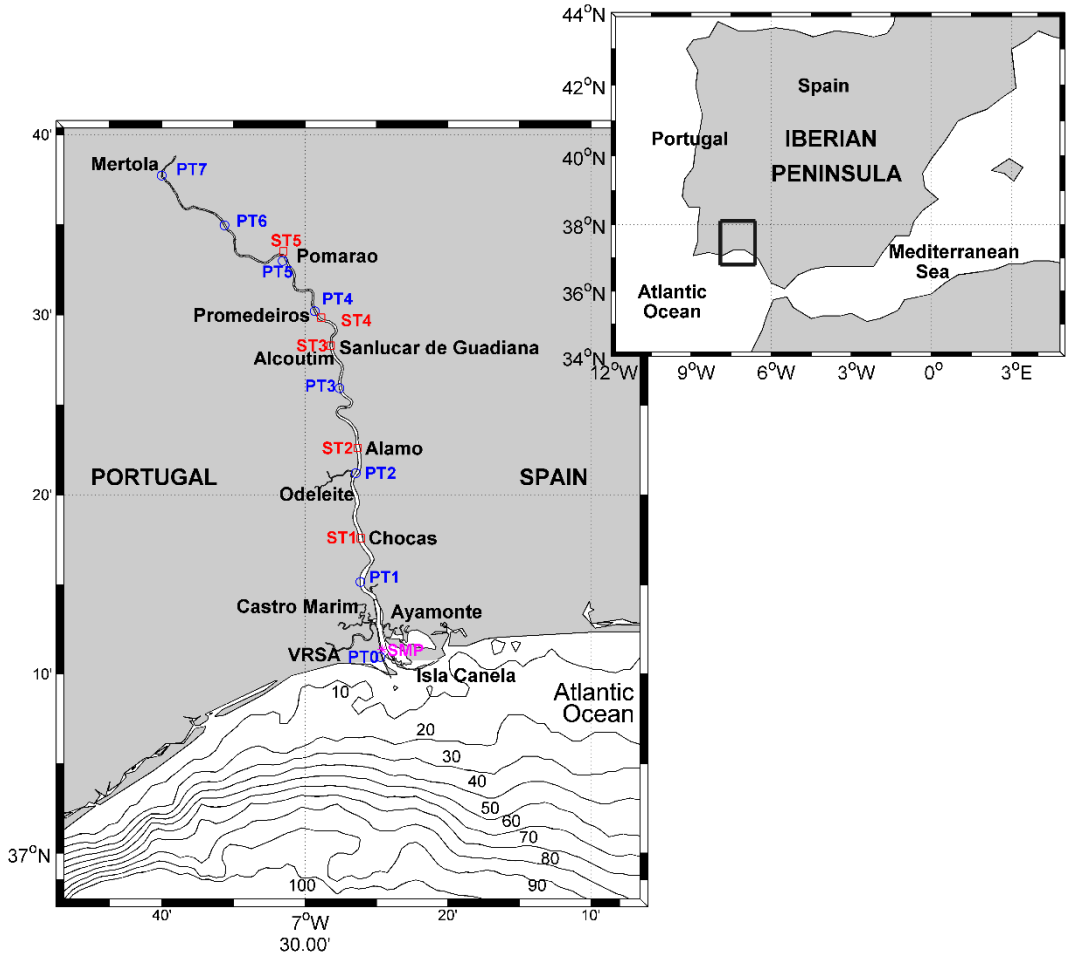

Figure 6. 1.- Map of the GE and its location within the Iberian Peninsula (see inset). Some localities of Spain and Portugal are indicated in bold black (VRSA stands for Vila Real de Santo Antonio). Circle symbols and acronym PT in blue indicate the location of 8 pressure transducers. Square symbols and acronym ST in red are 5 velocity- recording stations. The asterisk and acronym SMP indicate the location of the SIMPATICO monitoring system.

6.1.3. Previous modelling works in the GE

Numerical simulations of the GE can be traced back to the beginning of the century. Different approaches were implemented to simulate the Qr and tidal currents in the estuary. Fortunato et al. (2002) applied the 2D ADvance CIRCulation (ADCIRC) numerical model of Luettich et al. (1991) on a domain about 80 km upstream (Mertola, see figure 6.1 for location) using a finite element triangularization (Fortunato and Oliveira, 2000). This work was continued by Pinto et al. (2003), Pinto (2004), and Oliveira et al. (2006), who applied the more elaborated Eulerian-Lagrangian CIRCulation (ELCIRC) 3D, baroclinic model of Zhang et al. (2004). Wolanski et al. (2006) developed a 70 km long 1D ecohydrological model that integrates physical, chemical and biological processes in order to predict the ecosystem health. In this paper it is highlighted the importance of the man-made regulation of the Alqueva dam for the ecosystem. Lopes et al., (2003), Lopes (2004) and Martins et al., (2004) used the hydrodynamic system MOHID (MOdelo HIDrodinamico) in 2D and in 3D baroclinic mode with a cartesian grid and a domain of 40 km. Basos (2013) developed a high resolution curvilinear bathymetry as an input in the MOHID hydrodynamic system in 2D. A very recent one-dimensional study has been conducted for the GE by Garel and Cai (2018).

The above mentioned works are rather complete, with descriptions in 2D and 3D, but the validation was generally done with data prior to the opening of the Alqueva dam. Also, in most of the above-referred studies, the stations available for validation were located in the lower part of the estuary with rather short datasets. In the present study, longer dataset distributed along the estuary has become available. This availability has motivated the new simulation of the GE in the present work, using the hydrodynamic model MOHID. The data is appropriate for the two-dimensional barotropic model of this work, which is more precise than one-dimensional models as it accounts better for cross-section friction and convergence, suitable for a study on flooding areas. A three-dimensional model cannot currently be applied, has a higher computational cost and is out of the scope of this work.

Present work employs high resolution curvilinear bathymetry of Basos (2013), made of boundary-fitted curvilinear grids, which fit the coastline precisely, has few unused grid cells and higher precision in the more interesting narrower parts of the domain. The grid cells have different size and shape but the grid still can be nearly-orthogonal. This type

of grid is particularly well suited for long and narrow meandering rivers like Guadiana and for all coastal systems in general (Blumberg et al., 2000).

6.2. Materials and methods

6.2.1. Model and bathymetry

6.2.1.1 MOHID system

The hydrodynamic system MOHID is an open-source modular system that comprises numerical models, graphical interfaces and other pre- and post-processing tools (Braunschweig et al., 2004; Miranda et al., 2000; MOHID, 2002). The code is written in Fortran using an object-oriented programming strategy. The MOHID package includes GIS module which handles spatial and temporal variable data in specific formats required or produced by MOHID, MOHID GIS (Braunschweig et al., 2005).

MOHID Water is a 3D hydrodynamic model developed to simulate surface water bodies using Finite Volume method in the real domain without any spatial transformation. Following Martins et al. (2001), the Cartesian coordinate framework equations are as follows:

$$\frac{\partial u_1}{\partial x_1} + \frac{\partial u_2}{\partial x_2} + \frac{\partial u_3}{\partial x_3} = 0 \quad (6.1)$$

$$\frac{\partial u_1}{\partial t} + \frac{\partial (u_j u_1)}{\partial x_j} = f u_2 - g \frac{\rho_\eta}{\rho_0} \frac{\partial \eta}{\partial x_1} - \frac{1}{\rho_0} \frac{\partial p_S}{\partial x_1} - \frac{g}{\rho_0} \int_z^\eta \frac{\partial \rho'}{\partial x_1} dx_3 + \frac{\partial}{\partial x_j} (A_j \frac{\partial u_1}{\partial x_j}) \quad (6.2)$$

$$\frac{\partial u_2}{\partial t} + \frac{\partial (u_j u_2)}{\partial x_j} = -f u_1 - g \frac{\rho_\eta}{\rho_0} \frac{\partial \eta}{\partial x_2} - \frac{1}{\rho_0} \frac{\partial p_S}{\partial x_2} - \frac{g}{\rho_0} \int_z^\eta \frac{\partial \rho'}{\partial x_2} dx_3 + \frac{\partial}{\partial x_j} (A_j \frac{\partial u_2}{\partial x_j}) \quad (6.3)$$

$$\frac{\partial p}{\partial x_3} = -\rho g \quad (6.4)$$

Equation (6.1) is continuity for incompressible fluids, (6.2) and (6.3) are the Navier-Stockes equations for horizontal velocities and (6.4) is the hydrostatic equation. In them, (x_i) are the Cartesian coordinates (longitudinal, transversal and vertical, for x_1, x_2 and x_3, respectively), (u_i) are the velocity components in the coordinates x_i, η is the free surface, A_i, the turbulent viscosity coefficients, f, the Coriolis parameter, p_s, the atmospheric pressure, g, the acceleration of gravity, ρ_0 the local density, ρ a mean density, ρ' is the density anomaly referred to the depth-averaged density and ρ_η is the density on the

surface. Density has been calculated from the salinity and temperature through the seawater equation of state (Leendertsse and Liu, 1978).

MOHID Water has been applied to several coastal and estuarine areas and it has showed its ability to simulate complex features of the flows. Different environments have been studied along the Portuguese coast, including the main estuaries (Minho, Lima, Douro, Mondego, Tagus, Sado, Mira and Arade) and coastal lagoons (Ria de Aveiro and Ria Formosa). The model also has been applied in most Galician Rías and some European estuaries - Western Scheldt, The Netherlands, Gironde, France, and Carlingford, Ireland, etc., (www.mohid.com). In this paper, MOHID Water is used to simulate the GE in 2D barotropic mode. Barotropic tide gives the solution of the first order wave equation of shallow, funnel-shaped estuaries (Friedrichs, 2010) like the GE, which allows us to study rising-falling and flood-ebb flow asymmetries as well as relative phase between water level and tidal velocity. Moreover, using MOHID GIS has the advantage to allow manual change of values of particular grid cells, which is not possible in many other GIS programs.

Estuary bathymetry (see subsection 6.2.1.2) is used as the model root domain. Qr values from in-situ measurements (see subsection 6.2.2) are specified for several cells as input for the closed boundary conditions. Sea level oscillations simulate tidal forcing as input for the open boundary conditions (located at the continental shelf). The harmonic constants to reconstruct the barotropic tidal signal on the shelf have been obtained from the global Finite Element Solution tidal model (FES2004, Lyard et al., 2006), a tool included in Mohid-Studio. The most important ones are listed in Table A1 in the Annex. Although MOHID Water can deal with atmospheric (wind-stress, pressure) and radiative (solar heating, evaporation, etc.) forcing, they have not been included for idealization of the study.

6.2.1.2. Bathymetry

The model uses the bathymetry implemented by Basos, (2013) (http://www.hidrografico.pt/download-gratuito.php). It is a high resolution curvilinear bathymetry that comprises 300 m of the continental shelf and extends to 80 km inland, near Mertola (see figure 6.1). Some particular cell values in the upper estuary were realistically manipulated using MOHID GIS during the model calibration step in order to

improve the agreement with observations (see subsection 6.2.3.1). The final bathymetry of the domain is presented in figure 6.2.

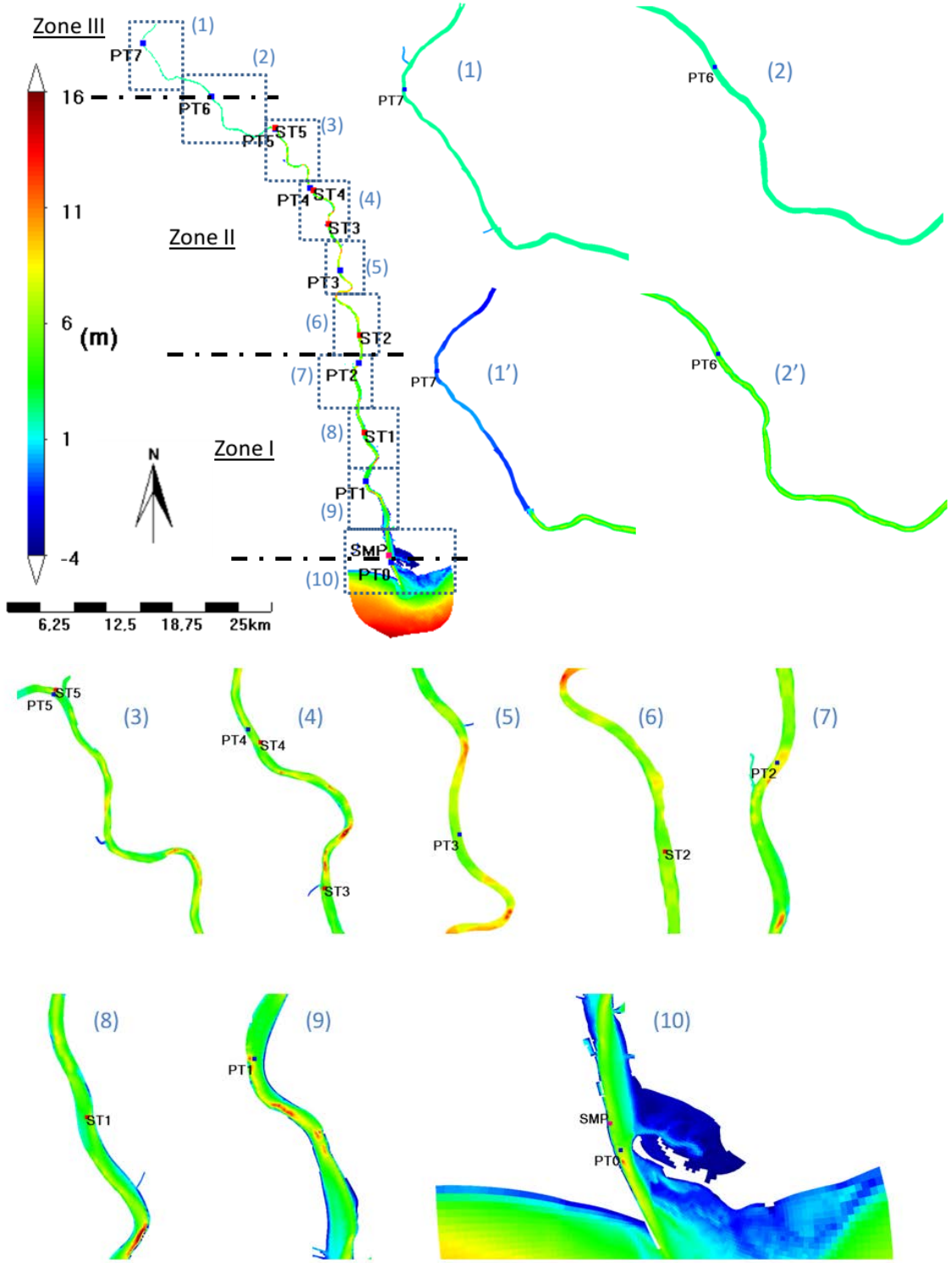

Figure 6. 2.- Bathymetry of the model domain (colour scale on the left). The 0 m contour corresponds to the hydrographic zero so that positive values (colours from cyan to red) are depths below zero and negative values (deep blue) are above zero. The estuary has been splitted into pieces in order to make visible bathymetric details. The sectors (1') and (2') are the manually modified sectors (1) and (2). The different locations of pressure transducers (PT) and velocity stations (ST) are indicated (see Table 6.A1 for further details on these stations). The initial point, i.e. 0 km, is situated at PT0 at the estuary mouth (see figure 6.2, box 10) and the last point is at PT7, 70 km at the estuary head (see figure 6.2, box 1).

6.2.2. In-situ measurements

Different surface water level and current velocity observations are available for calibration/validation purposes, with dataset both previous and later than the Alqueva dam construction (see Table 6.A2). Current-meters profilers (AANDERAA RCM9 MkII) were deployed near the deepest part of the channel, measuring velocity 0.5 m above the riverbed. Additionally to the data summarized in Table 6.A2, observations from a long-term environmental monitoring station (the Integrated System for Monitoring Parameters Type in COastal areas -SIMPATICO, SMP hereafter; see figure 6.1 for location) near the mouth are also available (Garel et.al 2009b, Garel and Ferreira, 2011a, Garel and Ferreira 2015, Garel, 2017b). This autonomous recording system has a bottom-mounted acoustic current-meter profiler (Sontek Argonaut XR, 750 kHz) and operated from March 2008 to April 2014. While the current-meters measure the current value at a single point in the water column, the SMP monitoring system directly provides the flow velocity at ten equally spaced points of the vertical profile. This device also provides a value integrated in the vertical and is used in the comparison with the value provided by the barotropic model.

The Qr (m^3s^{-1}) data from March 2008 to April 2014 were measured at two hydrographic stations. These data are freely available at the Instituto de Agua de Portugal (INAG, currently the Portuguese Environment Agency, http://snirh.pt). The two stations, Pulo do Lobo (managed by INAG/APA) and Pedrogão (managed by EDP-Portugal Electricidad) are located about 20 and 50 km from the head of the estuary respectively, and account both for 90% of the Guadiana Qr (Garel and Ferreira, 2015). Compared to the main Qr of the Guadiana river, the tributary discharge is negligible (Fortunato et al., 2002, Garel and D'Alimonte, 2017) and has not been considered in this study.

6.2.3 Calibration and Validation

6.2.3.1. Calibration

Even though some datasets are previous to the Alqueva dam construction (see table 6.A2), they are well suited for calibration, as the dam does not modify inherent estuarine physical constituents, like friction and viscosity, and any changes in estuarine conditions will take decades to be noticeable. A data subset was extracted from the available observational data so calibration and validation processes are not performed on the same data (cross

validation). The bottom friction coefficient and the viscosity parameters were adjusted to match the observed tidal propagation and deformation. The adjustment was carried out by analysing the amplitude and phase of surface level of the different harmonics, especially of M2 (Figure 6.3). The final adopted values for the friction coefficient, viscosity and other parameters such as grid size and time step are shown in Table 6.A3.

Judging from the amplitude pattern of M2 deduced from observations (red dots in figure 6.4a), the estuary is damped in the lower part and amplified from 30 km upstream, with a relative maximum at around 60 km probably due to reflection caused by the presence of a sill as suggested in Garel et al. (2009a) and Garel (2017a). This sill actually can be found at km 66. From 60 km to the upstream end of the domain, the observations display a noticeable damping due to friction. The observed tide at PT7 shows oscillations truncated near the low tide due to the presence of the sill (see figure 6.3c). Initial simulations did not match observations in the upper part of the estuary, probably due to the lack of data in this section. Two main changes were manually introduced in the bathymetry of the upper part. Cross-section shape was modified from rectangular-like to a more natural v-shaped. Also, a sill was set at 66 km from the mouth (hereafter, sill66). After these modifications, the model reproduced these features better, although the tide amplification around the sill still remained slightly underestimated (Figure 6.3c and 6.4a).

6.2.3.2. Validation

Validation was carried out by comparing the model output data with the available in-situ measurements, both sea level and currents. The surface level oscillations were quite well reproduced by the model (Figure 6.3) and the harmonic analysis confirms the result. Figure 6.4 shows the comparison for the most representative constituents of each species, M2 and S2 for semi-diurnal, K1 for diurnal and M4 for the main non-linear constituent. M4 is of particular interest because it is the result of friction in the estuary, since its amplitude was set to 0 m in the model boundary conditions at the mouth (Table 6.A1). The good agreement of this constituent with the observations gives support to the model configuration. Table 6.1 shows the very high correlation between model outputs and observations and the low root mean square error (RMSE) between both datasets, thus confirming the good performance of the model regarding surface oscillations.

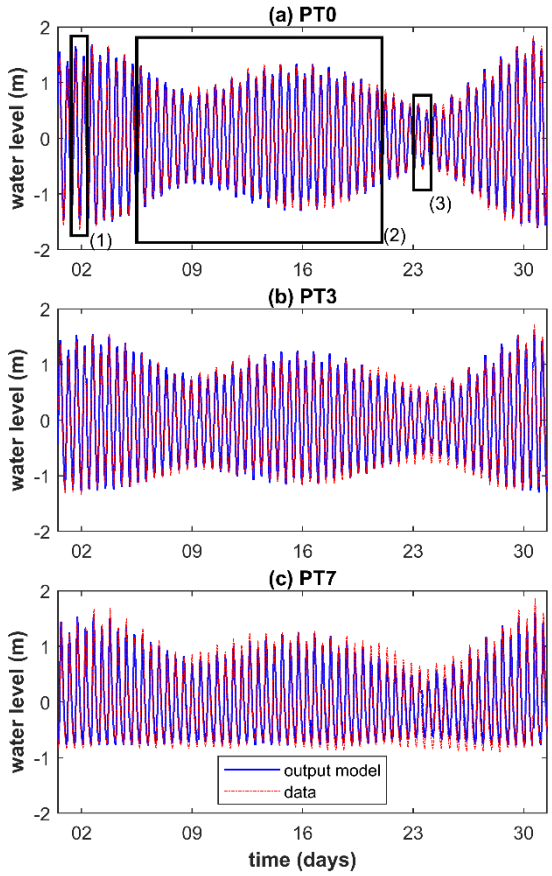

Figure 6. 3.- Tidal signal at some selected sites of the GE. Blue and red lines correspond to model outputs and observations, respectively. Rectangles in the top panel indicate the spring (1), fortnightly cycle (2), and neap (3) periods that have been used to specify strong, average and weak tidal forcing, respectively.

Table 6. 1.- Correlation coefficients (CorrCoef) and Root Mean Square Error (RMSE) of the tidal signal on the PTs.

Tidal gauge	Corr Coef (%)	RMSE (cm)
PT0	99.58	7.41
PT1	99.14	10.32
PT2	99.35	8.53
PT3	99.14	9.40
PT4	98.98	10.28
PT5	99.07	10.28
PT6	99.08	11.43
PT7	97.52	15.50

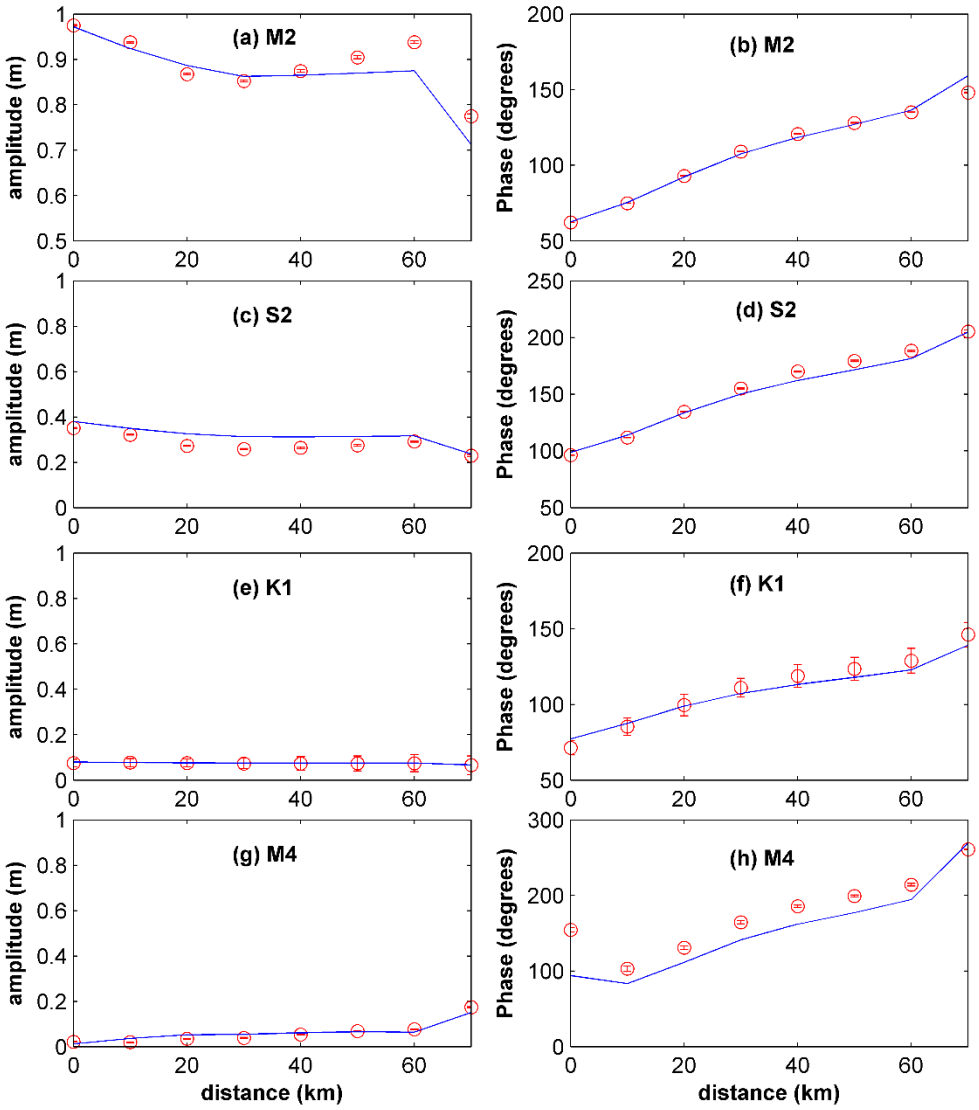

Figure 6. 4.- Amplitudes (column of the left) and phases (column of the right) of the harmonic constants along the estuary for some selected constituents. The simulation period is August 2015. Blue solid lines represent the model output and red circles (with its error bars) are the harmonic constants of water level observations, respectively.

Tidal velocity was validated by comparing observed and modelled velocities at the five current-meter sites (STs). Since no Qr data was available at these sites in the studied period, a value of 50 m^3s^{-1} has been estimated for them, which is the most probable value from the dam in a wet period (Fortunato et al, 2002, Wolanski, 2006). Notice that only one out of five records (ST4) was later to the Alqueva dam construction and, therefore, it is the only representative of the present conditions. The lack of velocity data made us to include both dataset for comparison with the model outputs, assuming that the phases of the currents have not changed too much after Alqueva dam construction.

Concerning to the recorded RCM9s velocities at the three sites presented in Figure 6.5, they show non-matching results in the amplitude. Velocity amplitude at ST1 is considerably smaller than at ST2 and ST4, indicating that this cannot be reproduced by the modelled barotropic tide given that the river-cross is similar at the three stations and there are no more physical variables within the model that could explain such discrepancy. The model, on the contrary, provides comparable velocity amplitude at the three sites, which is the expected result in a channelized estuary. We speculate with the fact that the magnitude of the observed amplitude depends on the exact location of the RCM9s over the river bed, thus being very sensitive to the exact deployment position. On the other hand, the current-meter measures the velocity at a single level near the riverbed, which is influenced by bottom friction, whereas the model provides a depth-averaged velocity. For this reason the velocity amplitude deduced from observations does not seem a suitable variable for validation purposes. Conversely, the phase is more suitable for this purpose since it relates to the moment of the velocity peak, which is expected to be rather constant in a given cross-section. It does show a coherent behaviour along the estuary (Figure 6.5a, b and c). Therefore, the validation of the model velocity only has considered the phases of the ST observations in which case the agreement is good (Figure 6.5d).

The validation is completed by comparing the model output with the vertically-averaged velocity measured by SMP station (Garel et al., 2009b) (Figure 6.5d, e). Since this site has long time series of observations after the construction of the Alqueva dam and Qr is available throughout these series, wet and dry periods have been simulated to be compared with the observations using the corresponding discharges Qr. The simulated velocities have been rotated in the direction of the channel axis, the along-river component has been selected and submitted to harmonic analysis. Since the model lacks meteorological forcing, graphical comparison does not match, so tidal wave characteristics are compared in Table 6.2. The agreement of amplitudes and phases is satisfactory for the semidiurnal constituents and also for K1, despite its low amplitude. Amplitudes of M4 agree too, but phases do not. The discrepancy may be due to the fact that SMP is too close to the boundary where the prescribed amplitude of M4 is null by the FES2004 model.

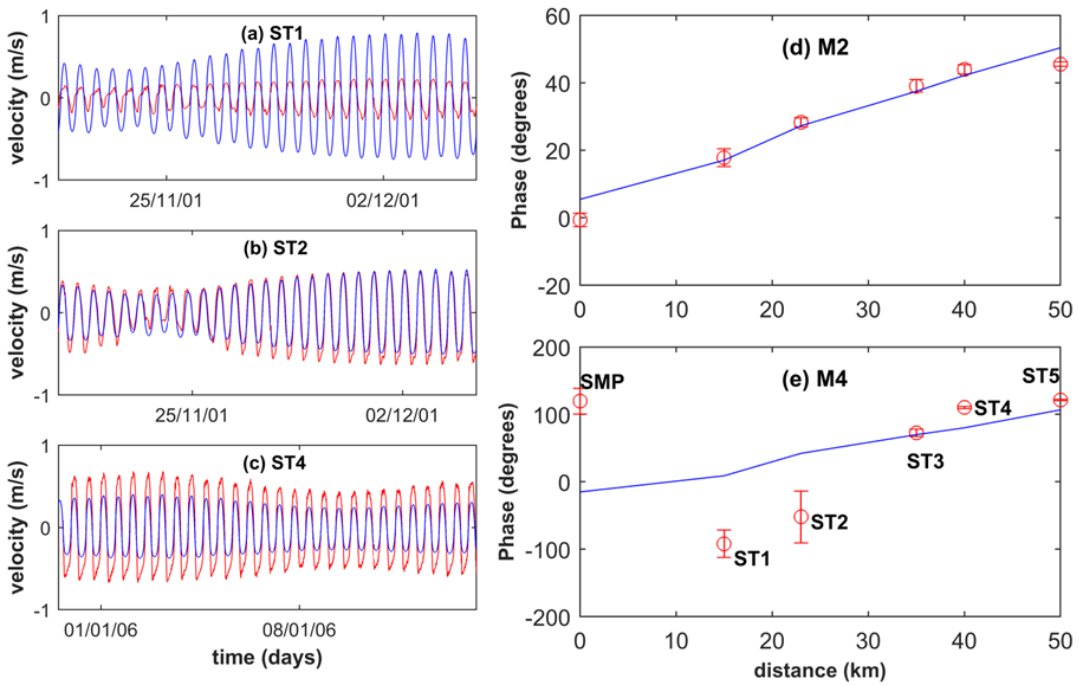

Figure 6. 5.- Panels a, b and c: Along-river component of the vertically-averaged velocity at stations ST1, ST2 and ST4 produced by the model (blue lines) and the in situ observed velocity at 0.5 m above the riverbed (red line).Panels d and e: Phases of the along-river component of the velocity throughout the estuary produced by the model (blue line) and of the observations at the different stations (red circles with error bars).

Table 6. 2.- Harmonic analysis of the depth-averaged along-river component of the velocity measured by SMP station upper line (normal case) and produced by the model lower line in (italic case).

	WET PERIOD		DRY PERIOD	
Constant	Amplitude (ms^{-1})	Phase (degrees)	Amplitude (ms^{-1})	Phase (degrees)
M2	0.76 ± 0.02	-1 ± 2	0.78 ± 0.03	-4 ± 2
	0.61 ± 3·10^{-4}	*5 ± 0.03*	*0.61 ± 3·10^{-4}*	*5 ± 0.03*
S2	0.23 ± 0.02	16 ± 6	0.32 ± 0.03	39 ± 6
	0.17 ± 3·10^{-4}	*26 ± 0.1*	*0.24 ± 2·10^{-4}*	*45 ± 0.1*
K1	0.04 ± 0.003	317 ± 4	0.05 ± 0.004	355 ± 5
	0.02 ± 9·10^{-4}	*347 ± 3*	*0.03 ± 0.002*	*341 ± 4*
M4	0.02 ± 0.006	120 ± 19	0.03 ± 0.004	151 ± 8
	0.03 ± 1·10^{-4}	*345 ± 0.3*	*0.02 ± 1·10^{-4}*	*349 ± 0.3*

6.3. Discussion and results

The spatial response of the estuary to the tidal propagation along the estuary is affected by the prescribed boundary conditions at the estuary mouth and the Qr at the estuary head. The response is addressed below by analysing the model results for different tidal and Qr forcing.

In order to study the influence of the changing tidal conditions on the tidal wave propagation along the estuary, three different situations corresponding to strong, mean, and weak tidal forcing have been defined (see rectangles in Figure 6.3a). They have been denoted by spring tide (rectangle #1), average tide (rectangle #2), and neap tide (rectangle #3), respectively. A harmonic analysis of these series was performed using the standard r_t_tide matlab function (Leffer and Jay, 2009; Pawlowicz et al., 2002). Despite the spring and neap tide conditions being much shorter than the average tide, a realistic tidal forcing was taken to know maximum and minimum amplitude in a complete fortnightly cycle. The most relevant value from the harmonic analysis are the Semi-diurnal Tidal Amplitude (hereafter, STA) given by M2 output, that is used as a description for the tidal propagation wave amplitude. Non-linear constituents or over-tides arise from quadratic bottom friction. Their change of amplitude from one point to another causes the deformation of the tidal oscillation, the greater the over-tides, the greater the deformation. Among them, M4 constituent is the most important one. Thus, the spatial slope of M4 gives information on friction, not the amplitude itself. The spatial variation of the Quarti-diurnal Tidal Amplitude (hereafter QTA) given by M4, is used as an approximate description of friction. These outputs are not actual M2 and M4 constituents when considering spring and neap tides since other constituents, such as S2, cannot be discriminated in STA. An interval of three tidal cycles has been taken as it is the shortest time interval where QTA can be discriminated so for spring and neap tide cases a tide cycle has been added (to those marked on the rectangles #1 and #3). Figure 6 presents the spatial evolution of STA and QTA along the estuary.

Seven different Qr (5, 10, 50, 100, 200, 300 and 500 m^3s^{-1}) within historical values have been selected as boundary conditions in the estuary head. Along with the three chosen tidal forcing, they give a total of 21 different scenarios (see Figure 6.6) which are discussed next.

6.3.1. Tidal propagation under change in boundary forcing.

Upon QTA behaviour, three distinct zones can be defined. Zone I, ranging from PT0 to PT2 (up to 20 km), is characterized by a rather steep increase of QTA amplitude. In zone II, ranging from PT2 to PT6 (from 20 to 60 km), QTA amplitude growth is smoothed. In zone III, upstream of PT6 (60 km and above), QTA is strongly dependent on Qr and the presence of sill66, which is situated in this zone. All these zones are indicated in Figure 6.6.

In zone I and in spring tides, the tidal range is linearly attenuated by ~0.25 m (~$1.25\ 10^{-2}$ m km^{-1}, Figure 6.6a) while in the average tide it is reduced to ~0.10 m (~$0.5\ 10^{-2}$ m km^{-1}, Figure 6.6b). In both cases the amplitude reduction is rather independent of the Qr. In neap tides the behaviour is a bit different; a detailed inspection shows that the slope of the amplitude changes sign: for Qr ≤ 100 m^3s^{-1} (or low regime), the tidal wave height increases slightly (positive slope) while for Qr > 100m^3s^{-1} (or high regime) the amplitude remains constant or, even, decreases slightly (Figure 6.6c). Regarding QTA, in spring tides its amplitude experiences a significant increase in this zone (Figure 6.6d). As QTA slope is an approximation of friction, it indicates that friction is relevant in this zone. Contrary to what happens with the tidal amplitude, the slope shows dependence on Qr, being steeper the higher the Qr. Under average tide, the spatial behaviour of QTA is noticeably reduced but still maintains a similar dependence on Qr (Figure 6.6e). Neap tides keep on exhibiting reduction and, again, the same dependence on Qr (Figure 6.6f). The diminution of QTA amplitude and the slope of the tidal forcing are expected results, as friction effects are increased with higher Qr (Savenije, 2005). Our model suggests that in zone I and under spring and average tide conditions, bottom friction predominates over morphological convergence, (Figures 6.6a,b) while at neap tides, frictional and convergence effects are nearly in balance.

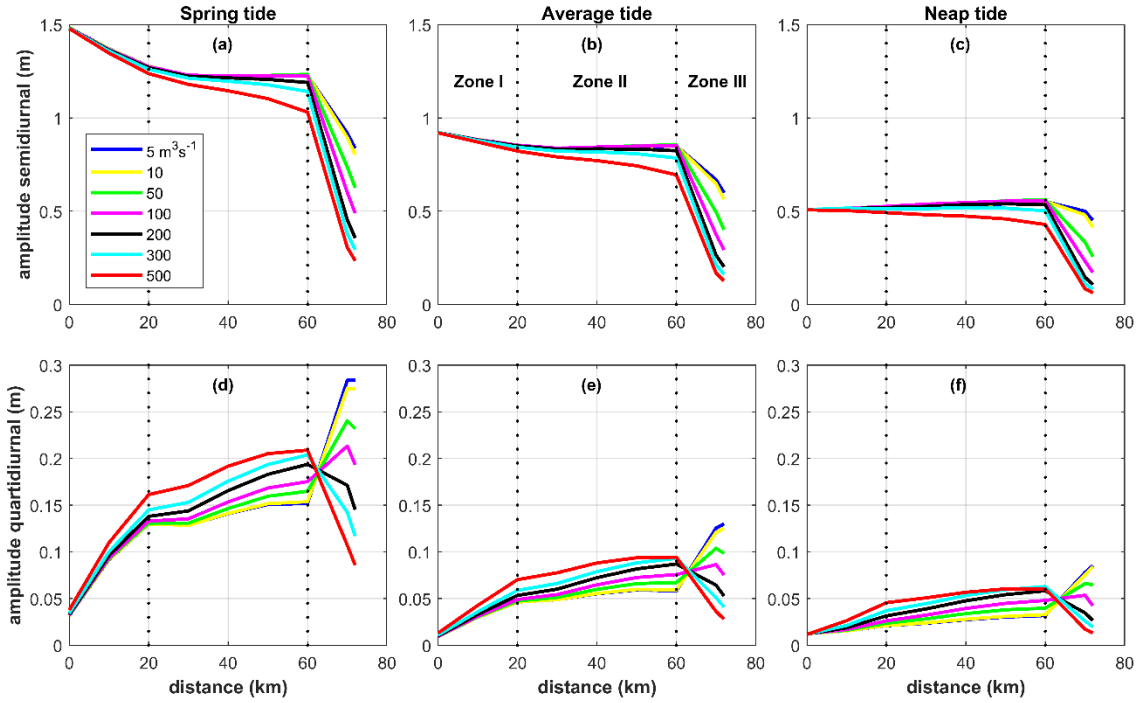

Figure 6. 6.- Top panels: Semi-diurnal amplitude along the estuary under different tidal forcing and freshwater discharges (Qr in m^3s^{-1}, see legend). Vertical dotted lines delimit the zones discussed in the text. Bottom panels: Same as top panels for quarti-diurnal constituent.

In spring tides and in the first 10 km of zone II, the tidal range follows the same pattern as in zone I (Figure 6.6a). Upstream of this distance, the pattern depends on Qr. In low regime ($Qr< 100m^3s^{-1}$) the tidal range is rather constant (around 1.2 m), implying balance between friction and convergence. Under high regime ($Qr>100m^3s^{-1}$), the amplitude goes on diminishing as it did in zone I, although at a lower rate (0.2 to 0.4 10^{-2}m km^{-1}), suggesting friction prevalence. The pattern under average tide mimics spring tides with diminished amplitudes (Figure 6b). In neap tides the amplitude tends to increase slightly for all Qr except fort the largest value of 500 m^3s^{-1} (Figure 6.6c, red line). This would indicate that convergence prevails or, at least, balances friction all over the zone except for unusually high Qr. Quarti-diurnal amplitude in zone II keeps on increasing at a reduced pace (Figures 6.6e), which would mean less friction in agreement with the convergence-friction balance mentioned above. All in all, in high regime, friction prevails over other amplification effects regardless of tidal forcing, while in low regime it is balanced by convergence (spring tide and average tide) or even overcome (neap tide).

In zone III, the tidal range is intensely attenuated (especially after the sill66 mentioned in 6.2.3.1 section) under any tidal forcing (Figure 6.6a, b and c), either by friction or by the

Qr. Still, during spring tides, tidal wave reaches amplitude of 0.8 m at the end of this zone under low Qr, although the presence of a weir at 80 km prevents further progression. For large Qr, however, the wave amplitude diminishes sharply, suggesting that Qr effect is greater than the friction effect on the wave attenuation. Accordingly, QTA behaves differently depending on Qr. For low Qr, QTA amplitude grows quickly, causing a strong deformation on the tidal wave, until it is truncated at sill66 due to low water level (Figure 6.3c). For large Qr, tidal progression is seriously hampered, consequently diminishing all constituents which is the reason for the counter-intuitive sharp diminution of QTA, particularly illustrated by the red lines corresponding to Qr = 500 m^3s^{-1} (Figure 6.6d, e and f). It is important to remark that the negative slope of QTA is not caused by friction, which is still large presumably, but by the strong damping of the tidal signal caused by Qr. Under these extreme circumstances, QTA slope is not an approximation of friction any longer.

6.3.2. Rising-falling tide duration

Figures 6.7a and 6.7b show the duration of the falling tide for spring and neap tides, respectively. Since tidal period is ~12.42 h, any duration different from 6.21 h implies asymmetry of the rising-falling tide. According to figure 6.7, the falling tide is longer everywhere for any tidal strength and Qr, even at the estuary mouth where the duration is ~6.5 h. The duration of the falling tide at any point during spring tide is greater than during neap tide.

In zone I, falling tide duration increases rather linearly with distance from the estuary mouth, depending mostly on tidal forcing and slightly on Qr: the greater the tidal forcing and Qr, the longer the duration. In zone II, falling tide still increases with distance with steeper increases the greater the Qr, and little variation with the tidal forcing. An exception is found between PT5 and PT6, where it decreases slightly during neap tides and for Qr< 200 m^3s^{-1}. In zone III, it rises again strongly, where it only depends on Qr, but contrary to the previous zones, the duration of the falling tide is longer for the lower Qr. This last increase is more noticeable during the neap tide (Figure 6.7b) and also for the lower Qr.

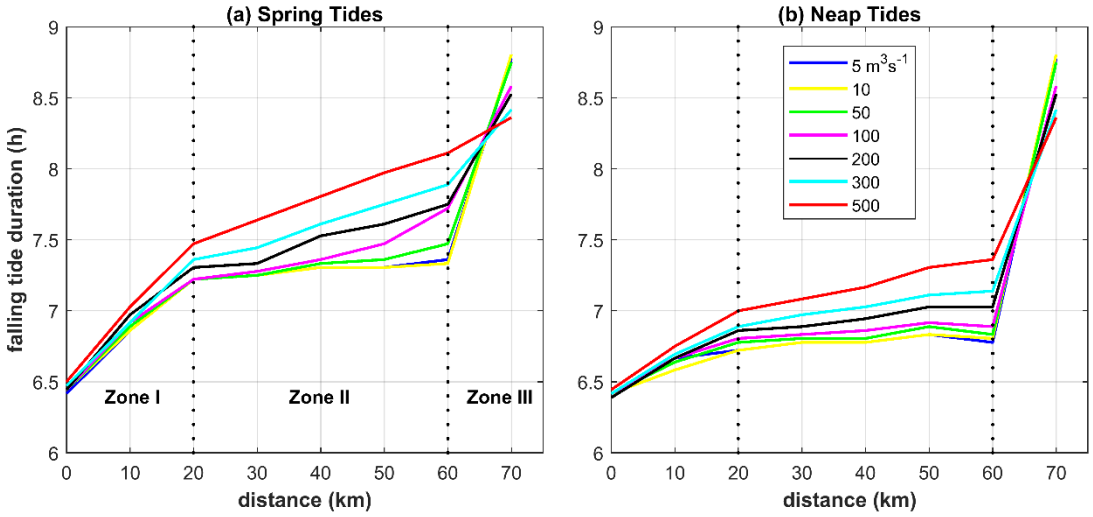

Figure 6. 7.- a) Duration of the falling tide in spring tide along the estuary for different Qr (see legend). b) Same as a) in neap tide. The duration of the rising tide is the difference between tidal period and the duration of the falling tide.

According to Savenije (2005), estuary friction delays tidal progression, so as expected the slope of the falling tide duration recalls the QTA slope, except for zone III with high Qr, where QTA signal was too damped. Therefore, the same discussion on estuary friction applies here: In zone I bottom friction is predominant, depending on tidal forcing and slightly on Qr; in zone II morphological convergence is balanced with friction (a characteristic of funneled estuaries) for low Qr, but friction is increased at higher Qr; in zone III friction is clearly dominated by Qr. Morphological convergence accelerates tidal progression in zone II, explaining the constant falling tide duration for low Qr (under 50 m^3s^{-1} for spring tides and 100 m^3s^{-1} for neap tides). Bottom friction increases with the basin cross-section, explaining the delay of the falling tide in zone II due to increases in the flooding area, which depends on the Qr and the tidal forcing. For example, around PT5 and for Qr = 100 m^3s^{-1}, falling tide duration is suddenly different during spring tides compared to neap tides. In the first case the bottom friction increases suggesting that water level arises occupying a larger flooding area (Figure 6.7a). Looking at PT5 during neap tides (Figure 6.7b), there is also a sudden increase when Qr goes from 100 to 200 m^3s^{-1}, confirming that the water level is flooding a bigger area in this case. Similarly, another sudden increase can be found at PT4 for Qr = 200 m^3s^{-1} during spring tides. For Qr =300 and 500 m^3s^{-1} in spring tides the thickness of the water sheet in zone III increases, the estuary basin is filled, the bottom friction effect is less notorious and river conditions are similar in zones II and III. Therefore, sill66 has no effect on tidal duration in zone III for

high Qr because water level is high enough to top the sill. Curiously and regardless of Qr, the same duration is achieved at the far end of the domain in zone III for spring and neap tides (compare Figures 6.7a and b), due to the predominance of Qr at the head of the estuary and with the lower Qr the less thickness of the water column and bottom friction causes the delay.

6.3.3. Ebb-flood flow duration

The model also predicts asymmetry of the ebb and flood phase duration. The ebb duration is longer and stream velocity is faster as Qr increases in every case, as shown in Figure 6.8, where flood and ebb currents have been drawn with thick and thin lines, respectively. Ebb-flood currents should behave as a pure sinusoidal wave at PT0. A strong deformation of the tidal wave is shown from PT3 to PT6, mostly due to friction (Figure 6.8, difference between panel a and panel b). At very low Qr, there is no apparent difference between ebb and flood duration as the wave progresses inland, while at higher Qr, flood duration is reduced. The greater is Qr, the flood currents become blocked in the upper estuary (for Qr = 500 m^3s^{-1} in figure 6.8b).

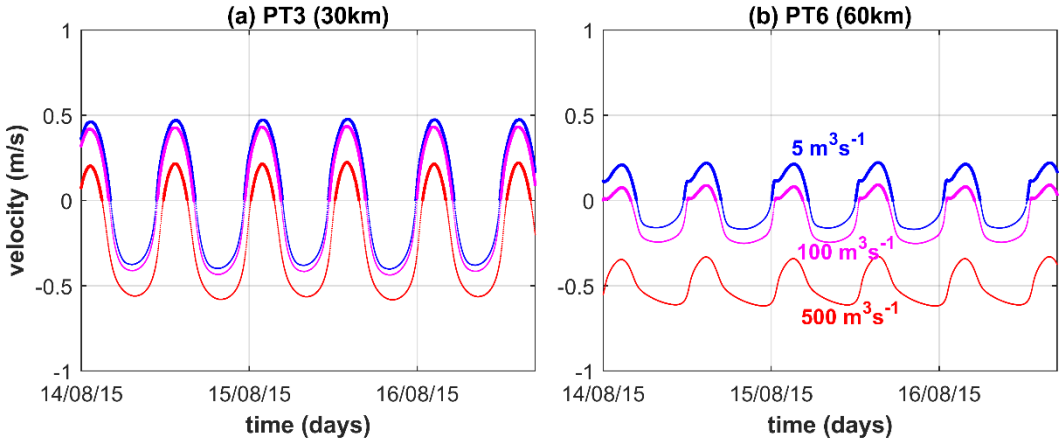

Figure 6. 8.- a) Modelled tidal currents at 30 km of distance from PT0 for three different Qr (blue 5, pink 100 and red 500 m^3s^{-1}). Thick and thin lines indicate flood and ebb currents, respectively. b) Idem for modelled currents at 60 km of distance from PT0 for the same three different Qr.

6.3.3.1- Strong tidal forcing: spring tides

Figure 6.9a addresses the variation of flood-ebb asymmetry in spring tides. It represents the difference in duration between flood and the ebb phases (DDF-E), which is always negative as the first is always shorter than the last one. The point of maximum difference

in duration between flood and ebb phase is defined as the as the point of no current reversal (hereafter, NCR) (marked by empty black circles in figure 6.9). Therefore, the DDF-E duration ranges from approximately 1h for low Qr at PT0 in the mouth (comparable durations of ebb and flood cycles) to -12.42h in those situations when NCR is met somewhere in the estuary.

For very low Qr ($\leq 10 m^3 s^{-1}$), DDF-E in zones I and II changes from ~-1.5h at PT0 to -2h at the end of zone II (Figure 9a). Upstream of this point, it increases rapidly although NCR is never reached. For moderate Qr ($10<Qr<100 m^3 s^{-1}$, approximately) the spatial variation of DDF-E is noticeable around the end of zone II, where it increases up to ~-4h. More interestingly, it drops drastically at the end of zone III, reaching a maximum. As Qr augments, the NCR moves downstream, limiting the reach of flood currents. For Qr=500 $m^3 s^{-1}$, for instance, the NCR is found at 50 km.

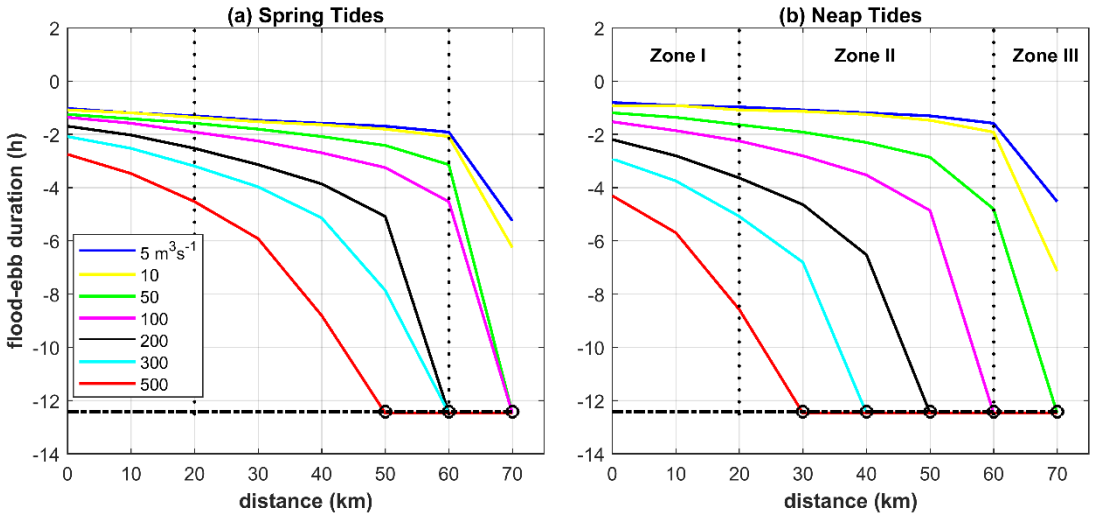

Figure 6. 9.- Differences in duration between flood and ebb (DDF-E) flows. The maximum difference in duration between flood and ebb that happens at -12.4 h is the point of no current reversal (marked with black circles). In the estuary, DDE-F is always negative as ebb duration is always greater than flood duration (a) For spring tides (b) For neap tides.

Even though in barotropic models stratification is not considered, at spring tides and Qr of up to 250 $m^3 s^{-1}$ flood flows and at the estuary head conditions can be considered well-mixed (Ferreira et al., 2003). According to Garel (2009a), there is an alternating establishment and breakdown of the two-layer residual flow with spring and neap tides. Therefore, in this case flood currents are actually blocked.

6.3.3.2- Weak tidal forcing: neap tides

Most of the comments on the spring tide forcing still applies to neap tides. The most obvious and interesting difference is the downstream shift of the NCR, which can be displaced as much as 20 km for moderate and large Qr (Figure 6.9b). For large Qr, flood currents are not able to reach further than 30 km upstream from PT0, leaving most of the estuary under the influence of Qr that runs seawards. It is worth noting that even though these values are not accurate due to the existing stratification, the NCR is always expected to happen closer to the estuary mouth than in the spring tide case. Therefore, the NCR obtained for the spring tide case can be considered the upper limit where flood currents still exist.

6.3.4. Relative phase between horizontal and vertical tidal movement.

An interesting parameter that provides information about morphology and tidal propagation along an estuary is the relative phase ($\emptyset_r=\emptyset_h-\emptyset_v$) between water level and current velocities (Savenije 2005, Friedrichs 2010), ($\emptyset_h$) and ($\emptyset_v$) , respectively, both are obtained from the harmonic analysis of water level and depth-averaged velocities. In the GE flood velocities are delayed respect to the water level propagation as indicated by positive values of the relative phase. Figure 6.10 shows this delay under average tide and different Qr indicated in the legend. At the mouth of the estuary, the relative phase is independent of Qr and slightly dependent on tidal forcing, varying from 57º under strong tidal forcing to 64º for weak forcing. Along the estuary, relative phase is very similar regardless of the tidal forcing no differences will be noticed between spring and neap tides therefore they will not be discussed separately. According to Friedrichs (2010), relative phase values between 45º and 90º, as it is the case of GE, correspond to long shallow equilibrium estuaries whose morphology is weakly to strongly funnel-shaped.

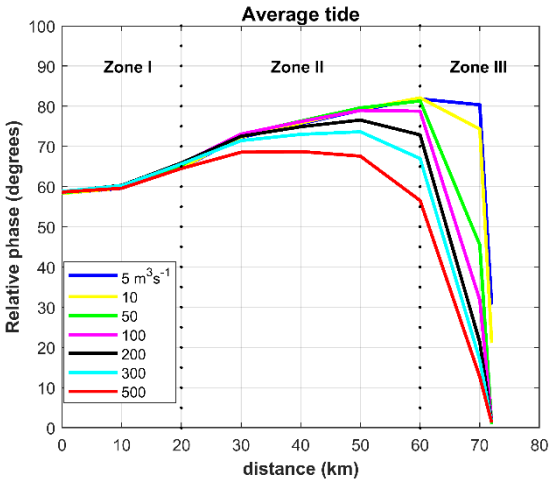

Figure 6. 10.- Relative phase along the estuary (difference between the phase of the water level, h, and the phase of the tidal flow velocity, v, $\emptyset_h - \emptyset_v$) during an average tide and different Qr, whose values are indicated in the legend.

In zone I the relative phase increases with distance with remarkable similarity for all Qr considered. For low Qr the relative phase goes increases in zone II, depicting a shape that agrees with the linearized theory of one-dimensional tidal propagation in long estuaries of constant depth (Toffolon and Savenije, 2011), which is reasonably representative for GE again. For large Qr, however, the relative phase does not increase in zone II, but maintains a rather constant value that even diminishes at the end of the zone. It is a consequence of the notable deformation that high Qr causes in tidal oscillation, which reduces the duration of the rising tide (enlarges the falling tide duration, see Figure 6.7), shifting the time of the high water and decreasing the relative phase consequently. This reduction of the relative phase is observed for all tidal forcing because the estuary becomes fluvial-dominated for large enough Qr, an expected behaviour. In zone III, relative phase is sharply decreased to zero, the point of maximum water height and the point of high water slack coinciding, indicating a standing wave.

6.4. Summary and conclusions

Applying a barotropic model in an estuary it is possible to determine the main hydromorphological changes due to the hydraulic control exercised by a dam. The study has been conducted for well-mixed estuaries strongly influenced by the tide. Estuary states prior to the opening of the dam have been reproduced using historical values of Qr

Likewise, it would be possible to know the hydromorphological changes in another estuary of similar characteristics where the construction of a dam is planned.

The model used is MOHID Water module from MOHID Studio 2016 and it has been verified in a meso-tidal estuary of the SW of the Iberian Peninsula, the GE, with Basos' Bathymetry (2013), and considering only realistic tidal forcing and freshwater discharge (Qr). Bathymetry had to be manually modified to comply with the observations in the estuary head by drawing a V-shape cross-section and introducing a sill at km 66. The model proved reasonably accurate for phase values of two tidal oscillations, elevation and current velocities. Tidal amplitude is also accurate, except around the sill at km 66, where it is systematically undervalued by the model, what can be due to bathymetry low resolution in this zone. Current velocities amplitude does not match observations, what can also be caused by partial stratification.

Simulations were run for several values of Qr within historical values, during spring and neap tides and during an averaged period. A harmonic analysis was performed on tidal amplitude and tidal current velocities. Given the shortness of the considered periods, two concepts were introduced for the harmonic constants discussion: Semi-diurnal Tidal Amplitude (STA), which corresponds to M2 output and is composed of all constituent waves that cannot be discriminated from M2 in this period, and Quarti-diurnal Tidal Amplitude (QTA), which is the equivalent for M4 output. These values were used for discussing tidal progression in amplitude (through rising-falling duration), current velocities (through ebb-flood duration) and the relative phase between them, which informs of the standing-progressive behaviour of the wave.

Following QTA behaviour, three zones with different tidal range behaviour are remarked and which depend on Qr. Zone I, in the mouth, shows tidally-dominated friction with a minor contribution from Qr, minor tidal wave deformation and mixed progressive behaviour. Zone II, in the inner estuary, shows a balance between friction and morphological convergence. In this zone, in places where friction increased and the delay of falling tide when Qr increased, it suggested the presence of flood areas. Zone III, in the estuary head, shows mostly a dependence with Qr (river dominated) where the tidal wave is severely damped, and becomes standing for high Qr.

The last two zones are those that have been most affected by the hydraulic control of Qr. In zone II, under well mixed estuarine conditions, the volume of Qr determined the

maximum reach of the flood tide, developing the point of no current reversal (NCR). It has been proved that from a certain discharge these estuaries have a dissipative behaviour regardless of the tidal forcing. That some areas do not flood again due to the decrease in Qr reduces the river flow to a narrower channel permanently. In this way there is a greater influence of the tide upstream and, therefore, the progressive nature of the tidal wave, which will influence morphological changes in the estuary. On the other hand, these areas that for a long time remained flooded will not provide eroded material to the main flow or the natural environment of the aquatic ecosystem being confined to a smaller area. But there is no information on both effects because they have not been taken into account in the simulations. In the GE, according to Wolanski et al., (2006), the Alqueva dam regulates Qr to be under 50 m^3s^{-1}. The simulation shows that for such values, flooding area will be reduced, especially at PT4 and PT5 locations. The point of no current reversal (NCR) will not occur within the estuary limits anymore and standing waves will not form on the estuary head either.

Because of everything said above, it is feasible to say that to maintain a constant water quality flow in the estuary it is not enough, it is necessary to maintain the seasonal variability.

Acknowledgements

We acknowledge the pre-doc fellowship to Campus de Excelencia Internacional del Mar (Plan ReSEArch Agregación-CEIMAR: 18INAC0284) and for the support for a stay to University of Algarve. We are grateful to the Maretec, 'Marine and Environmental Technology Research Center', which belongs to the High Technical Institute of the University of Lisbon and, especially, to Frank Braunschweig for their assistance in the handling of the MOHIDStudio2016. The SIMPATICO monitoring station was purchased through a national programme for the re-equipping of scientific institutions (Reeq/484/MAR/2005).

ANNEX 6.1

6.A1.1.- Harmonic constituents at the ocean boundary

Table 6. A1.- Harmonic constants of the main constituents used to reconstruct the tidal signal on the continental shelf boundary. The constants have been obtained from the global tide-model FES2004. Only harmonic constants with amplitudes greater than 1 cm are listed in the table, although the model includes some more with amplitude below this threshold. M4 is intentionality included, despite its zero amplitude, in order to emphasise the fact that this shallow water constituent of non-linear origin is null at the boundary but it is locally generated in the estuary by the model.

Constituent	Amplitude (m)	Phase (degrees)
M2	1.02	57
S2	0.40	83
K1	0.07	49
K2	0.10	76
N2	0.22	40
2N2	0.03	19
O1	0.06	311
Q1	0.02	48
P1	0.02	262
M4	0	-

6.A1.2.- Data used for calibration/validation

Table 6.A2.- Observations collected along the GE estuary that have been used for model calibration. All water level observations have been collected after the Alqueva dam construction (February 2002) but only ST4 current meter observations are later than this date. Despite being previous to the dam construction, the other current meter observations have been also included in the calibration out of necessity (see comments in the text)

	Location		Period validation		Sampling interval (min)	Distance (km)	Observations
Name	Lat (North)	Lon (West)	Start	End			
ST1 (Choças)	37º17'35''	7º26'6''	21/11/2001	5/12/2001	5	15	Current – meter Aanderaa RCM-9
ST2 (Alamo)	37º22'36''	7º26'18''	20/11/2001	4/12/2001	5	23	Current – meter Aanderaa RCM-9
ST3 (Alcoutim)	37º28'18''	7º28'12''	20/11/2001	4/12/2001	5	35	Current – meter Aanderaa RCM-9
ST4 (Promedeiros)	37º30'2''	7º29'7''	30/12/2005	19/1/2006	10	40	Current – meter Aanderaa RCM-9
ST5 (Pomarao)	37º33'18''	7º31'30''	19/11/2001	4/12/2001	5	50	Current – meter Aanderaa RCM-9
PT0	37º10'58''	7º24'29''	31/7/2015	31/8/2015	10	0	Tidal – gauge
PT1	37º15'9''	7º26'2''	31/7/2015	31/8/2015	10	10	Tidal – gauge
PT2	37º21'13''	7º26'24''	31/7/2015	31/8/2015	10	20	Tidal – gauge
PT3	37º25'57''	7º27'32''	31/7/2015	31/8/2015	10	30	Tidal – gauge
PT4	37º30'13''	7º29'17''	31/7/2015	31/8/2015	10	40	Tidal – gauge
PT5	37º33'18''	7º31'30''	31/7/2015	31/8/2015	10	50	Tidal – gauge
PT6	37º34'59''	7º35'37''	31/7/2015	24/9/2015	10	60	Tidal – gauge
PT7	37º37'45''	7º40'00''	31/7/2015	24/9/2015	10	70	Tidal – gauge
SIMPATICO	37º11'20''	7º24'45''	3/11/2012 31/7/2013	3/12/2012 31/8/2013	15	0	Continuous monitoring

6.A1.3.- Grid characteristics and other inputs in the model.

Table 6.A3. Some characteristics of the grid, time step using to run the model and physical parameters resulting of the calibration of the model.

Parameter	Numerical value
Grid dimensions	2209 x 122
Cell size inside the estuary	[10,70]m
Time step	5s
Horizontal Viscosity	3.00 m^2s^{-1}
Friction coefficient	0.002

7.- HARNESSING THE ENERGY OF MARINE CURRENTS IN MESO-TIDAL ESTUARIES. VIABILITY IN THE GUADIANA ESTUARY (SW IBERIAN PENINSULA) (Paper pendiente de ser enviado).

***María Concepción Calero Quesada*[(a)]**, *Jesús García-Lafuente[(a)], Javier Delgado Cabello[(a)], Francisco Javier Campuzano[(b)(c)]*

[(a)] Physical Oceanography Group of the University of Malaga (GOFIMA), Spain.

[(b)] MARETEC/LARSyS, Instituto Superior Técnico, Universidade de Lisboa, 1649-004 Lisbon, Portugal.

[(c)] CoLAB +ATLANTIC, Molhe Leste, 2520-620 Peniche, Portugal.

conchi.calero@ctima.uma.es

Abstract

Tidally-driven estuaries are water systems where marine currents are strong to be used as a renewable energy. To optimize energy extraction reducing the impact it is necessary to delimit the area to install a turbine farm. The aim is to find the most viable area in the meso-tidal Guadiana Estuary and assess the energy that can be extracted. A parametric approach was carried out considering different characteristics of the flow. They were represented by numerical indicators integrated in an empirical equation which gives a value to decide the viability of an area. The method indicates that the most viable area is the lower area of the estuary during spring tides with ebb flow. Flows have been modelled by the hydrodynamic system MOHID that was implemented by a module in order to simulate a 105-turbine farm. The monthly average power extracted from the whole farm is 29 KW ($7.5 \cdot 10^4$ MJ per month). The propagation of tidal wave was investigated under different conditions to assess the impact of the farm to find that it has no significant effect in the amplitude of tidal wave but it modifies slightly the duration of the falling tide far upstream in the estuary in neap tides.

Keywords: meso-tidal estuary, MOHID system, energy extraction, parametric approach, module turbine, tidal propagation.

Abbreviations:

· COP25: Climate summit number 25

· EU: European Union

· GE: Guadiana Estuary

· VRSA: Vila Real de Santo Antonio (Portugal)

· SMP: SIMPATCO, Integrated System for Monitoring Parameters Type in Coastal areas.

· GIS: Geographic Information System

· FES: Finite Element Solution

· Qr: Freshwater discharge

· D: Diameter

· MCT: Marine Current Turbine

· TAT: Time interval during which the energy flux is Above a Threshold value.

· TFP: Time interval during which the energy flux does not change sign.

· TFU: Time interval during which the flow lays along a given direction.

· FN: high frequency phenomena or noise.

· FS: Vertical shear of the flow.

· V: Quality function or viability.

· M2: Semidiurnal signal of the tide.

· M4: Quartidiurnal signal of the tide.

7.1.- Introduction

7.1.1.- Theoretical framework

In November 2019, the European Parliament declared the climate emergency during the development of the climate summit COP25. In December 2019, the UE committed to activate a package of measures to face the climate emergency through its Green New Deal to get climate neutrality in 2050, that is, that only what the Earth to be able to absorb. To achieve this neutrality, the Green New Deal pledges to energy efficiency and to develop an electricity sector based on renewable energies.

Oceans represent an important renewable energy resource although technology is no so developed as other renewable energies, like solar or wind energy, due to its high cost

(IRENA, 2014). Energy from the oceans can be obtained in different ways such as waves, tidal range, tidal currents, marine currents, ocean heat energy and salinity gradient. Technology employing the horizontal flow that accompanies the rising and falling of the tide is in advance stage, as the case of the tidal plant in Rance (France) (IRENA, 2014). Conversely, technology which use kinetic energy of the tide is still in an early stage (Brito and Melo et al., 2016).

Intense ocean currents often take place in shallow areas like rivers and estuaries (Carballo et al., 2009). Estuaries have undisputable advantages over other water systems to extract energy: The flow is channeled by the topography making the currents to be intense and unidirectional (Nishino and Willden, 2012). Moreover, they are accessible for assembly and subsequent maintenance of the devices, for which they are recommended areas to test prototypes (Pacheco and Ferreira, 2016). In fact, there are prototypes adapted to rivers and estuaries like Evopod turbine in the Ria Formosa (South Portugal) scaled to 1:10th (Pacheco et al., 2018). Thus, it is possible to predict the behavior of devices working on areas of difficult access such as the Strait of Gibraltar, more concretely in the area of the Espartel Sill, where an intense and rather unidirectional flow with adequate characteristics to extracting energy exists (Calero Quesada et al., 2014).

Energy flux is calculated as:

$$\vec{E}_{flux} = \frac{1}{2}\rho\bar{u}^2\vec{u} \qquad (7.1)$$

where ρ is the seawater density, whose representative value is 1027 kgm^{-3} in this work and u is the velocity of the flow. When a preferred direction exists, which is the longitudinal one in estuaries, the energy flux is constrained to this direction and calculated by:

$$E_{flux} = \frac{1}{2}\rho(u_1^2 + u_2^2)u_1 \qquad (7.2)$$

where u_1 is the longitudinal component of velocity and u_2 the transversal one.

Energy extraction from marine currents depends on the location (O'Rourke et al., 2014). It is important to know the hydrodynamic of this location in order to select the right devices and adapt them *ad hoc* for an optimum use and, also, it would allow to evaluate the effects of devices on hydrodynamics beforehand (García-Oliva et al., 2017; Ramos and Iglesias, 2013; Bryden and Couch, 2013). On the other hand, estuaries are sensitive to changes performed in its interior so the right election of devices and of the

emplacement are essential aspects to take into account previously to the design of a turbine farm (Nash et al., 2014; Bahaj et al., 2007).

The aim of this work is to know the amount of energy available for extraction form marine currents in the meso-tidal estuary of Guadiana River, SW Iberian Peninsula (Figure 7. 1). For that purpose, a parametric approach has been considered to identify areas and periods of time in which currents in the estuary are favorable. This method was already used in the Strait of Gibraltar (Calero Quesada et al., 2014) and now is applied to the Guadiana Estuary (GE, hereinafter). To obtain the energy extraction in this place, system MOHID was implemented by a module turbine by representing a turbine farm (Balsells Badia, 2017).

7.1.2.- Study area

The GE is a meso-tidal estuary, shallow and narrow, situated in the south of the Iberian Peninsula, being the border between Spain and Portugal. Its width decreases exponentially from 800 m at the mouth to 70 m at the head located 80 Km upstream (Fortunato et al., 2002; Ruíz Muñoz et al., 1996) where the tide is blocked by a dam. The mean depth is about 5 m although reaches 18 m at certain places (Ruíz Muñoz et al., 1996; Garel, 2017). Climatologically, there is a wet season that extends from November to January and a dry season from July to August (Morales et al., 1993). Since the inauguration of the Alqueva dam 120 Km upstream in year 2002, the freshwater discharge (Qr, hereinafter) is regulated. Tidal range at the mouth varies between 1.5 m in neap tides and 3.5 in spring tides (Garel and Ferreira, 2013) which classifies the estuary in meso-tidal category. Semidiurnal periodicity prevails being M2, S2 and N2 the main tidal constituents of this species while K1 and O1 are the main of the diurnal one Garel et al., 2009a) (see table 7.A1, Appendix 7.1).

In an estuary, the strongest currents usually occur in the vicinity of the mouth. This is the widest and deepest area of the GE and it would be the most recommendable area to install a turbine farm from a practical and economical point of view. Previous works (Calero Quesada et al., 2019) showed that the zone 2030 Km upstream from the mouth are strongly influenced by tidal currents and weakly by Qr. Therefore, energy extraction in this area is rather independent of Qr, that is, of the variability between wet and dry periods.

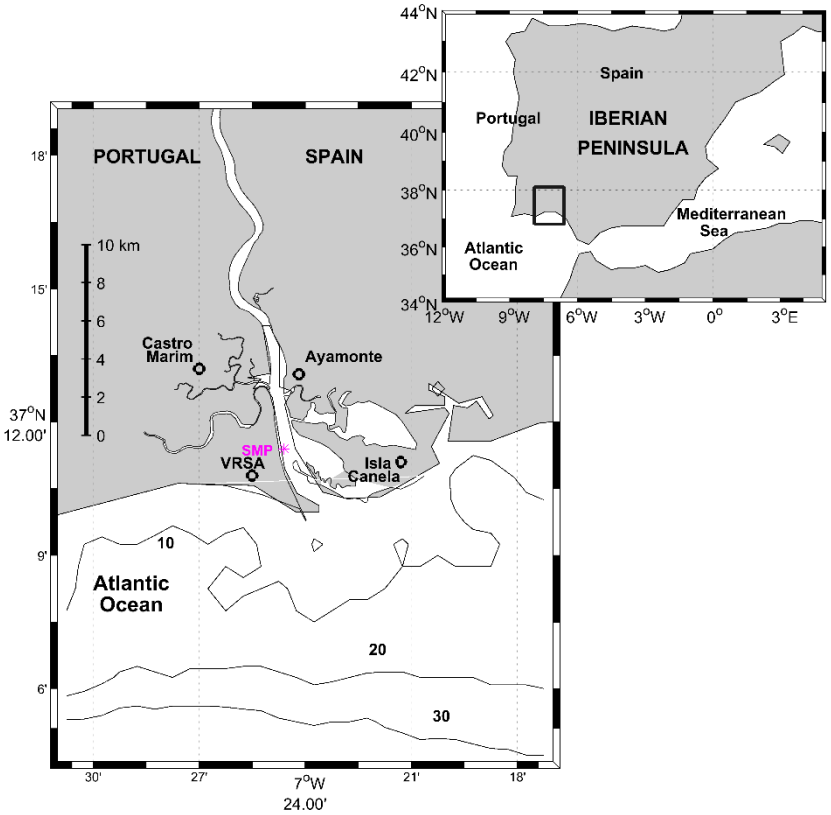

Figure 7. 1.- Map of the low area of the GE and its location in Iberian Peninsula (box in the top right). Some locations of Spain and Portugal are showed in bold (VRSA stands for Vila Real de Santo Antonio). Pink asterisk shows the position of the monitoring system SIMPATICO (SMP, see text).

7.2.- Methodology

7.2.1.- In situ measurements

In situ observations from the environmental station "Integrated System for Monitoring Parameters Type in COastal areas (Portuguese acronym SIMPATICO, SMP hereinafter; see figure 7.1) are available (Garel et al., 2009b; Garel and Ferreira, 2011; 2015). This autonomous recording system had a bottom-mounted acoustic current-meter profiler (Sontek Argonaut XR, 750 kHz) and operated from March 2008 to April 2014. The SMP samples horizontal currents at ten levels of the vertical profile.

Actual values of Qr freely available from the Instituto de Agua de Portugal (INAG, Portuguese Environment Agency, http://snirh.pt) were used to validate the model currents with measurements of SMP station.

7.2.2.- Model and bathymetry

7.2.2.1. MOHID system

The hydrodynamic system MOHID is an open-source modular system that comprises numerical models, graphical interfaces and other pre- and post-processing tools (Braunschweig et al., 2004; Miranda et al., 2000; MOHID, 2002, http://www.mohid.com/). The code is written in Fortran using an object-oriented programming strategy. The MOHID package includes GIS module which handles spatial and temporal variable data in specific formats required or produced by MOHID and MOHID GIS (Braunschweig et al., 2005).

MOHID Water is a three-dimensional hydrodynamic model developed to simulate surface water bodies using Finite Volume method in the real domain without any spatial transformation. Model solves the hydrostatic equilibrium Navier-Stockes equations under Boussinesq and Reynolds approximations. In Cartesian coordinates the equations are (Martins et al., 2001):

$$\frac{\partial u_1}{\partial x_1} + \frac{\partial u_2}{\partial x_2} + \frac{\partial u_3}{\partial x_3} = 0 \quad (7.3)$$

$$\frac{\partial u_1}{\partial t} + \frac{\partial (u_j u_1)}{\partial x_j} = f u_2 - g \frac{\rho_\eta}{\rho_0} \frac{\partial \eta}{\partial x_1} - \frac{1}{\rho_0} \frac{\partial p_S}{\partial x_1} - \frac{g}{\rho_0} \int_z^\eta \frac{\partial \rho'}{\partial x_1} dx_3 + \frac{\partial}{\partial x_j} \left(A_j \frac{\partial u_1}{\partial x_j} \right) \quad (7.4)$$

$$\frac{\partial u_2}{\partial t} + \frac{\partial (u_j u_2)}{\partial x_j} = -f u_1 - g \frac{\rho_\eta}{\rho_0} \frac{\partial \eta}{\partial x_2} - \frac{1}{\rho_0} \frac{\partial p_S}{\partial x_2} - \frac{g}{\rho_0} \int_z^\eta \frac{\partial \rho'}{\partial x_2} dx_3 + \frac{\partial}{\partial x_j} \left(A_j \frac{\partial u_2}{\partial x_j} \right) \quad (7.5)$$

$$\frac{\partial p}{\partial x_3} = -\rho g \quad (7.6)$$

Equation (7.3) is continuity for incompressible fluids, (7.4) and (7.5) are the Navier-Stockes equations for horizontal velocities and (7.6) is the hydrostatic equation. In them, (x_i) are the Cartesian coordinates (longitudinal, transversal and vertical, for x_1, x_2 and x_3, respectively), (u_i) are the velocity components in the coordinates x_i, η is the free surface, A_i, the turbulent viscosity coefficients, f, the Coriolis parameter, p_s, the atmospheric pressure, g, the acceleration of gravity, ρ_0 the local density, ρ a mean density, ρ' is the density anomaly referred to the depth-averaged density and ρ_η is the density on the surface. Density has been calculated from the salinity and temperature through the seawater equation of state (Leenderstee and Liu, 1978).

MOHID Water has been applied to coastal and estuarine areas and it has showed its ability to simulate complex features of the flows. Different environments have been studied along the Portuguese coast, including the main estuaries as the Minho (Sousa et al., 2014)

Douro (Abreu, 2010), Mondego (Ascione Kenov et al., 2012), Tagus (Valentim et al., 2013; Pablo et al., 2019), Sado (Vaz et al., 2009), Guadiana (Calero Quesada et al., 2019) and coastal lagoons as Ria de Aveiro (Valentim et al., 2013) and Ria Formosa (Leitao et al., 1996). The model also has been applied in most Galician Rías and some European estuaries - Western Scheldt (Netherlands), Gironde (France) (Cancino and Neves, 1999)… In this paper, MOHID Water is applied to the GE to study water level and currents at five layers of equal thickness. Barotropic tide gives the solution of the first order wave equation of shallow, funnel-shaped estuaries (Friedrichs, 2010) and can be used to describe the propagation of tidal wave. To this regard, it is worth mentioning that GE is well-mixed and the effect of stratification or the strain-induced periodic stratification is negligible (Garel et al., 2009; Simpson et al., 1990; Ferreira et al., 2003) especially in the mouth, where this study focuses.

Either actual Qr values from INAG or constant values are specified as input conditions at the inland closed boundary. Tidal sea level oscillations are prescribed at the open boundary inthe continental shelf. The harmonic constants used to reconstruct the barotropic tidal oscillations on the shelf have been retrieved from the global Finite Element Solution tidal model FES2004 (Lyard et al., 2006), a tool included in MOHID Studio (graphical user interface to MOHID Water modelling system, http://www.MOHID.com). The most important ones are listed in Table 7.A1 in the Annex. Although MOHID Water can deal with atmospheric (wind-stress, pressure) and radiative (solar heating, evaporation, etc.) forcings, they have not been included in this study.

7.2.2.2 Bathymetry

The model uses the high resolution curvilinear bathymetry implemented by (Basos, 2013) (http://www.hidrografico.pt/download-gratuito.php). It comprises 300 m of the continental shelf and extends to 80 km inland. Figure 7.2 shows the whole bathymetry and a zoom of the lower area where the study focuses.

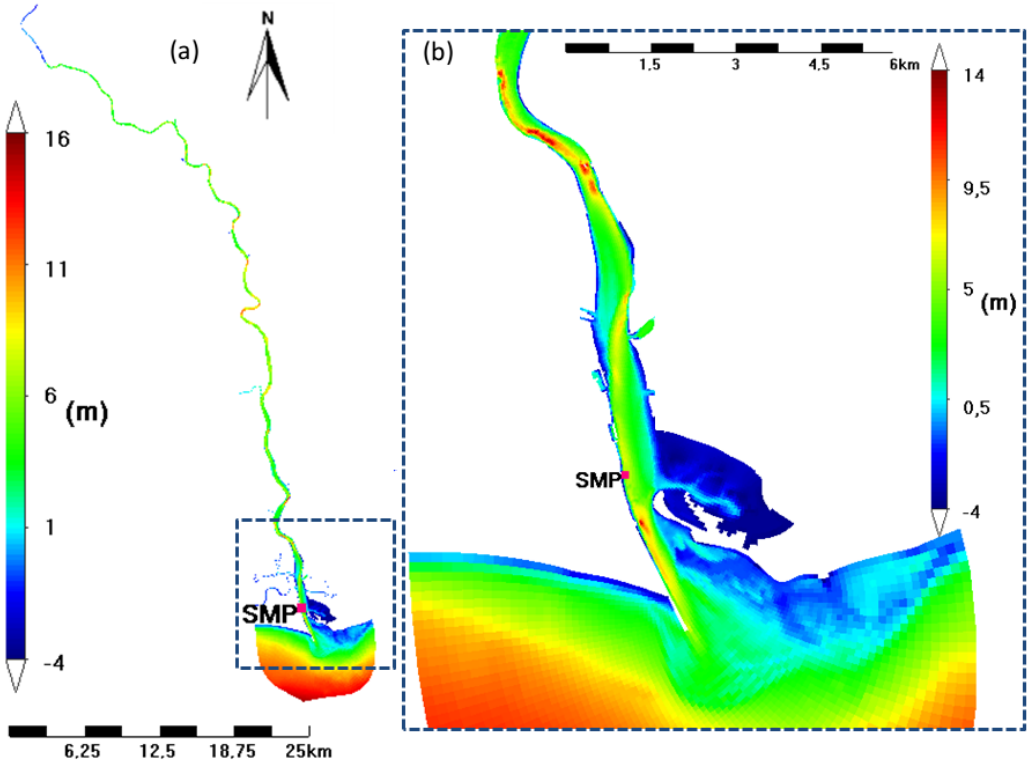

Figure 7. 2.- Panel a) Bathymetry of the model domain (left scale). The 0 m contour is the hydrographic zero. Positive values (colours from cyan to red) are depths below zero and negative values (deep blue) are above zero. Panel b) is a zoom of the lower estuary (right scale). In both panels the autonomous monitoring system SMP is indicated.

7.2.3.- Validations and simulations

In estuaries, currents are usually more intense in the surface layer so that this portion of the water column is more suitable for energy extraction. Accordingly, the vertical profile of the water column has been discretized in 5 layers of equal thickness, the 5th being the most superficial one and the focus of this work. Current velocity in it has been compared with observations in SMP. Since this system measures horizontal velocity at ten levels (Garel et al., 2009b) the average value of layers 9 and 10 was used to compare with the output value of layer 5 of the model.

Having long time series from SMP simultaneously to real Qr data, it has been possible to carry out that comparison for both, dry and wet periods, which allows for a more robust validation. As the model has no meteorological forcing, the validation has been realized by comparing harmonic constants of the longitudinal velocity produced by the model. Table 7.1 presents amplitudes and phases of the main semidiurnal tidal (M2, S2 and N2) and diurnal (K1 and O1) constituents. M4, which represents friction of the tide inside the

estuary, has been included too. There is a good agreement in amplitudes and phases of semidiurnal constituents. Diurnal ones are little relevant, although they still show a good agreement in amplitudes but not in phases, which is probably due to their little representativeness that makes them be badly reproduced by the model. The same happens with quartidiurnal component, which shows good agreement in amplitude but not in phase. The discrepancy in this case may arise from the fact that SMP is close to the open boundary where zero value is assigned to M4 in the model boundary conditions.

Table 7. 1.- Amplitudes and phases of the main tidal constituents measured in SMP and produced by the model (in italics).

Superficial layer	WET month		DRY month	
Constant	Amplitude (m/s)	Phase (degrees)	Amplitude (m/s)	Phase (degrees)
M2	0.84 ± 0.05	1 ± 3	0.85 ± 0.05	3 ± 3
	0.87 ± 0.02	*6 ± 1*	*0.87 ± 0.04*	*6 ± 2*
S2	0.24 ± 0.05	15 ± 14	0.33 ± 0.06	48 ± 8
	0.27 ± 0.02	*25 ± 4*	*0.37 ± 0.03*	*45 ± 6*
N2	0.23 ± 0.05	350 ± 14	0.15 ± 0.05	335 ± 18
	0.18 ± 0.02	*356 ± 4*	*0.18 ± 0.04*	*356 ± 11*
K1	0.04 ± 0.03	205 ± 61	0.05 ± 0.02	94 ± 9
	0.03 ± 0.01	*10 ± 14*	*$0.04 \pm 1 \cdot 10^{-4}$*	*346 ± 1*
O1	0.02 ± 0.03	211 ± 99	0.03 ± 0.03	143 ± 53
	0.04 ± 0.01	*246 ± 12*	*$0.03 \pm 5 \cdot 10^{-4}$*	*242 ± 1*
M4	0.06 ± 0.06	149 ± 80	0.05 ± 0.04	187 ± 64
	0.06 ± 0.01	*359 ± 9*	*0.05 ± 0.01*	*357 ± 7*

7.2.4.- Module turbine

The energy extracted by a farm of Marine Current Turbines (MCTs, hereinafter) and the effect that they have on the estuarine currents have been studied implementing the MOHID system with module turbine (Balsells Badia, 2017). This module provides the best approach to harness energy from marine currents and the impact of MCTs in the flow. The main consideration in the design of the module is the application of a two- and

three- dimensional model for axial turbines which can operate in both directions and free rotation of the vertical axis doing current velocity always be perpendicular to the blades.

There are several approaches to model the effects of turbines both in two- and three-hydrodynamic models. Most of them are based on the same premise, represent the turbines as a momentum sink adding a reaction force in the hydrodynamic of the model. Thus, power is interpreted as the product of reaction force and current velocity

$$P_T = F_T u_1 \qquad (7.7)$$

where P_T is the power turbine, F_T is the reaction force and u_1 the longitudinal component of velocity. Velocity is a model output used to calculate F_T according:

$$F_T = \frac{1}{2}\rho A_T C_T u_1^2 \qquad (7.8)$$

where ρ is water density, A_T is the area swept by the blades, C_T is the thrust coefficient that quantifies the force exerted by the turbine to the flow. On the other hand, power can be calculated as

$$P_T = \frac{1}{2}\rho A_T C_P u_1^3 \qquad (7.9)$$

where C_P is the power coefficient that quantifies the amount of power extracted from the flow. Some models use the same coefficient for thrust and power, what means that the work done against the flow is the same as the energy extracted from it but, as it is expected, thrust coefficient have to be greater. For more details about these coefficients, see (Bahaj et al., 2007; Balsells Badia, 2017).

As the model has vertical spatial discretization, the turbine area A_T has been divided in layers of areas $A_{T,K}$ each one (see figure 7.3) obtained as

$$A_{T,K} = \frac{r^2}{2}\theta - r\sin\left(\frac{\theta}{2}\right) d - \sum_{K=1}^{K} A_{T,K-1} \qquad (7.10)$$

where K is the number of layers implied in the turbine swept area, r is the radio of turbine, θ is the angle between blades, and d is the vertical distance between the center of the rotor and layer K.

Basic parameters of the turbines are the same for all the simulations. The force exerted by the anchoring structure has not been considered. A security factor in the cut-in of speed of 15 % is assumed. It means that, once the turbine starts to turn, it does not stop spinning until the velocity of the current falls below the 85% of the cut-in speed. If the current

speed falls under this value, it needs to reach the cut-in speed again for the turbine rotor to start rotating again.

Energy extraction is obtained by numerical integration of the power. For a constant intervals Δt, the energy extracted after n iterations (at time $n\Delta t$) is

$$E_T = \sum_{i=0}^{n} P_T \Delta t \qquad (7.11)$$

The outputs provided by the module turbine gives are the instantaneous power, the energy extracted at time t and the current velocity modulus at each MCT and for the whole farm. As inputs, the module requires the spatial coordinates of each MCT, the cut-in speed V_C (V_C = 0.5 ms^{-1} in this work), the diameter of the turbine, D, and the distance between the estuary floor and the lowest point of the area swept by the blades, Z_{min}. This distance must be greater or equal to 25 % of the local thickness of the water column in the lowest astronomical ebb to reduce the turbulence and shear in the bottom layer and also to allow for the free movement of eventual dense and potentially harmful materials drifted by the flow (EMEC, 2013; Hass et al., 2011).

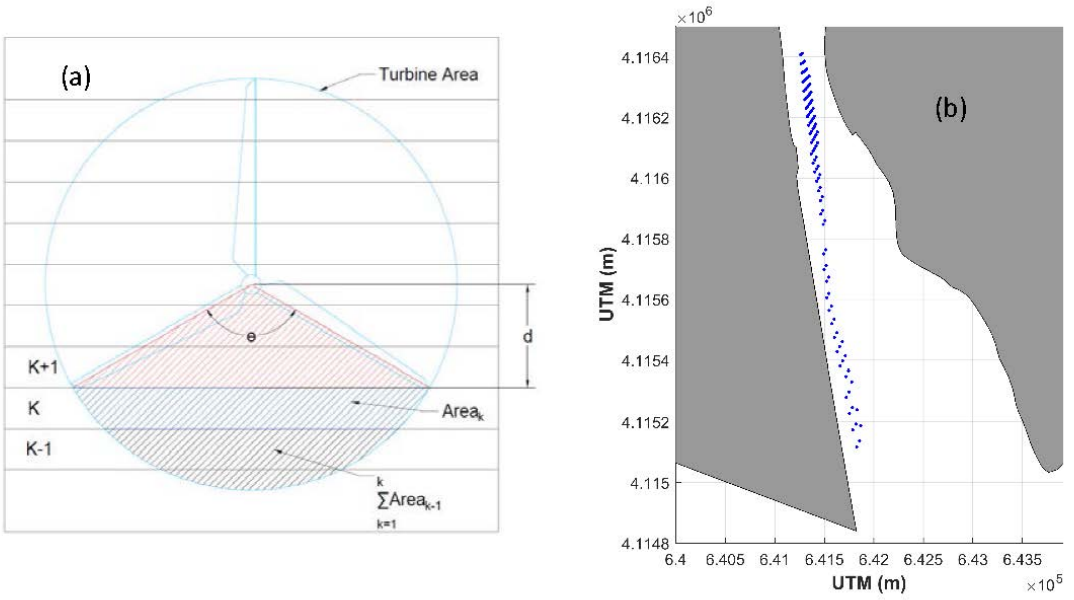

Figure 7. 3.- Panel a) Vertical discretization of the turbine in the module turbine. The parameter K refers to the layer in which the turbine has been discretized and d is the distance between the center of the rotor and layer K. Panel b) Distribution of the turbines inside the farm in the GE. The total of 105 axial turbines of D=2 m diameter occupies an area of 0.36 km^2.

7.3.- Evaluation of the flow properties applied to the energy extraction.

7.3.1.- Characteristics of the flow

Regarding the energy extraction, the available energy flux is the key variable. However, there are other flow characteristics that must be considered for the election of the operating device and for the emplacement of the farm in order to improve efficiency and optimize energy extraction (O'Rourke et al., 2011).

A method based on indicators has been applied that quantifies other relevant characteristics of the flow. This method has been previously used in the Strait of Gibraltar with satisfactory results (Calero Quesada et al., 2014), and now is applied to GE to show that it can be generalized to other systems. Only the lowest part of the estuary, where there are strong currents (Calero Quesada et al., 2019; Garel et al., 2009b) and favorable topographic features of width and deep, have been considered in the GE. Even with this geographical restrictions, it is necessary to delimit correctly the most viable area, which justifies the application of the method used in (Calero Quesada et al., 2014). In the following sections, a set of indicators are defined and adapted to GE. To calculate these indicators simulations with real Qr were used.

7.3.1.1 Average energy flux

Figure 7.4 shows the average value of the energy flux at the mouth of the GE during a period of a month and another period embracing spring tides (about 7 days), using equation (7.2). The figure shows absolute values of the equation, even though, strictly speaking, the flux is positive (negative) if it points upstream (downstream) the estuary. It has been also calculated for neap tides. However, in this case, the flow does no reach the critical velocity V_C and it is not appropriate to harness the energy, so that these results have not been included in figure 7.4.

Highest values occur in spring tides, especially during ebb flow, reaching values of 900 Wm^{-2} almost over the whole lower GE (Figure 7.4f), with peaks of 1200 Wm^{-2} downstream SMP. This amount of energy compares well with that available in other marine areas like the Strait of Gibraltar, specifically in Tarifa (South of Spain), an area which has been considered for the installation of a farm (Calero Quesada et al., 2014). The energy peaks are located around 3 Km downstream of SMP, although the area

upstream this site is not discarded as it shows positive and negative fluxes of intensity between 500 and 600 Wm^{-2} (absolute values) respectively (Figure 7.4d,e,f).

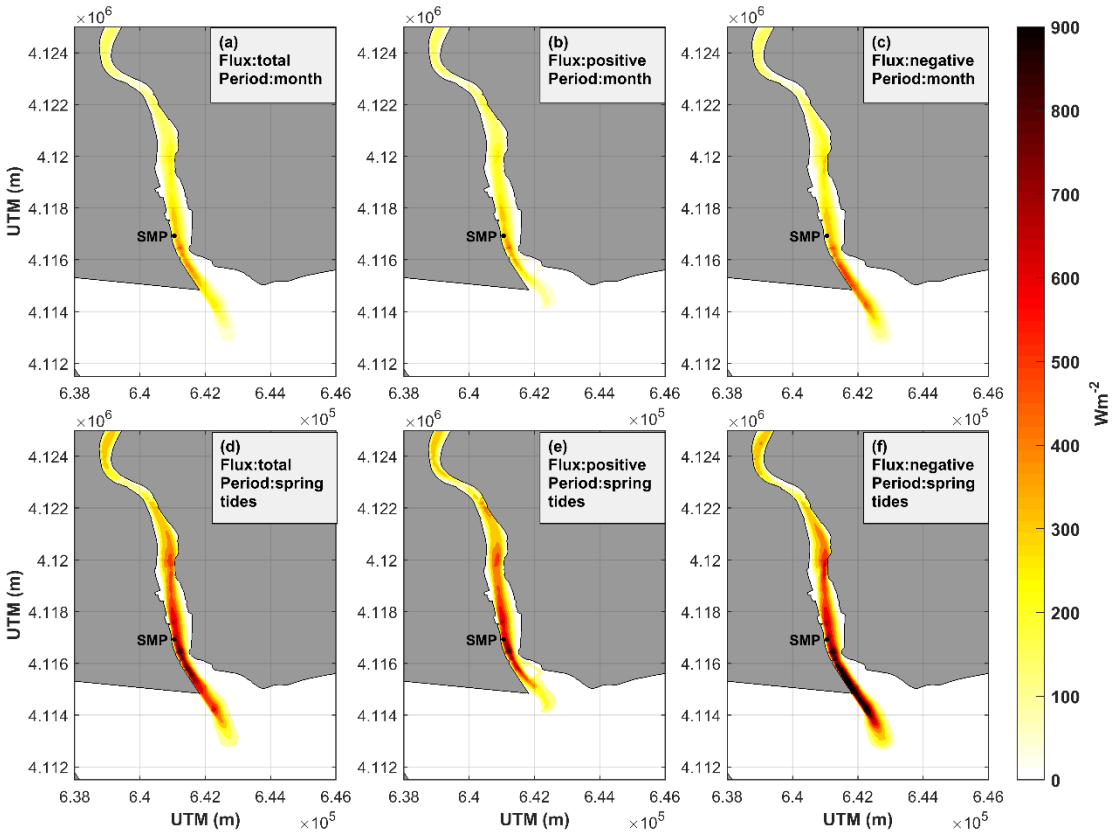

Figure 7. 4.- Average energy flux in the lower area of the GE under different periods and for the two possible directions of the flow (according the legend in the panels). Total averaged energy flux, upstream flux (positive) and downstream flux (negative) are presented in the panels of the left, center and right columns, respectively.

7.3.2.- Other relevant parameters

7.3.2.1. Time interval during which energy flux is above a threshold value (TAT).

In order for a turbine farm to be profitable, the energy flux must exceed a threshold value during long time intervals. For that, the parameter time interval during which energy flux is above a threshold values (*TAT*), is defined as the percentage of time during which the flux intensity is greater than the threshold. The selected threshold is 200 Wm^{-2} that corresponds to a current of 0.73 ms^{-1} according to equation (7.2). This speed is greater than the cut-in speed, V_C=0.5 ms^{-1}, introduced previously in module turbine but it would the speed from which energy extraction would be profitable.

Figure 7.5 shows the *TAT* distribution in the lower GE. Greatest percentages are observed during spring tides and negative fluxes, reaching values up of 70% or more (Figure 7.5f)

spreading over almost the whole width of this area of the estuary. The percentage falls to 45 % for positive flux (figure 7.5e), confirming the flood-ebb tide asymmetry (Calero Quesada et al., 2019). Without distinction between them, the mean percentage during spring tides reaches 60 % in almost the whole width of the estuary (figure 7.5d). For the month average period (upper panels, figure 7.5) the variability of *TAT* resembles that of spring tides with notably smaller values, which makes the area downstream SMP the only interesting zone under these condition (figure 7.5c).

Figures 7.5 and 7.5 show how the values during monthly averages (top panels) are attenuated with regard to those of spring tides average (bottom panels). This supports the fact that neap tide periods are not profitable for energy extraction. On the other hand, if only monthly averages are considered, the potential for the instantaneous energy extraction from the estuary would be underestimated.

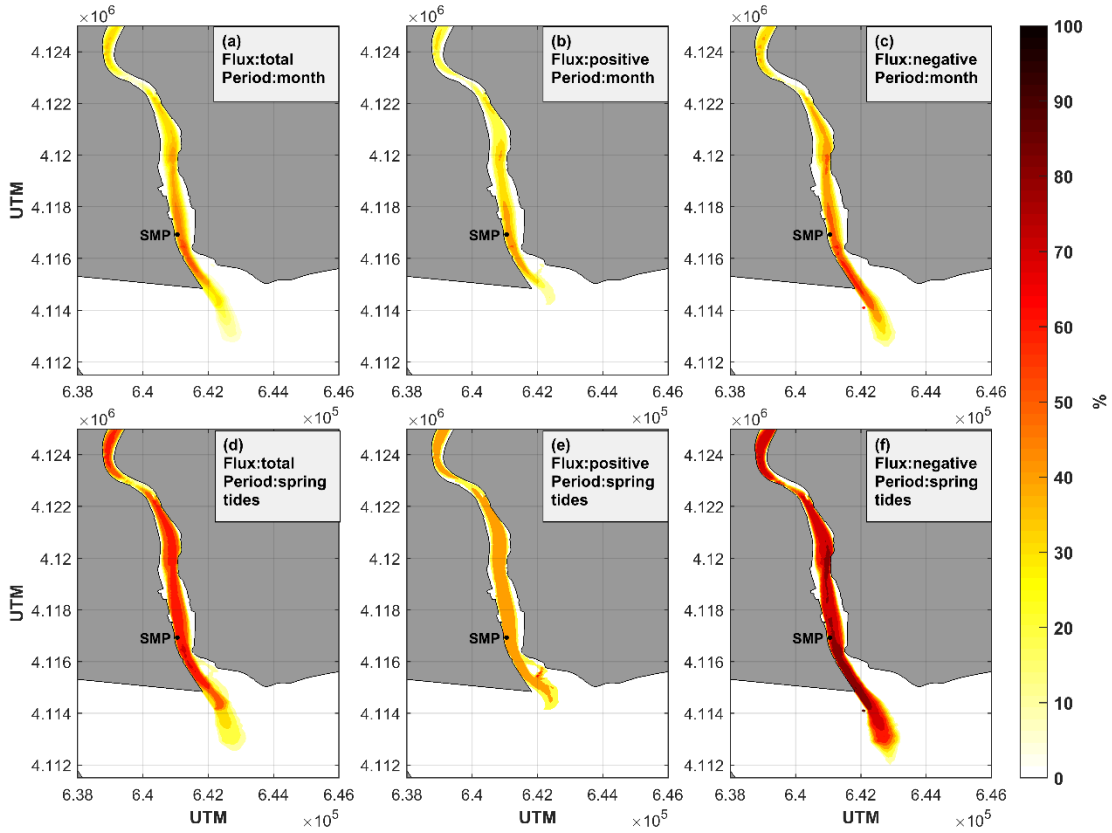

Figure 7. 5.- Time percentage during which the energy flux exceeds 200 Wm^{-2} (TAT). Panels follow the same scheme as in figure 7.4.

7.3.2.2 Time interval during which the energy flux does not change sign (TFP).

Some devices work only for unidirectional currents, that is, they extract energy when the current flows in a direction but they stop operating if the flow reverses. For such devices, the definition of a new parameter that quantifies the time percentage during which energy flux does not change sing (*TFP*) is convenient. There are two directions for the currents in an estuary. The time during which the current remains in a direction is similar but not the same because the asymmetry between flood-ebb tides. In the GE, *TFP* is 45 % for flood tide and 55 % for ebb tide, in both cases occupying the whole lower GE (Calero Quesada et al., 2019; Garel et al., 2009b) regardless the time interval considered.

7.3.2.3. Time interval which the flux lays along a given direction (TFU).

Other devices have not its motion axis fixed so they work perpendicular to the flow direction. Considering the situation in which the flux does not change sign, the direction of the flow can change and diminish the efficiency and performance of these devices. It is convenient to define a parameter that quantifies the time interval during which the flow remains within a given direction (*TFU*). The percentage of time that the flow maintains a given direction with a tolerance angle of $\pm\,\theta$ (which in this work has been taken as 30º) has been computed to this aim. This parameter is more restrictive than the previous *TFP* and identifies areas where the flows are rather unidirectional, a crucial condition for this type of devices (Li et al., 2011; Goundar and Raffiudein, 2013). Figure 7.6 represents the distribution of this parameter considering two main directions which are 115º and 290º for flood and ebb tide, respectively. *TFU* values are homogeneous in the channel of the estuary with 45 % for flood tide and 55 % for ebb tide. These values match the *TFP* because the GE is a channeled estuary. Notice, however, that at the mouth the distribution of *TFU* is not homogeneous, rather the contrary, there are important changes of the TFU that could compromise the performance of a turbine farm.

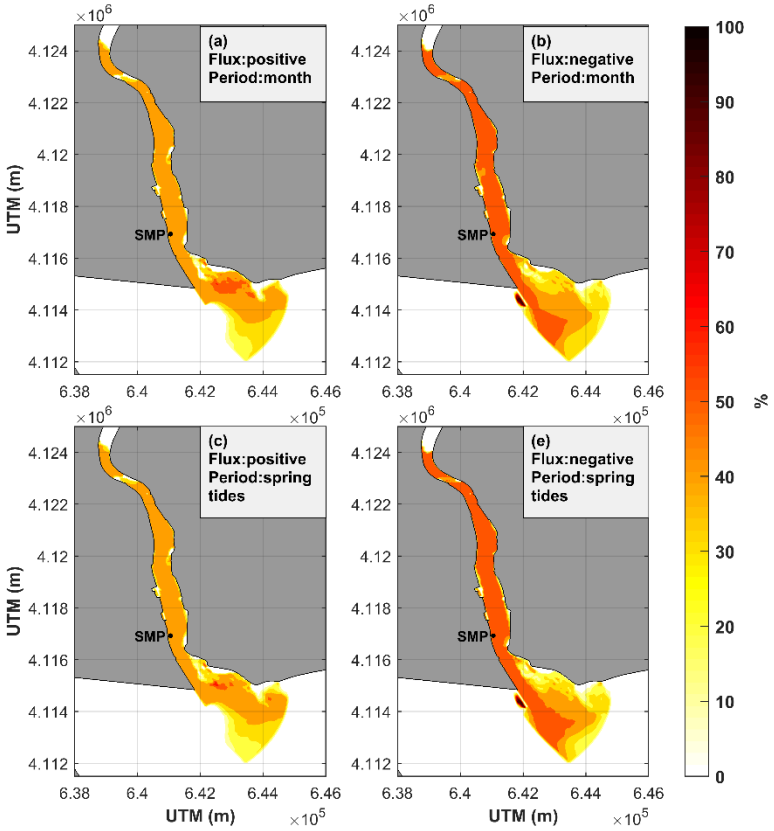

Figure 7. 6.- Time percentage during which the energy flux lays along a preferred direction (TFU). Legends at each panel indicates the direction of the flux, positive (flood tide) in the direction of 115º and negative (ebb tide) in the direction of 290º with a tolerance angle of ± θ = 30º. Color bar indicates the time percentage the flux is unidirectional.

7.3.2.4. High frequency phenomena or noise (FN).

High frequency phenomena in hydrodynamic systems contributes negatively to the mean life of the devices. These fast fluctuations of the flow are considered as noise, which is quantified as the root mean square of the high-passed series of the velocity. A Gaussian filter of $3h^{-1}$ cut-off frequency, which removes tides, was used to this aim. The root mean square, denoted as FN, is an indicator of the noise and has units of ms^{-1}.

FN is mainly present in the riversides and it is hardly detected in the central part of the channel. It shows some differences between the monthly average and the spring tide periods, when significant values of the *FN* spread wider along the riversides, and also between flood and ebb tides, being higher in the last case reaching 0.2 ms^{-1}. Although noise extends along both riversides, it is more noticeable in the west side around an existing dam located at the southern end of the mouth. Figure 7.7 shows the distribution of *FN* for ebb tide during spring tides, which is the most unfavorable situation. In the rest of situations, *FN* is negligible in practice.

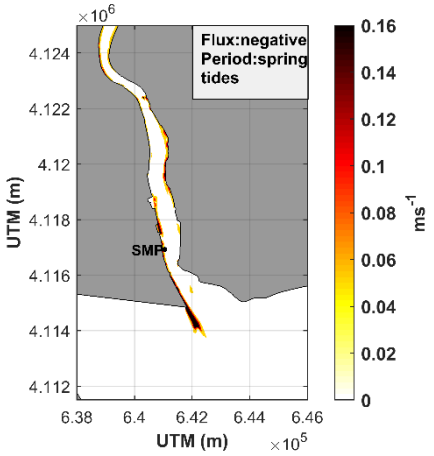

Figure 7. 7.- High frequency phenomena or noise (FN) for ebb tide during spring tide period.

7.3.2.5. Vertical shear of the flow (FS).

Forces on turbine blades immersed in water are 10 times greater than those on wind turbines. The mean life of the turbine depends on the vibrations that the rotor supports, which is accentuated under sheared flows. An indicator of the vertical shear (*FS*) has been defined as the absolute value of the mean vertical gradient of the horizontal velocity, that is, the difference between surface and the bottom layer velocities divided by the depth and averaged over time. It has units of s^{-1}.

Figure 7.8 shows the distribution of *FS* indicator for flood (panel a) and ebb (panel b) tide during spring tides, which is the period of higher detected values. For flood tide, *FS* reaches 0.12 s^{-1} at specific areas of the estuary, such as the mouth, the east riverside and from the center of the channel to the west at around 4 km upstream of SMP. For ebb tide, *FS* may reach similar peaks but with residual presence. The most remarkable fact in this case is the presence of a vertical shear of 0.06 s^{-1} extended over almost the whole lower GE, from the mouth to 6 km upstream SMP. Therefore, in this case, vertical shear can produce vibrations which must be considered in horizontal axis devices.

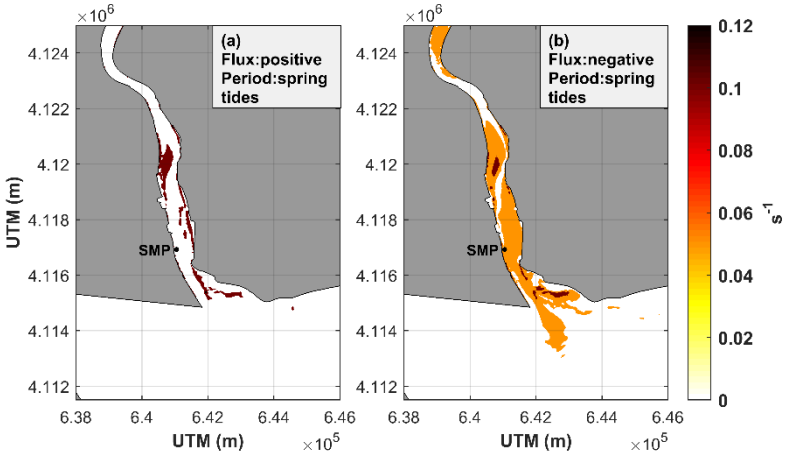

Figure 7. 8.- Vertical shear (FS) distribution for flood (panel a) and ebb (panel b) flows during spring tides.

7.3.3.- Assessment of the location of a turbine farm installation: quality function.

To diagnose the suitability of a turbine farm emplacement, a quality function, V, has been constructed. The function gathers the information of the former indicators according to their relevance. Installing a MCT farm in a place that gathers good conditions of flow permanence, unidirectionality, low noise, etc, but no intense enough flow, does not make sense. Or the contrary, selecting an area with promising strong currents but also with important levels of noise or turbulence, exposes the devices to risks that will shorten the mean life of the farm. The function V gathers the pros and cons of a given place and assesses the turbine farm profitability in terms of the amount of energy extractable and of the plausible mean life of the devices. Following the method used in (Calero Quesada et al., 2014), V is defined as:

$$V = [2X_I^2 + X_I(X_{TAT} + X_{TFP} + X_{TFU})](1 - X_{FN})(1 - X_{FS}) \qquad (7.12)$$

where X_I represents the intensity of the energy flux, E_{flux}, described in section 7.3.1.1, and the rest of parameters, X_{YYY}, are the indicators defined in section 7.3.2. The function is always positive and dimensionless. To achieve both objectives, all the indicators have been converted into dimensionless numbers according to table 7.2. The range of variation of the different indicators has been divided into intervals and a unique numerical value has been assigned to each interval. X_{TAT} varies between 0 and 3 and parameterizes the indicator *TAT*. X_{TFP} parameterizes *TFP* and takes values of 0 or 1 uniquely because of the periodic motion upstream/downstream of the flow. *TFU*, parameterized by X_{TFU}, is more restrictive than X_{TFP} for those devices that require unidirectional flow so that three

intervals have been considered and, consequently, three possible numerical values (0, 1, 2) for X_{TFU}.. For these three indicators, *TAT*, *TFP* and *TFU*, the threshold value from which they are considered to be influential is 40%. This threshold is less than the one used in the Strait of Gibraltar (Calero Quesada et al., 2014). The reason is the flood-ebb asymmetry indicated in section 7.3.2.2, with ebb tide slightly longer than flood tide. Considering a greater threshold, energy extraction during flood tide would be discarded when it can be profitable (Figure 7.9c).

Table 7. 2.- Numerical values assigned to parameters (X_{YY}, X_{YYY}) in equation (7.11). The first block is for restrictive parameters (X_I and X_{YYY}) while the second block is for no restrictive parameters (see text). Rows I, X_{YYY} and X_{YY} on each block show the numerical value associated to each interval in of the indicator range. For instance, in a place where TAT is 65%, its associated parameter X_{TAT} is 1, if it were 80%, X_{TAT} would be 2 and so on.

		VALUE			
	(X_{YYY})	*0*	*1*	*2*	*3*
Restrictive	*I (W/m^2)*	<200	[200, 500)	[500, 800)	≥ 800
	TAT (%)	< 40	[40, 75)	[75, 90)	≥ 90
	TFP (%)	< 40	≥ 40	---	---
	TFU (%)	< 40	[40, 80)	≥ 80	---
	(X_{YY})	*0*	*0.10*	*0.15*	*0.20*
Non Restrictive	*FN (m/s)*	< 0.05	[0.05, 0.15)	[0.15, 0.25)	≥ 0.25
	FS (s^{-1})	< 0.02	[0.02, 0.04)	[0.04, 0.06)	≥ 0.06

In *V*, the energy flux weights much more than the other parameters as it is the main variable. It also appears with an exponent greater than 1. Parameters X_{TAT}, X_{TFP}, and X_{TFU} are directly related to the capability of the devices for optimizing the energy extraction, so that they contribute with exponent 1. These three parameters along with X_I are called "restrictive parameters. On the other hand, parameters X_{FN} and X_{FS} are related to the mean life of the devices and are introduced in the equation with a factor between 0.8 and 1. They are called "no restrictive".

The highest value achievable for *V* is 36. The maximum value of *V* obtained in this work is above 30, similar than the obtained in the Strait of Gibraltar (Calero Quesada et al., 2014). According to *V*-values the areas have been classified as non-viable ($V < 15$), acceptable ($15 < V < 20$), recommendable ($20 < V < 25$) and very recommendable ($V > 25$).

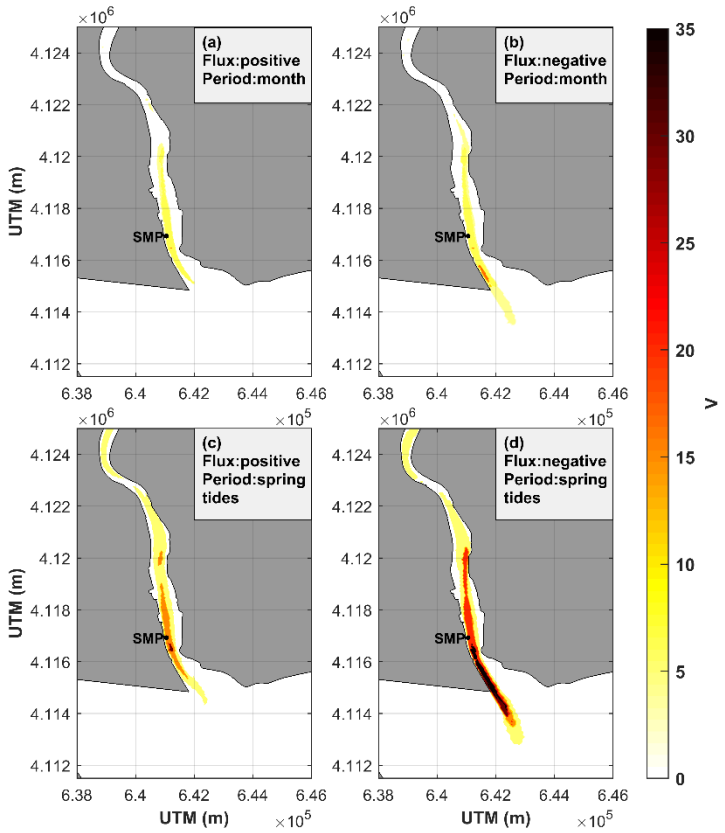

Figure 7. 9.- Distribution of quality function *V* (scale on the right). Legends in the panels provide the same information as in the previous figures.

Figure 7.9 shows the distribution of function *V* which takes values above 15 in spring tides, reaching almost 35 downstream of SMP with ebb tide. During flood tide in spring tides, the scenario is acceptable. It changes to more recommendable with ebb tide. The region of the estuary where $V > 15$ is the lower GE from 3 km upstream of SMP to a similar distance downstream of this site, and the condition is fulfilled in both flood and ebb tides. The total surface extends around 1.8 Km^2. If the spring tide periods had not been considered separately from the monthly-averaged periods and the conclusions had been derived only from the results obtained for the latter, the final inference would have been that GE is not acceptable emplacement. Therefore, it is important to consider the temporal variability of marine currents in water systems in order to analyze the suitability of a place.

7.3.4.- Estimation of the energy extraction potential of a farm.

In the most favorable scenario of spring tides during ebb tide the function *V* reaches its peak value of 35 (figure 7.9e). It allows the selection of an area bounded by this value to

install a turbine farm. As a case of study, the performance of a farm of 105 axial turbines with a diameter D=2 m that spreads over 0.36 km^2 downstream of SMP is investigated (Figure 7.3b). Other favorable morphological conditions such as a mean depth of 5 m and the fact of being located in the widest part of the estuary without preventing the marine shipping in the zone, give added value to the choice.

Figure 7.10 shows the instantaneous power output of the whole farm during a month obtained by equation (7.11) using a constant Qr = 50 m^3s^{-1}. Similar results were obtained for Qr = 10 m^3s^{-1} and Qr = 100 m^3s^{-1}.

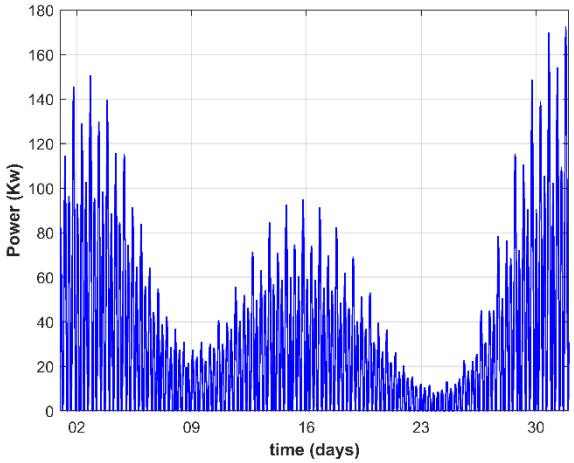

Figure 7. 10.- Modelled instantaneous power extracted from a turbine farm of 105 axial MCTs situated at the mouth of GE during a month.

The energy that can be obtained in a month, computed according to equation (7.11), is $7.5 \cdot 10^4$ MJ. Taken into account the Betz law (Thönniβen et al., 2016) which indicates that less than 16/27 (59 %) of kinetic energy can only be converted to mechanical energy using a wind turbine, the maximum extractable energy would be $4.5 \cdot 10^4$ MJ. It would be even less due to the efficiency of the devices that, for axial turbines, is around 90 % (Ahmadian and Falconer et al., 2012).

Similar values of power and energy are obtainable in the Tajo Estuary with a turbine farm of 24 MCTs of 20 m of diameter (Ceregeiro, 2019). The smaller dimensions of turbines in the GE in this case of study would be compensated by the higher number of devices. Note that this estimation of the energy extraction has been made considering the turbine farm located in the area where $V > 35$ (downstream of SMP). However, farm has not been

extended to the area where $15 < V < 25$ (upstream of SMP (Figure 7.9d)), so the energy extraction in the GE would be greater.

7.4.- Impact of the turbine farm in the tidal propagation.

The impact of the turbine farm on the tide in the GE has been evaluated by comparing tidal parameters (amplitude, phase) produced by the baroclinic hydrodynamic model with and without farm. To this aim, three different situations representing strong, average and weak tidal forcing have been defined (Figure 7.11).

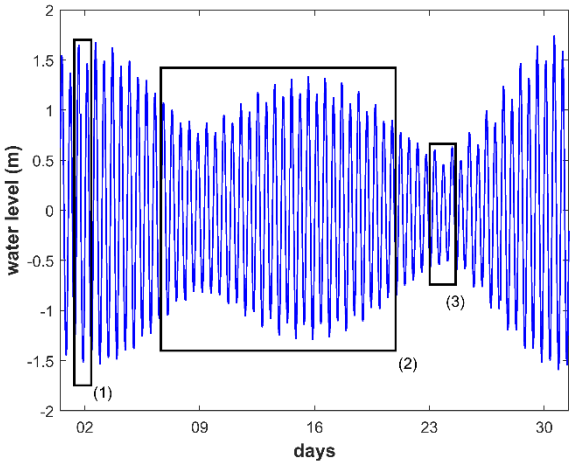

Figure 7. 11.- Water level at the initial point (after farm, 0 km) during a month indicating time periods of different tidal strength used to compare tidal amplitude of semidiurnal (STA) and quartidiurnal (QTA) species in scenarios with and without farm. Rectangle #1 shows the period of strong forcing (spring tides), rectangle #2 is for the period of "average" tides, which includes a full fortnightly cycle, and rectangle #3 is for the period of weak forcing (neap tides).

For each of the three situations, of the amplitude of the semidiurnal tide (STA, hereinafter) has been analyzed. Notice that STA does not coincide with M2 in this analysis, since for periods of strong and weak forcing (rectangles #1 and #3 in figure, respectively), the harmonic analysis returns a fictitious semidiurnal constituent that is the sum of M2 and S2 for strong forcing and the difference of M2 and S2 for weak forcing. The reason is the very short length of the series (2 or 3 days, respectively) used to estimate the harmonic constants, which does not allow for separating M2 and S2 constituents. This is not the case of the "average" tide, whose length is enough to accomplish such separation. In this case, STA tends to be close to the actual value of M2 amplitude. For this reason the term STA is used instead of M2.

In the other hand, quartidiurnal contribution (QTA) is analyzed as a proxy of the friction in the estuary (remind that the main constituent of this species, M4, is not prescribed in the open-ocean boundary). For the same reasons as before, the term QTA is preferred the M4 in order to describe friction since quartidiurnal species contain many other non-lineal constituents.

The analysis has been made for different Qr, namely, 10, 50 and 100 m^3s^{-1}, which embraces the typical discharges in the GE (Fortunato et al., 2002). Figure 7.12 shows the results of the analysis. The division in three zones suggested by the different slopes of STA and QTA amplitudes (Zone I, Zone II and Zone III) and carried out in (Calero Quesada et al., 2019) has been maintained. The origin (km 0 in Figure 7.12) is situated near SMP (Figure 7.2). Zone I spreads over the first 20 km and holds the turbine farm, Zone II over the next 40 km and, finally, Zone III extends from km 60 to the estuary's head. Zone I is identified with the zone of clear influence of the tide, Zone II is identified with an intertidal zone where balance between tidal forcing and Qr occurs, whereas in Zone III, Qr prevails (Calero Quesada et al., 2019).

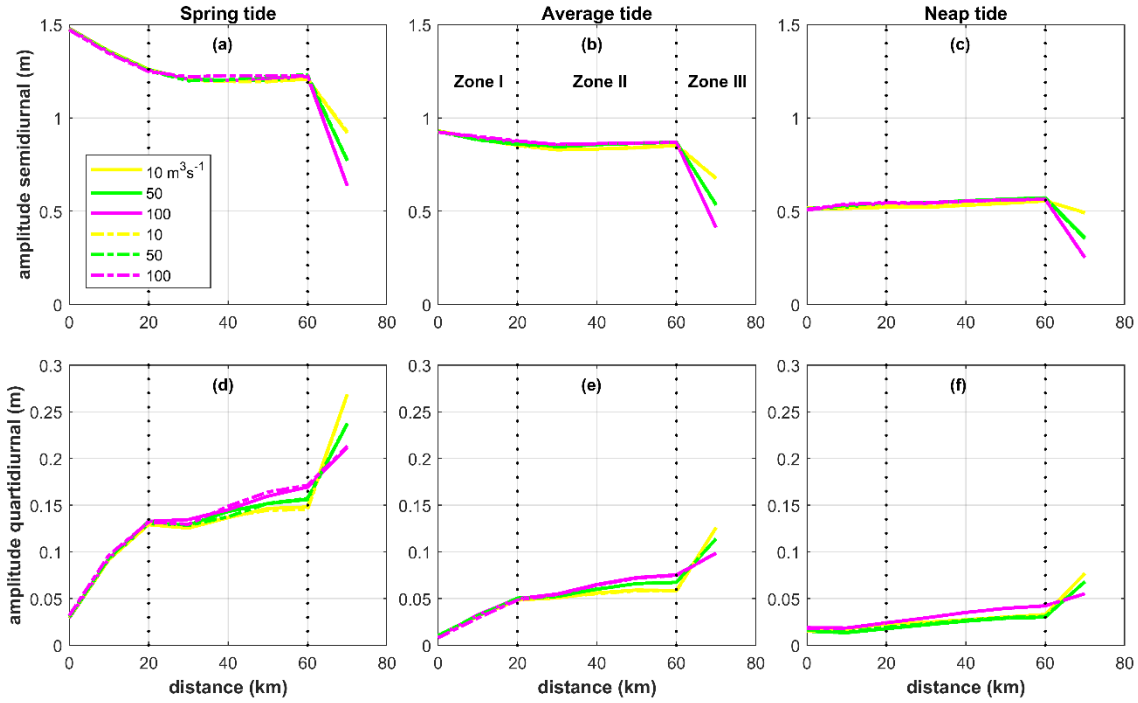

Figure 7. 12.- Semidiurnal tidal amplitude (STA) along the estuary in spring, average (fortnightly cycle) and neap tides (panels a, b and c, respectively), and quartidiurnal component (QTA) during the same time periods (panels d, e and f). Solid (dashed) lines indicate amplitudes without (with) the turbine farm Different Qr's of 10, 50 and 100 m^3s^{-1} have been used (see color code in the legend of panel a). Vertical dotted lines show the division ofthe estuary in the three zones mentioned in the text (see panel b).

Figure 7.12 does not show significant differences when the farm is installed. There are small variations in Zone I nearby the farm and further upstream in Zone II, which are not well appreciated in the figure. The changes would be associated to the slight weakening of the tidal forcing beyond the farm and also to the acceleration due to the edge of the turbines (Bryden and Couch 2005). A possible cause for this small discrepancy could be a modification of the balance between acceleration due to the convergence of the flow in the estuary and the deceleration due to friction with the bottom and the turbines them shelves. A greater discrepancy between STA and QTA amplitudes is observed in spring tides when Qr is large. For Qr=100 m^3s^{-1}, its influence in the balance of forces along the estuary reaches even the mouth.

The rising-falling asymmetry, that is, the difference between the duration of the rising and falling semi-cycles, has been also investigated. Figure 7.13 shows the duration of the falling cycle (the rising one is the tidal period (12.42 h) minus the falling one and its plot is redundant) in spring and neap tides.

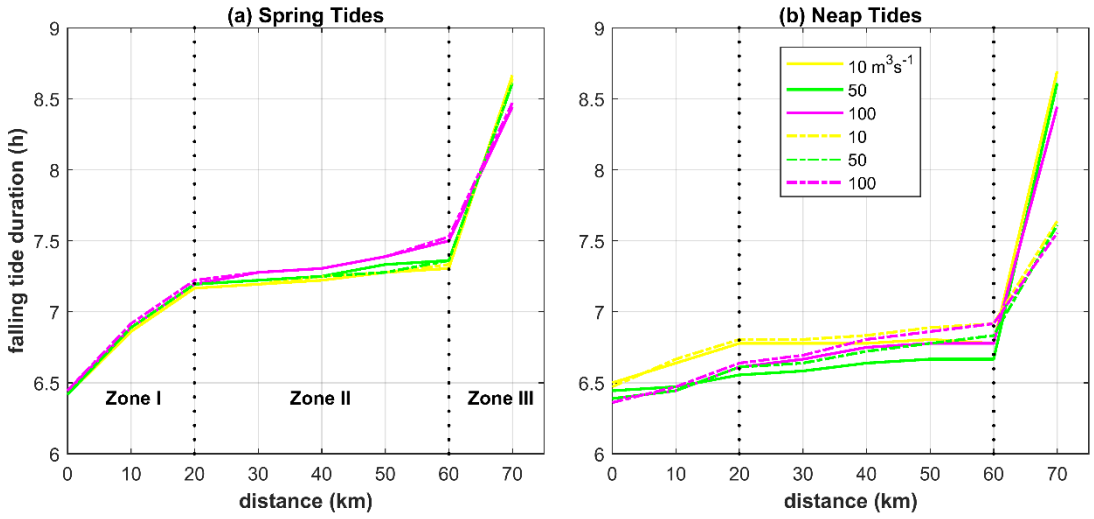

Figure 7. 13.- Falling tide duration in spring (panel a) and neap tides (panel b) for the different Qr indicated in the legend of panel b. Duration without and with the turbine farm are indicated by solid and dashed lines, respectively.

The duration of the falling tide is less modified in spring tides than in neap tides. In Zone I in spring tides, solid and dashed lines differ less than 2 min, in most of Zone II, both lines runs very near one to the other, even matching each other; it is not until the end of the Zone that they separate a little bit, especially for Qr = 50 m^3s^{-1}, which shows a difference of 5 min at km 50, the duration being shorter with the turbine farm. In Zone

III, the duration is similar with and without the farm. In neap tides, the falling tide is shorter with the turbine farm at the beginning of Zone I. Upstream, the lines of the same color intersect and this tendency is reversed. In Zone II, differences up to 10 min are observed, being shorter without turbines. In Zone III, dashed lines move away from solid ones even more, changing the pattern and diminishing the duration in presence of the turbine farm, which reaches a maximum of 1 h at the end of the Zone III. The behavior is similar for the different Qr.

The pattern that apparently emerges is that tidal forcing in spring tides is strong enough that the presence of the turbine farm does not modify the duration of the falling tide along the estuary substantially (Figure 7.13a). That is, in this zone where there is higher influence of Qr, with a weaker tidal forcing, the resulted effect is to short the falling tide half cycle. In the intermediate zone where is a balance between tidal forcing and Qr, as indicated by an almost null slope of the solid line, the weakening of tidal signal with the presence of turbine farm has as a result a lengthening in duration of falling tide half cycle.

7.5.- Conclusions

A method based on indicators has been used to define a quality function that allows to locate the most interesting areas for energy extraction in the meso-tidal estuary of the Guadiana River. The method was used before in another system, the Strait of Gibraltar (Calero Quesada et al., 2014) successfully. The most intense currents with associated energy fluxes of 900 Wm^{-2} (and peak values of 1200 Wm^{-2}) are localized in the lower part of the estuary, near the mouth, during spring tides for the ebb tidal flow, as it could be expected. The quality function allows to delimit the most propitious area for installing a turbine farm, not only regarding the energy flux but also other characteristics of the flow such as permanence of the flow in a direction, unidirectionality, vertical shear and high frequency phenomena (noise). All of them were integrated in the defined empiric quality function (equation (7.12)), which gives a numerical output useful to select the most suitable area. The method can be exported to other similar or larger estuaries.

Once the best area for energy extraction was delimited, the energy production of a farm of axial axes turbines (105 turbines in the case studied) s has been simulated. For this, a module was implemented in MOHID model which represents the turbine as a momentum sink to add a reaction force to the hydrodynamic model. The instantaneous power and the

theoretical energy provided by the turbine farm have been evaluated. A mean power of 29 KW and a monthly energy of $7.5 \cdot 10^4$ MJ have been obtained.

Turbine farm does not impact significantly in the tidal propagation within the estuary, as deduced from the study of the amplitude variation of semidiurnal components of the tide (the prevailing species) when the farm is incorporated into the model. Small variations of certain parameters (the duration of the falling/rising tides as well as the amplitude at some stretches of the estuary) are hardly detected in our analysis. They are a little more obvious under neap tides. We speculate that changes in the balance between convergence and friction might be behind the discrepancies.

Acknowledgments

M.C. Calero-Quesada acknowledges the pre-doc fellowship of Campus de Excelencia Internacional del Mar (Plan ReSEArch Agregación-CEIMAR: 18INAC0284). Also to the High Technical Institute of the University of Lisbon for a stay during summer of 2019 and the University of Malaga for support this stay.

Apendix 7.A. Annex 7.I

7.A.1. Tidal Harmonic Constituents introduced in the open boundary in MOHID system.

Table 7.A1.- Harmonic constants of the main constituents used to reconstruct the tidal signal on the continental shelf open boundary. The constants have been obtained from the global tide- model FES2004. Only harmonic constants with amplitudes>1 cm are listed in the table, although the model includes some more with amplitude below this threshold. M4 is intentionally included, despite its zero amplitude, in order to emphasis the fact that this shallow water constituent of non-linear origin is null at the boundary but it is locally generated in the estuary by the model.

Constituent	Amplitude (m)	Phase (degrees)
M2	1.02	57
S2	0.40	83
K1	0.07	49
K2	0.10	76
N2	0.22	40
2 N2	0.03	19
O1	0.06	311
Q1	0.02	48
P1	0.02	262
M4	0	-

8.- PRINCIPALES RESULTADOS Y CONCLUSIONES

En este capítulo enumeramos los principales resultados y conclusiones extraídos de los capítulos 5, 6 y 7:

1. Se ha propuesto un método basado en indicadores que permita encontrar las zonas más viables de un sistema hidrodinámico para la instalación de una granja de turbinas. Una función empírica, llamada función de calidad, V, reúne toda la información aportada por esos indicadores proporcionando un valor numérico a partir del cual clasificar la viabilidad de una zona.

2. Este método ha sido aplicado a dos sistemas hidrodinámicos diferentes, el SG y el GE, situados al sur de la Península Ibérica, caracterizados por presentar corrientes intensas. El análisis de las corrientes se ha realizado aplicando un modelo hidrodinámico diferente en cada escenario, el que mejor se adapta a las características de cada sistema. Se trata de los modelos hidrodinámicos del MITgcm para el SG y el Mohid para el GE. En ambos casos el método ha resultado ser satisfactorio.

3. En el SG se ha encontrado que las corrientes más intensas tienen lugar en la capa superficial sobre el Umbral de Camarinal y desde aquí hacia la parte oriental del estrecho, a profundidades intermedias sobre el área del Umbral de Camarinal y en profundidad sobre el área de Umbral de Espartel, donde los flujos llegan a superar los 1.8 kWm^{-2}. Al considerar el resto de indicadores, el área más superficial y las intermedias quedan más comprometidas dejando al área en profundidad entorno a Umbral de Espartel como la más viable, con el mayor valor de V.

4. En el Estuario del Guadiana se ha encontrado que la mejor zona es la parte baja del estuario para marea vaciante durante el periodo de mareas vivas donde el flujo en promedio puede llegar a los 1.2 kWm^{-2} y la función de calidad V toma valores similares a los del SG.

5. Se ha simulado una granja de turbinas de eje axial en la zona más viable del GE y se ha obtenido que la potencia instantánea media es de 29 kW al mes y la energía extraída en ese periodo es de $7.5 \cdot 10^4$ MJ.

6. Se ha estudiado la hidrodinámica en el GE dada la importancia de conocer el emplazamiento para la instalación de una granja de turbinas. Además, los estuarios son sistemas hidrodinámicos muy sensibles a cualquier tipo de cambio. El estudio se realizó en 2D bajo diferentes forzamientos de mareas y de Qr para explorar el efecto de la propagación de la onda de marea.

7. Un estudio similar ha permitido la comparación del comportamiento de la onda de marea en presencia y en ausencia de la granja de turbinas. El resultado es que la granja tiene un efecto poco significativo en la propagación de la onda de marea y los cambios producidos aparecen a continuación de la granja y a largas distancias.

AGRADECIMIENTOS

En primer lugar deseo expresar mi agradecimiento a mis directores de tesis, el catedrático Jesús García Lafuente y el doctor Javier Delgado Cabello, por su paciencia y apoyo en este trabajo así como el respeto a mis comentarios y por la dirección y el rigor a las mismas. Sin su ayuda no habría podido desarrollar esta tesis y tengo mucho que agradecerles, me han guiado en el camino y me han facilitado los medios para conseguirlo.

Igualmente me gustaría agradecer a mis compañeros del grupo GOFIMA que hayan remado a mi lado, me hayan dedicado parte de su tiempo y su amistad, llegando a ser una familia para mí. Ellos son Francisco Criado Aldeanueva, José Carlos Sánchez Garrido, Cristina Naranjo Rosa, Simone Sammartino, Javier Soto Navarro.

A su vez, agradecer a otros compañeros fuera del grupo GOFIMA que he conocido durante este tiempo y que de algún modo me han prestado su ayuda con sus aportaciones. Me refiero sin duda a Erwan Garel, Flávio Martins, al resto del grupo CIMA de la Universidad del Algarve y a Francisco Campuzano, del Instituto Superior Técnico de Lisboa. Por supuesto, también, a la Universidad de Málaga por haberme prestado soporte económico y de la que me he sentido orgullosa de formar parte.

Igualmente otros compañeros que han formado parte de este maravilloso equipo de Gofima como Juan Moreno Navas. También personas de dentro y fuera del mundo académico, a las que tendría mucho que agradecer, algunas ya no están, y al resto que no he incluido, espero que me disculpen… ha sido un camino largo.

Financiación

Esta tesis doctoral comenzó su andadura bajo la financiación del proyecto titulado *'Propuesta metodológica para diagnosticar y pronosticar las consecuencias de las actuaciones humanas en el estuario del Guadalquivir'* desarrollado por la Autoridad Portuaria de Sevilla y el Consejo Superior de Investigaciones Científicas (CSIC). El trabajo siguió desarrollándose al completo bajo el Proyecto de Excelencia RNM-3738 financiado por la Junta de Andalucía. También se agradece el apoyo parcial de CTM2010-21229-C02 del Ministerio de Economía español y CTM-2008-04150E de las actividades

europeas de MarinERA y la concesión de un contrato predoctoral del Campus de Excelencia Internacional del Mar (CEIMAR) (Plan ReSEArch Agregación-CEIMAR: 18INAC0284). Así mismo se agradece el apoyo económico al Ministerio de Ciencia, Tecnología e Innovación por la dotación económica para la realización de una estancia de 3 meses en el Centro de Investigación Marina y Ambiental (CIMA) perteneciente a la Universidad del Algarve en Faro (Portugal). Posteriormente, otra estancia de 1 mes en el mismo centro financiado por CEIMAR. Por último, a la Universidad de Málaga por la financiación para una estancia de 15 días en el Instituto Superior Técnico (IST) de Lisboa (Portugal).

9.- REFERENCIAS

(CSIRO), C. S. (2012). *Ocean renewable energy: 2015–2050. An analysis of ocean energy in Australia.*

Abreu , A. L. (2010). *Avaliação do potencial energético das marés no Estuário do Rio Douro.* Porto (Portugal): PhD. Faculdade de Engenharia do Porto .

Ahmadian, R., & Falconer, R. A. (2012). Assessment of array shape of tidal stream turbines on hydro-environmental impacts and available power . *Renew.Energy, 44*, 318-327. doi: http://dx.doi.org/10.1016/j.renene.2012.01.106

Amelio, M., Barbarelli, S., Florio , G., Scornaienchi, M., Minniti, G., & Cutrupi, A. (2012). Innovative tidal turbine with central deflector for the exploitation of river and sea currents in on-shore installations. *Appl Energy, 97*, 944-55. doi:http://dx.doi.org/10.1016/j.apenergy.2011.11.044

Armi, L., & Farmer, D. M. (1985). The internal hydraulics of the Strait of Gibraltar and associated sills and narrows. *Oceanol. Acta , 8*, 37–46.

Armi, L., & Farmer, D. M. (1988). The flux of the Mediterranean water through the Strait of Gibraltar. *Prog Oceanogr, 21*, 1-105.

Ascione Kenov, I., Garcia, A. C., & Neves, R. (2012). Residence time of water in the Mondego estuary (Portugal) . *Estuarine, Coastal and Shelf Science, 106*, 13-22. doi: https://doi.org/10.1016/j.ecss.2012.04.008.

Bahaj, A. S. (2011). Generating electricity from the oceans. *Renew Sustain Energy Rev, 15*, 3399–416. doi:http://dx.doi.org/10.1016/j.rser.2011.04.032

Bahaj, A. S., Molland, A. F., Chaplin, J. R., & Batten, W. M. (2007). Power and thrust measurements of marine current turbines under various hydrodynamic flow conditions in a cavitation tunnel and a towing tank. *Renewable Energy, 32*, 407-426. doi:doi.org/10.1016/j.renene.2006.01.012.

Balsells Badia, O. (2017). *Implementation of the effect of turbines on water currents in MOHID Modelling System .* Lisboa, Portugal: (Master Thesis) Instituto Superior Tecnico.

Basos, N. (2013). *GIS as a Tool to Aid Pre- and Post-Processing of Hydrodinamic Models. Aplication to the Guadiana Estuary.* Faro, Portugal: PhD. Univesity of Algarve. Obtenido de http://refhub.elsevier.com/S1385-1101(17)30322-2/rf0005

Bedard, R., Jacobson , P. T., Previsic, M., Musial, W., & Varley, R. (2010). An overview of ocean renewable energy technologies. *Oceanography, 23 (2)*, 22-31. doi:http://dx.doi.org/10.5670/oceanog.2010.40

Blumberg , A. F., Kim, B. N., & O'Neil, S. (March de 2000). Use of orthogonal curvilinear grids for the represetnation of the litorl ocean environment. *Proceedings of Spring 2000 Simulation Interoperability Workshop*, 00S-SIW-118. Obtenido de http://refhub.elsevier.com/S1385-1101(17)30322-2/rf0010

Braunschweig , F., Fernandes, L., Galvao, P., Trancoso, R., Pina, P., & Neves, R. (2005). Mohid GIS - A geogrpaphical information system for water modelling software. (E. Meeting,

Ed.) *Geophysical Research Abstracts*, 05-A-08213. Obtenido de http://refhub.elsevier.com/S1385-1101(17)30322-2/rf0020

Braunschweig, F., Leitao, P. C., Fernandes, L., Pina, P., & Neves, R. (2004). The object oriented design of the integrated waer modelling system MOHID. *Dev. Water Sci., 55(2)*, 1079-1090. Obtenido de http://refhub.elsevier.com/S1385-1101(17)30322-2/rf0015

Brito, E., & Melo, A. (2016). *Annual report 2016. Implementing Agreement on ocean energy systems. IEA-OES.* . Villaje JL.

Bruno, M., Alonso, J. J., Cózar , A., Vidal, J., Ruíz Cañavete, A., & Echevarria, F. (2002). The boiling water phenomena at Camarinall Sill, the Strait of Gibraltar. *Deep Sea Res II, 49*, 4097–113.

Bryden, H. L., & Kinder, T. (1991). Steady two-layer exchange through the Strait of Gibraltar. *Deep Sea Res, 38(S1)*, S445–63.

Bryden, I. G., & Couch, S. J. (2005). .ME1 – marine energy extraction: tidal resource analysis. *Renewable Energy, 31*, 133–139. doi:10.1016/j.renene.2005.08.012.

Bryden, I. G., Bullen, C., Baine, M., & Paish, O. (1995). Generating electricity from tidal currents in orkney and shetland. *Underwater Technology*, 21-22.

Burman, K., & Walker, A. (s.f.). *Ocean energy technology overview: federal energy management program (FEMP).* doi:http://dx.doi.org/10.2172/962501

Cai, H., Savenije, H. G., & Jiang, C. (2014). Analytical approach for predicting fresh water discharge in an estuary based on tidal water observations. *Hydrology and Earth System Sciences, 18*, 4153–4168. doi:10.5194/hess-18-4153-2014

Cai, H., Savenije, H. G., & Toffolon, M. (2013). Linking the river to the estuary: influence of river discharge on tidal damping. *Hydrology and Earth System Sciences, 10*, 9191-9238. doi:10.5194/hessd-10-9191-2013

Cai, H., Savenije, H. G., Yang, Q., & Ou, S. (2012). Influence of the river discharge and dredging on tidal wave propagation: Modaomen estuary case. *Journal of Hydraulic Engineering, 138 (10)*, 885-896. doi:10.1061/(ASCE)HY.1943-7900.0000594

Calero Quesada, M. C., García-Lafuente, J., Garel, E., Delgado-Cabello, J., Martins, F., & Moreno-Navas, J. (2019). Effects of tidal and river discharge forcings on tidal propagation along the Guadiana Estuary. *Sea Research J., 146*, 1-13. doi:https://doi.org/10.1016/j.seares.2019.01.006

Calero Quesada, M. C., García-Lafuente, J., Sánchez Garrido, J. C., Sammartino, S., & Delgado-Cabello, J. (2014). Energy of marine currents in the Strait of Gibraltar and its potential as a renewable energy resource. *Renew Sustain Energy Rev, 34*, 98-109. doi:http://dx.doi.org/10.1016/j.rser.2014.02.038

Cancino, L., & Neves, R. (1999). Hydrodynamic and sediment suspension modelling in estuarine systems. Part II: Application to the Western Scheldt and Gironde estuaries . *Journal of Marine Systems, 22*, 117-131.

Candela, J., Winant , C., & Bryden, H. L. (1989). Meteorologically forced subinertial flows through the Strait of Gibraltar. *J Geophys Res, 94*, 12667–74.

Candela, J., Winant, C., & Ruíz, J. (1990). Tides in the Strait of Gibraltar. *J Geophys Res, 95*, 7313–35.

Carballo, R., Iglesias, G., & Castro, A. (2009). Numerical model evaluation of tidal stream energy resources in the Ría de Muros (NW Spain). *Renewable Energy, 34*, 1517-1524. doi:10.1016/j.renene.2008.10.028.

Carter, G. S., & Marriefield , M. A. (2007). Open boundary conditions for regional tidal simulations. *Ocean Model, 18*, 194–209.

Castro-Santos, L., Prado García, G., Estanqueiro, A., & Justino, P. (2015). The Levelized Cost of Energy (LCOE) of Wave Energy Using GIS Based Analysis: The Case Study of Portugal. *International Journal of Electrical Power & Energy Systems, 65*, 21-25.

Ceregeiro, J. (2019). *Tidal Farm Electric Energy Production in the Tagus River.* Lisboa (Portugal): PhD. Universidade de Lisboa.

Chícharo, L., Chícharo, M. A., Esteves, E., Andrade, P., & Morais, P. (2002). Effects of alterations in fresh water supply on the abundance and distribution of Engraulis encrasicolus in the Guadiana Estuary and adjacent coastal areas of south Portugal 1,. *Journal Ecohydrology and Hydrobiology, 1*, 195-200.

Chícharo, M. A., Chícharo, L., & Morais, P. (2006). Interannual differences of ichthyofauna structure of the Guadiana estuary and adjacent coastal area (SE Portugal/SW Spain): before and after Alqueva dam construction . *Estuarine, Coastal and Shelf Science, 70*, 39-51.

De Falcao, A. (2010). Wave energy utilization: a review of technologies. *Renew Sustain Energy Rev, 14*, 899–918. doi:http://dx.doi.org/10.1016/j.rser.2009.11.003

Delgado , J., García-Lafuente, J., & Vargas, J. M. (2001). A simple model for submaximal exchange through the Strait of Gibraltar . *Sci Mar, 65(4)*, 313–22.

Dias, J. M., González, R., & Ferreira, Ó. (2004). Natural Versus Anthropic Causes in Variations of Sand Export for River Basins: An Example from the Guadiana River Mouth (Southwestern Iberia). Rapid Transgression into Semi-enclosed Basins. *Polish Geological Institute Special Papers*, 95-102. Obtenido de http://refhub.elsevier.com/S1385-1101(17)30322-2/rf0045

Díez-Minguito, M., Baquerizo, A., Ortega-Sánchez, M., Navarro, G., & Losada, M. A. (2012). Tide transformation in the Guadalquivir estuary (SW Spain) and process-based zonation. *Journal of Geophysical Research,, 117, C03019*. doi:10.1029/2011JC007344

Drew, B., Plummer, A. R., & Sahinkaya, M. N. (2009). A review of wave energy converter technology. Proc Inst Mech Eng Part A. *J Power Energy*, 223:887. doi:http://dx.doi.org/10.1243/09576509JPE782

Dyer, K. R. (1997). *Estuaries: A Pysical Introduction.* (J. Wiley, Ed.) Avon. Obtenido de http://refhub.elsevier.com/S1385-1101(17)30322-2/rf0050

EMEC. (2013). *Assessment of Tidal Energy Resource - Marine Renewable Energy Guides. European Marine Energy Centre Ltd*. Obtenido de http://www.emec.org.uk/assessment-of-tidal-energy-resource/

Erzini, K. (2005). Trends in NE Atlantic landings (southern Portugal): identifying the relative importance of fisheries and environmental variables. *Fisheries Oceanography, 14*, 195-209.

EU. (May de 2014). *Blue Energy Action Needed to Deliver on the Potential of Ocean Energy in European Seas and Oceans by 2020 and Beyond*. Obtenido de http://eur-lex.europa.eu/legal-content/EN/TXT/?qid=1396419828231&uri=CELEX:52014DC0008

Eurostat. (Junio de 2020). *https://ec.europa.eu/eurostat/statistics-explained/*. Obtenido de https://ec.europa.eu/eurostat/statistics-explained/: https://ec.europa.eu/eurostat/statistics-explained/index.php?title=Energy_production_and_imports/es&oldid=508592#Tanto_la_UE_como_sus_Estados_miembros_son_importadores_netos_de_energ.C3.ADa

Farmer, D. M., & Armi, L. (1986). Maximal two-layer exchange over a sill and through the combination of a sill and contraction with barotropic flow. *J Fluid Mech, 164*, 53–76.

Ferreira, A. M., Martins, M., & Vale, C. (2003). Influence of diffuse sources on levels and distribution of polychlorinated biphenyls in the Guadiana river estuary, Portugal . *Mar. Chem, 83*, 175-184.

Fortunato, A. B., & Oliveira, A. (2000). On the representation of bathymetry by unstructured grids . En L.R. Bentley et al., *Computational Methods in Water Resources XIII* (Vol. 2, págs. 889-896). .

Fortunato, A. B., Oliveira, A., & Alves , E. T. (2002). Circulation and salinity intrusion in the Guadiana Estuary. *Thalassas, 18(2)*, 43-65. Obtenido de http://refhub.elsevier.com/S1385-1101(17)30322-2/rf0070

Friederichs, C., & Aubrey, D. (1994). Tidal propagation in strongly convergent channels. *J. Geophys. Res., 99*, 3321-3336. Obtenido de http://refhub.elsevier.com/S1385-1101(17)30322-2/rf0080

Friedrichs, C. T. (2010). Barotropic Tides in Channelized Estuaries . En A. Levinson, *Contemporary Issues in Estuarine Physics.* Cambridge.

Frost, C., Findlay, D., Macpherson, E., Sayer, P., & Johanning, L. (2018). A Model to Map Levelised Cost of Energy for Wave Energy Projects. *Ocean Engineering, 149*, 438–451.

Funke, S. W., Farrel, P. E., & Piggott, M. D. (2014). Tidal turbine array optimization using the adjoint approach . *Renew Energy, 63*, 658–73. doi:http://dx.doi.org/10.1016/j.renene.2013.09.031

García-Lafuente, J., & Criado-Aldeanueva, F. (2001). *Física de la Tierra. Oceanografía Física: su investigación en España* (Vol. 13).

García-Lafuente, J., Álvarez Fanjul, E., Vargas, J. M., & Ratsimandresy , A. W. (2002). Subinertial variability in the flow through the Strait of Gibraltar . *J Geophys Res, 107 (C10)*, 3168. doi: http://dx.doi.org/10.1029/2001JC001104.

García-Lafuente, J., Bruque Pozas, E., Sánchez Garrido, J. C., Sannino, G., & Sammartino, S. (2013). The interface mixing layer and the tidal dynamics at the eastern part of the Strait of Gibraltar. *J Mar Syst , 0924-7963 117–118*, 31-42.

García-Lafuente, J., Delgado Cabello, J., & Criado Aldeanueva, F. (2002b). Inflow interruption by meteorological forcing in the Strait of Gibraltar . *Geophys Res Lett*, 29:19.

García-Lafuente, J., Sammartino, S., Huertas, E. I., Flecha, S., Sánchez Leal, R. F., Naranjo, C., . . . Bellanco, M. J. (2021). Hotter and Weaker Mediterranean Outflow as a Response to Basin-Wide Alterations. *Frontiers in Marine Science, 8*, 150. doi:DOI=10.3389/fmars.2021.613444

García-Lafuente, J., Vargas, J. M., Plaza, F., Sarhan, T., Bascheck , B., & Candela, J. (2000). Tide at the eastern section of the Strait of Gibraltar. *J Geophys Res, 105*, 14197–213.

García-Oliva, M., Djordjevic, S., & Gabin, R. T. (2017). The influence of channel geometry on tidal energy extraction in estuaries. *Renewable Energy, 101*, 514-525. doi:http://dx.doi.org/10.1016/j.renene.2016.09.009

Garel , E., Pinto, L., Santos, A., & Ferreira, Ó. (2009a). Tidal and river discharge forcing upon water and sediment circulation at a rock-bound estuary (Guadiana estuary, Portugal). *Estuar. Coast. Shelf Sci, 84*, 269–281. doi:https://doi.org/10.1016/j.ecss.2009.07.002

Garel, E. (2017). Present dynamics of the Guadiana estuary. En D. Moura, A. Gomes, I. Mendes, J. Anibal, & U. o. Algarve (Ed.), *Guadiana River Estuary - Investigating the Past, Present and Future* (1 ed., págs. 15-37). Faro. Obtenido de http://hdl.handle.net/10400.1/9887

Garel, E. (2017a). Present dynamics of the Guadiana estuary , Guadiana River Estuary - Investigating the Past, Present and Future. En D. G. Moura (Ed.). Faro, Portugal: 1st Edition. University of Algarve. Obtenido de ISBN 978-989-8859- 18-1. http://hdl.handle.net/10400.1/9887.

Garel, E. (2017b). Collection and dissemination of data from environmental monitoring systems in estuaries. *Proceeding of 4th Experiment@International Conference.* Faro (Portugal): IEEE.

Garel, E., & Cai, H. (2018). Effects of tidal-forcing variations on tidal properties along a narrow convergent estuary. *Estuar. Coasts*. doi:https://doi.org/10.1007/s12237-018-0410-y

Garel, E., & D'Alimonte, D. (2017). Continuous river discharge monitoring with bottom-mounted current profilers at narrow tidal estuaries . *Cont. Shelf Res., 133*, 1-12. doi:https://doi.org/10.1016/j.csr.2016.12.001

Garel, E., & Ferreira, O. (2011a). Monitoring estuaries using non-permanent stations: practical aspects and data examples. *Ocean Dyn, 61*, 891–902. doi:https://doi.org/10.1007/s10236-011-0417-4

Garel, E., & Ferreira, O. (2011b). Effects of the Alqueva Dam on sediment fluxes at the mouth of the Guadiana Estuary. *Journal of Coastal Research, 64*, 1505-1509.

Garel, E., & Ferreira, Ó. (2013). Fortnightly changes in water transport direction across the mouth of a narrow estuary. *Estuar. Coasts, 36*, 286–299. doi:https://doi.org/10.1007/s12237-0.12- 9566-z

Garel, E., & Ferreira, O. (2013). Fortnightly Changes in Water Transport Direction Across the Mouth of a Narrow Estuary . *Estuaries and Coasts, 36*, 286-299. doi:DOI: 10.1007/s12237-0.12-9566-z

Garel, E., & Ferreira, O. (2015). Multi-year high-frequency physical and environmental observations at the Guadiana estuary . *Earth System Science, Data 7*, 299–309. doi:https://doi.org/10.5194/essd-7-299-2015

Garel, E., Nunes, S., Magalhaes-Neto, J., Fernandes, R., Neves, R., Marques, J. C., & Ferreira, O. (2009b). The autonomous Simpatico system for real-time continuous water-quality and current velocity monitoring: examples of application in three Portuguese estuaries. *Geo-Mar. Lett., 29*, 331–341. doi: https://doi.org/10.1007/s00367-009-0147-5

Goude , A., & Agren, O. (2014). Simulations of a vertical axis turbine in a channel. *Renew. Energy, 63*, 477–85. doi:http://dx.doi.org/10.1016/j.renene.2013.09.038

Goundar , J. N., & Raffiuddein, A. M. (2013b). Design of a horizontal axis tidal current turbine. *Appl Energy, 111*, 161–74. doi:http://dx.doi.org/10.1016/j.apenergy.2013.04.064

Goundar, J., & Raffiudein , A. (2013a). Marine current energy resource assessment and. *Renew Energy*, 1-9. doi:http://dx.doi.org/10.1016/j.renene.2013.06.036

Grogan, D. M., Leen, S. B., Kennedy, C. R., & Ó'Brádaigh, C. M. (2013). Design of composite tidal turbine blades. *Renew Energy, 57*, 151–62. doi:http://dx.doi.org/10.1016/j.renene.2013.01.021

Hanson, H. P., Bozek, A., & Duerr, A. E. (2011). The Florida current: a clean but challenging energy resource . *EOS Trans Am Geophys Union, 92*, 29–36. doi:http://dx.doi.org/10.1029/2011EO040001.

Hanson, H. P., Skemp, S. H., Alsenas, G. M., & Coley, C. E. (2010). Power from the Florida current. A new perspective on an old vision. *Am Meteorol Soc 2010*. doi:http://dx.doi.org/10.1175/2010BAMS3021.1

Hass, K. A., Fritz, H. M., French, S. P., Smith, B. T., & Neary, V. (2011). *Assessment of Energy Production Potential from Tidal Streams in the United States.* United States N. p., 2011. doi:10.2172/1219367

http://www.tidalstreampower.gatech.edu/. (s.f.). Obtenido de http://www.tidalstreampower.gatech.edu/.

IRENA. (2014). *http://www.irena.org/DocumentDownloads/Publications/Tidal_Energy_V4_WEB.pdf,.*

Jay, D. A. (1991). Green's law revisited: tidal long-way propagation in channels with strong topogrphy. *J. Geophys. Res., 96 (C11)*, 585 20. Obtenido de http://refhub.elsevier.com/S1385-1101(17)30322-2/rf0130

Jo Chul, h., Yim Jin , y., Lee Kang , h., & Rho Yu , h. (2012). Performance of horizontal axis tidal current turbine by blade configuration. *Renew Energy, 42*, 195–206. doi:http://dx.doi.org/10.1016/j.renene.2011.08.017.

Kevin, A. H., Fritz, M. H., French, S. P., Smith, B. T., & Neary, V. (2011). Assessment of energy production potential from tidal stream in the United States [Final project report]. *Georgia Research Corporation (, DE-FG36-08G018174*.

Khan, M. J., Bhuyan, G., Iqbal, M. T., & Quaicoe, J. E. (2009). Hydrokinetic energy conversion system and assessment of horizontal and vertical axis turbines for river and tidal applications: a technology status review. *Appl Energy, 86*, 1823–35. doi:http://dx.doi.org/10.1016/j.apenergy.2009.02.017

Lanzoni, S., & Seminara, G. (1998). On tide propagation in covergent estuaries. *J. Geophys. Res., 103 (C3)*, 30, 793. Obtenido de http://refhub.elsevier.com/S1385-1101(17)30322-2/rf0135

Leenderstee, J., & Liu, S. (1978). *A three-dimensional turbulent energy model for non-homogeneus estuaries and coastal systems* . Amsterdam: J. C. J. Nihoul, Elsevier.

Leffler, K., & Jay, D. A. (2009). Enhancing tidal harmonic analysis: robust (hibrid L1/L2) solutions. *Cont. Shelf Res., 29*, 78-88. Obtenido de http://refhub.elsevier.com/S1385-1101(17)30322-2/rf0145

Leitao, J. C., Neves, R., Leitao, P. C., & Coelho, H. (1996). Hydrodynamic characterisation of the Ria Formosa with the Mohid system. *Associaçao Portuguesa dos Recursos Hidricos*, 447-458.

Li, Y., Lence, B. J., & Calisal, S. M. (2011). An integrated model for estimating energy cost of a tidal current turbine farm. *Energy Convers Manag, 52*, 1677–87. doi:http://dx.doi.org/10.1016/j.enconman.2010.10.031

Li, Y., Lence, B. J., & Calisal, S. M. (2011). An integrated model for estimating energy cost of a tidal current turbine farm . *Energy Convers Manag, 52*, 1677–87. doi:http://dx.doi.org/10.1016/j.enconman.2010.10.031

Liang, D., Xia, J., Falconer, R. A., & Zhang, J. (2014). Study on tidal resonance in severn estuary and Bristol Channel. *Coast. Eng. J., 56*(01), 1450002. Obtenido de http://refhub.elsevier.com/S0960-1481(16)30798-4/sref3

Liu, P., & Veitch, B. (2012). Design and optimization for strength and integrity of tidal turbine rotor blades. *Energy, 46*, 393–404. doi:http://dx.doi.org/10.1016/j.energy.2012.08.011

Lomonaco, P. (1999). *Propagación de la onda de marea en estuarios someros. PhD. Thesis.* Cantabria (Spain): Universidad de Cantabria. doi:DOI:10.13140/RG.2.1.2263.2480

Lopes de Almeida, C. (2008). *Aproveitamento Da Energia Da Onda de Maré No Estuário Do Tejo.* PhD. Universidade de Aveiro.

Lopes, J. M. (2004). *Modelação Matemática do Transporte de Sedimentos no Estuário do Guadiana. Master thesis in Mechanical Engineering.* Universidade do Minho (Portugal).

Lopes, J., Neves, R., Dias, J., & Martins, F. (2003). Calibração de um sistema de modelação para o Estuário do Guadiana. *Thalassas (special issue 4º simposio sobre el margen continental ibérico atlántico), 19 (2)*, 155-156.

Luettich, R. A., Westerink, J. J., & Sheffner, N. W. (1991). *ADCIRC: an advanced three-dimensional model for shelves coasts and estuaries. Report I: theory and methodology of ADCIRC-2DDI and ADCIRC-3DL.* Department of the Army, US Army Corps of Engineers.

Lyard, F., Lefevre, F., Letellier, T., & Francis, O. (2006). Modelling the global ocean tides: a modern insight from FES 2004. *Ocean Dyn, 56*, 394-415.

Marshall, J., Adcroft, A., Hill, C., Perelman, L., & Heisey, C. A. (1997b). A finite-volume, incompressible Navier Stokes model for studies of the ocean on parallel computers. *J Geophys Res*, 5753–66.

Marshall, J., Hill, C., Perelman, L., & Adcroft, A. (1997a). Hydrostatic, quasi-hydrostatic and non-hydrostatic ocean modelling. *J Geophys Res, 102*, 5733-52.

Martins, F., Leitao, P. C., Silva, A., & Neves, R. (2001). 3D modelling of the Sado Estuary using a new generic vertical discretazation approach. *Oceanol, 24*, 51-62. Obtenido de http://refhub.elsevier.com/S1385-1101(17)30322-2/rf0170

McDowell, D. M., & O'Connor, B. A. (1977). *Hydraulic Behaviour of Estuaries.* London: McMillan. Obtenido de http://refhub.elsevier.com/S1385-1101(17)30322-2/rf0180

MEDAR, G. (2002). Medatlas 2002: Mediterranean and Black Sea database of temperature, salinity and bio-chemical parameters climatological atlas. Paris.

Medina, R., Losada, M. A., Lomonaco, P., & Baquerizo, A. (1998). Application of a long-term evolution model of tidal inlets to the design of a navigation channel, the Navia inlet case. *Proceedings 26 th International Conference on Coastal Engineering.* Copenhagen (Denmark).

Miranda, R., Braunschweig, F., Leitao, P., Neves, R., Martins, F., & Santos, A. (2000). MOHID 2000. A coastal integrated object oriented model. En W. R. Blain, & C. A. Brebbia, *Hydraulic Engineering software VIII* (págs. 393-401). WIT press. Obtenido de http://refhub.elsevier.com/S1385-1101(17)30322-2/rf0190

MITgcm. (s.f.). *(http://mitgcm.org/sealion/online_documents/node2.html).*

MOHID Water Modelling System 2002. (2002). Obtenido de http://www.mohid.com/

Morales, J. A. (1993). *Sedimentología del Estuario del Guadiana (S.W. España-Portugal). Ph.D thesis* (Vol. 274). Sevilla, Spain: University of Sevilla.

Muller, M., & Wallace, R. (2008). Enabling science and technology for marine renewable energy. *Energy Policy, 36*, 4376–82. doi:http://dx.doi.org/10.1016/j.enpol.2008.09.035.

Muller, M., Jeffrey, H., Wallace, R., & von Jouanne, A. (2010). Centers for marine renewable energy in Europe and North America. *Oceanography, 23 (2)*, 42-52. doi:http://dx.doi.org/10.5670/oceanog.2010.42

Naranjo, C., García-Lafuente, J., Sánchez Garrido, J. C., Sánchez Román, A., & Delgado Cabello, J. (2012). The Western Alboran Gyre helps ventilate the Western Mediterranean Deep Water through Gibraltar. Deep Sea Res Part I. *Ocean Res Pap, 63*, 157–63.

Nash , S., O' Brien, N., Olbert, A., & Hartnett, M. (2014). Modelling the far field hydro-environmental impacts of tidal farms – a focus on tidal regime, inter-tidal zones and flushing. *Comput. Geosci., 71*, 20-27. doi:https://doi.org/10.1016/j.cageo.2014.02.001

Niblick, A. (2012). *Experimental and Analytical Study of Helical Cross-Flow Turbines for a Tidal. PhD.* University of Washington.

Nishino, T., & Willden, R. H. (2012). Effects of 3-d channeled blockage and turbulent wake mixing on the limit of power extraction by tidal turbines . *International Journal Heat Fluid Flow, 37*, 123-135,. doi: https://doi.org/10.1016/j.ijheatfluidflow.2012.05.002

Ocean Energy Forum. (2016). *Ocean Energy Strategic Roadmap 2016, Building Ocean Energy for Europe.* Obtenido de https://webgate.ec.europa.eu/maritimeforum/sites/maritimeforum/files/OceanEnergyForum_Roadmap_Online_Version_08Nov2016.pdf.

Oceanflowenergy. (s.f.). *Oceanflowenergy*. Obtenido de Oceanflowenergy: http://www.oceanflowenergy.com/Evopod-Technology.html

Oliveira, A., Fortunato, A., & Pinto, L. (2006). Modelling the hydrodynamics and the fate of passive and active organisms in the Guadiana Estuary. *Estuarine, Coastal and Shelf Science, 70*, 76-84.

O'Rourke, F., Boyle, F., & Reynolds , A. (2009). Renewable energy resource and technologies applicable to Ireland. *Renew Sustain Energy Rev, 13*, 1975-84. doi:http://dx.doi.org/10.1016/j.apenergy.2009.08.014.

O'Rourke, F., Boyle, F., & Reynolds , A. (2010b). Tidal energy update 2009. *Appl Energy, 87*, 398–409. doi:http://dx.doi.org/10.1016/j.apenergy.2009.08.014

O'Rourke, F., Boyle, F., & Reynolds , A. (2011). Marine current energy devices: current status and possible future applications in Ireland . *Renew Sustain Energy Re, 14*, 1026–36. doi:http://dx.doi.org/10.1016/j.rser.2009.11.012

O'Rourke, F., Boyle, F., & Reynolds, A. (2010a). Marine current energy devices: current status. *Renew Sustain Energy Rev, 14*, 1026-36. doi:http://dx.doi.org/10.1016/j.rser.2009.11.012.

O'Rourke, F., Boyle, F., & Reynolds, A. (2010c). Tidal current energy resource assessment in Ireland: current status and future update. *Renew Sustain Energy Rev, 14*, 3206–12. doi:http://dx.doi.org/10.1016/j.rser.2010.07.039

O'Rourke, F., Boyle, F., & Reynolds, A. (2014). Ireland's tidal energy resource. An assessment of s site in the Bulls Mouth and Shannon Estuary using measured data. *Energy Convers Manag, 87*, 726-734. doi:https://doi.org/10.1016/j.enconman.2014.06.089

Pablo, H., Sobrinho, J., Garcia, M., Campuzano, F., Juliano, M., & Neves, R. (2019). Validation of the 3D-MOHID Hydrodynamic Model for the Tagus Coastal Area. *Water, 11*, 1713.

Pacheco , A., Gorbeña , E., Plomaritis , T., & Gonçalves, J. (2018). Lessons learned from E1 Evopod Tidal Energy Converter deployement at Ria Formosa, Portugal . *Conference paper. 7th International Conference on Ocean Energy France.* Cherbourg (France). doi: https://www.researchgate.net/publication/327338849

Pacheco, A., & Ferreira, O. (s.f.). Hydrodynamic changes imposed by tidal energy converters on extracting energy on a real case scenario . *Applied Energy, 180*, 369-385. doi: http://dx.doi.org/10.1016/j.apenergy.2016.07.132

Pawlowicz, R., Beardsley, B., & Lentz, S. (2002). Classical tidal harmonic analysis including error estimates in MATLAB using T_TIDE. *Comput. Geosci., 28*, 929-937. Obtenido de http://refhub.elsevier.com/S1385-1101(17)30322-2/rf0215

Pearce, N. (2005). Worlwide Tidal Current Energy Developments and Oportunities for Canada's Pacific Coast. *International Journal of Green Energy*(2:4), 365-386. doi:10.1080/01971520500287974

Pinto, L., Fortunato, A. B., Oliveira, A., & Baptista, A. M. (2004). Haline stratification in the Guadiana Estuary. Part II: numerical modelling (in Portuguese). *Recursos Hídricos, 25/2*, 99 - 110.

Pinto, L., Oliveira, A., Fortunato, A. B., & Baptista, A. M. (2003). Analysis of the stratification in the Guadiana estuary . En *Spaulding (Ed.), Estuarine and Coastal Modelling, VIII* (pág. 1094e1113). ASCE.

Prandle, D. (2003). Relationships between tidal dynamics and bathymetry in strongly convergent channels. *J.Phys. Oceanogr., 33(12)*, 2738-2750. Obtenido de http://refhub.elsevier.com/S1385-1101(17)30322-2/rf0230

Prandle, D. (2004). How tides and river flows determine estuarine bathymetrics. *Prog. Oceanogr., 61 (1)*, 1-26. Obtenido de http://refhub.elsevier.com/S1385-1101(17)30322-2/rf0235

Prandle, D. (2009). *Estuaries: Dynamics, Mixing, Sedimentation and Morphology.* Cambridge University Press. Obtenido de http://refhub.elsevier.com/S1385-1101(17)30322-2/rf0240

Ramos, V., & Iglesias, G. (2013). Performance assessment of tidal stream turbines: a parametric approach. *Energy Convers Manag, 69*, 49-57. doi:http://dx.doi.org/10.1016/j.enconman.2013.01.008

Raschid, A. (2012). Status and potentials of tidal in stream energy resources in the southern coast of Iran: a case study. *Renew Sustain Energy Rev, 16*, 6668–77. doi:http://dx.doi.org/10.1016/j.rser.2012.08.010

Resch, G., Held, A., Faber , T., Pancer , C., Toro, F., & Haas, R. (2008). Potentials and prospects for renewable energies at global scale. *Energy Pol, 36*, 4048-36. Obtenido de http://refhub.elsevier.com/S0360-5442(17)32160-6/sref4

Ruíz Muñoz, F., González-Regalado, M. I., & Morales, J. A. (1996). Distribución y ecología de los foraminíferos y ostrácodos actuales del estaurio mesomareal del Río Guadiana (SO España). *Geobios., 29(5)*, 513-528. Obtenido de http://refhub.elsevier.com/S1385-1101(17)30322-2/rf0245

Sammartino, S., García-Lafuente, J., Naranjo, C., Sánchez Garrido, J. C., Sánchez Leal, R., & Sánchez Román, A. (2015). Ten years of marine currents measurements in Espartell Sill, Strait of Gibraltar. *J. Geophys. Res. Oceans, 120*, 6309-6328. doi:10.1002/2014JC010674

Sánchez Garrido, J. C. (2009). *Generación y propagación de ondas internas en el Estrecho de Gibraltar: Efectos 3-D y de rotación [PhD thesis].* Granada (Spain): University of Granada.

Sánchez Garrido, J. C., García-Lafuente, J., Criado-Aldeanuea, F., Baquerizo, A., & Sannino, G. (2008). Time-spatial variability observed in velocity of propagation of the internal bore

in the Strait of Gibraltar. *J Geophys Res, 113*. doi:http://dx.doi.org/10.1029/2007JC004624

Sánchez Garrido, J. C., Sannino, G., Liberti, L., García-Lafuente, J., & Pratt, L. (2011). Numerical modeling of three dimensional stratified tidal flow over Camarinal Sill, Strait of Gibraltar. *J Geophys Res, 116*. doi:http://dx.doi.org/10.1029/2011JC007093

Sánchez Román, A. J., Sannino , G., García-Lafuente, J., Carrillo, A., & Criado-Aldeanueva, F. (2009). Transport estimates at the western section of the Strait of Gibraltar: a combined experimental and numerical modeling study Geophys Res. *Geophys Res, 114*, C06002. doi:http://dx.doi.org/10.1029/2008JC005023.

Sannino, G., Bargagli , A., & Artale, V. (2002). Numerical modelling of the mean exchange through the Strait of Gibraltar. *J Geophys Res, 107(C8)*, 3094. doi:http://dx.doi.org/10.1029/2001JC000929.

Sannino, G., Bargagli , A., & Artale, V. (2004). Numerical modelling of the semidiurnal tidal exchange through the Strait of Gibraltar. *J Geophys Res, 109*, C05011. doi:http://dx.doi.org/10.1029/2003JC002057

Sannino, G., Pratt, L., & Carrillo, A. (2009). Hydraulic criticality of the exchange flow through the Strait of Gibraltar. *J Phys Oceanogr , 39*, 2779–99. doi: http://dx.doi.org/10.1175/2009JPO4075.1

Savenije, H. G. (2005). *Salinity and Tides in Alluvial Estuaries.* Elsevier BV. Obtenido de http://refhub.elsevier.com/S1385-1101(17)30322-2/rf0250

Savenije, H. G., & Veling, E. J. (2005). Relation between tidal damping and and wave celerity in estuaries. *J. Geophys. Res., 110*, C04007. doi:https://doi.org/10.1029/2004JC002278

Silva, A. J., Lino, S., Santos, A. I., & Oliveira, A. (2003). Near Bottom Sediment Dynamics in the Guadiana Estuary. *Thalassas, 9*, 180-182. Obtenido de http://refhub.elsevier.com/S1385-1101(17)30322-2/rf0265

Silva, M. C., Fortunato, A. B., Oliveira, A., & Rocha, J. S. (2000). Environmental Conditions in the Guadiana Estuary: The Present Knowledge. (A. P. Hídricos, Ed.) Obtenido de http://refhub.elsevier.com/S1385-1101(17)30322-2/rf0260

Simpson, J. H., Brown, J., Matthews, J., & Allen, G. (1990). Tidal straining, density currents, and stirring in the control of estuarine stratification . *Estuaries, 13*, 125–132. doi:https://doi.org/10.2307/1351581

Sousa, M. C., Vaz, N., Alvarez, I., Gomez-Gesteira, M., & Dias, J. M. (2014). Modeling the Minho River plume intrusion into the Rias Baixas (NW Iberian Peninsula) . *Continental Shelf Research, 85*, 30-41. doi:https://doi.org/10.1016/j.csr.2014.06.004

Thönniben, F., Marnett, M., Roidl, B., & Schröden, W. (2016). A numerical analysis to evaluate Betz's Law for vertical axis wind turbines . *J. Phys, 753, 022056*.

Threshel, R., & Musial, W. (2010). Ocean renewable energy's potential role in supplying future electrical energy needs. *Oceanography, 23 (2)*, 16-21. doi:http://dx.doi.org/10.5670/oceanog.2010.39

Toffolon, M., & Savenije, H. G. (2011). Revisiting linearized one-dimensional tidal propagation. *Journal of Geophysical Research., 116*. doi:10.1029/2010JC006616.

Valentim, J. M., Vaz, N., Silva, H., Duarte, B., Caçador, I., & Dias, J. M. (2013). Tagus estuary and Ria de Aveiro salt marsh dynamics and the impact of sea level rise . *Estuarine, Coastal and Shelf Science, 130*, 138-151. doi:https://doi.org/10.1016/j.ecss.2013.04.005

Van Rijn, L. C. (2010). *Tidal Phenomena in the Scheldt Estuary.* Deltares. Obtenido de http://refhub.elsevier.com/S1385-1101(17)30322-2/rf0275

Vaz, N., Fernandes, L., Leitao, P. C., Dias, J. M., & Neves, R. (2009). The Tagus Estuarine Plume Induced By Wind and River Runoff: Winter 2007 Case Study . *Journal of Coastal Research,, SI 56, , ICS2009* , 1090-1094. Obtenido de ISSN 0749-0258

Wang, S., Yuan, P., Li, D., & Jiao, Y. (2011). An overview of ocean renewable ernergy in China. *Renew Sustain Energy Rev, 15*, 91–111. doi:http://dx.doi.org/10.1016/j.rser.2010.09.040

Wolanski, E., Chícharo, L., Chícharo, A. M., & Morais, P. (2006). An eco-hydrology model of the Guadiana Estuary (South Portugal). *Estuar. Coast. Shelf Sci, 70*, 132-143. doi:https://doi.org/10.1016/j.ecss.2006.05.029

Woolf, D. K., Easton, M. C., Bowyer, P. A., & McIlveny, J. (2014). The Physics and Hydrodynamic Setting of Marine Renewable Energy. *Marine Renewable Energy Technology and Environmental Interactions. Humanity and the Sea.* doi:https://doi.org/10.1007/978-94-017-8002-5_2

Zhang, Y. L., Baptista, A. M., & Myers, E. P. (2004). A cross-scale model for 3D baroclinic circulation in estuary-plume-shelf systems: I. Formulation and skill assessment . *Continental Shelf Research, 24/18*, 2187e2214.

Zhou , Z., Benbouzid , M., Charpentier , J. F., Scuiller , F., & Tang, T. (2013). A review of energy storage technologies for marine current energy systems. *Renew Sustain Energy Rev , 18*, 390-400. doi: http://dx.doi.org/10.1016/j.rser.2012.10.006.

APÉNDICE. ACRÓNIMOS Y ABREVIATURAS

· EPRI: Instituto de Investigación de Energía Eléctrica de EEUU

· NREL: Laboratorio Nacional de Energía Renovable en EEUU

· MCT: Turbina de corriente marina

· CSIRO: Organización de Investigación Científica e Industrial de la Commonwealth

· SG: Estrecho de Gibraltar

· TN: Estrechamiento de Tarifa

· CS: umbral de Camarinal

· ES: Umbral de Espartel

· MB: Banco Majuan

· GE: Estuario del Guadiana

· M2: primera constituyente semidiurna de marea

· S2: segunda constituyente semidiurna de marea

· K1: primera constituyente diurna de marea

· O1: segunda constituyente diurna de marea

· M4: primera constituyente no lineal de marea

· VRSA: Vila Real de Santo Antonio (Portugal)

· Qr: descarga de agua dulce de un río

. MITgcm: Modelo Instituto Tecnológico de Massachusetts

· MOHID: Modelo Hidrodinámico

· GIS: Sistema de Información Geográfica

· E_{flux}: Intensidad del Flujo de Energía

· ρ: densidad del agua del mar

· u: velocidad de corriente

· u_1: componente longitudinal de la velocidad

· u_2: componente transversal de la velocidad

· STA: Amplitud de Marea Semidiurna

· QTA: Amplitud de Marea Cuartidiurna

· P_T: potencia instantánea

· F_T: fuerza de reacción

· A_T: área sumergida de una turbina

· C_T: coeficiente de empuje

· C_P: coeficiente de potencia

· E_T: energía extraída

· Δt: intervalo temporal (Ascione Kenov, Garcia, & Neves, 2012) (Valentim, y otros, 2013) (Pablo, y otros, 2019) (Vaz, Fernandes, Leitao, Dias, & Neves, 2009) (Leitao, Neves, Leitao, & Coelho, 1996)